UNIVERSITY OF SOUTHAMPTON

Beyond Standard Model Collider Phenomenology of Higgs Physics and Supersymmetry

Marc Christopher Thomas

Presented for the degree of

Doctor of Philosophy

Southampton High Energy Physics
Department of Physics and Astronomy
Faculty of Science
University of Southampton

March 2015

This version of the thesis was submitted for examination in March 2015,

and may differ from later versions.

ABSTRACT

University of Southampton,

Faculty of Engineering, Science and Mathematics

School of Physics and Astronomy

DOCTOR OF PHILOSOPHY

"Beyond Standard Model Collider Phenomenology

of Higgs Physics and Supersymmetry"

by Marc Christopher Thomas

In this thesis I study the collider phenomenology of BSM physics at the LHC, concentrating on the Higgs boson and supersymmetery. The implications and effects on cross sections of the loss of unitarity in scattering processes involving multiple vector bosons and/or the Higgs, when the Higgs couplings to the W and the Z are non-SM, is studied using an effective Lagrangian. Subsequently methods to remove unwanted background from transversely polarised vector bosons are explored, which enable an estimation of the potential to measure the Higgs couplings to weak bosons in a model-independent way via vector boson fusion. MSSM effects on Higgs production and decay are also considered, concentrating on the effects due to light stops, sbottoms and staus. Amongst other things, we find that light 3^{rd} generation squarks generally produce asymmetrical alteration in signal strengths of different production channels, generally causing $\frac{\mu_{VBF}}{\mu_{ggF}} > 1$. Finally we extend some ATLAS analyses in the low $\Delta m = m_{\tilde{t}} - m_{\tilde{\chi}_1^0}$ region, extending the excluded masses of light stops. This enables us to limit the maximum effects of light stops on the Higgs, and further limits the parameter space where the light stop scenario of electroweak baryogenesis is viable.

Contents

List of Figures

Declaration of Authorship

I, Marc Thomas, declare that this thesis, entitled 'Beyond Standard Model Collider Phenomenology of Higgs Physics and Supersymmetry' and the work presented in it are my own. I confirm that

- This work was done wholly or mainly while in candidature for a research degree at this university.
- Where I have consulted the published work of others, this is always clearly attributed.
- Where I have quoted the work of others, the source is always given. With the exception of such quotations, this thesis is entirely my own work.
- I have acknowledged all main sources of help.
- Where the thesis is based on work done by myself jointly with others, I have made clear exactly what was done by others and what I have contributed myself.
- Work contained in this thesis has previously been published in references [30], [31] and [32].

Signed:

Date:

Acknowledgements

I would like to express my thanks to the many people who have given me the help and guidance to enable me to complete this PhD.

The guidance and support offered by my supervisor Professor Alexander Belyaev, as well as the encouragement to take part in collaborations and conferences, and to present my work to a wider audience has helped me to grow in confidence as a research scientist and I'd like to give him a special thanks.

I'd like to express my appreciation to my many collaborators whose patient explanations and advice have helped me complete the work in this thesis and made it so enjoyable. In particular I'd like to thank Professor Stefano Moretti and Professor Shaaban Khalil for many long discussions on the supersymmetric Higgs sector, and Dr Alexandra Oliveira and Professor Rogerio Rosenfeld for their patience and help which allowed me to complete my first paper.

My office mates also deserve my thanks for the long and fascinating discussion on all topics of physics and the world in general, and making the office such an enjoyable environment. In particular I'd like to thank Jason Hammett, Shane Drury, Maria Dimou, Daniele Barducci and Jurgen Dietz for their help in the first couple of years when getting to grips with particle physics and QFT was a particular challenge.

I'd also like to thank the STFC for providing the funding which has allowed me to complete this work.

Finally I'd like to say thank you to my wife Emily. Without her support, encouragement and patience this PhD would not have been possible.

— M.C.T

Chapter 1

Introduction

1.1 The Standard Model

The standard model (SM) as a theory of particle physics was completed in its present form in the 1970s. Since this time it has achieved remarkable success with the discovery, as predicted by the model of the tau lepton[1] along with the charm[2, 3] and bottom quarks[4] in the 1970s, the W and Z bosons in the 1980s[5–7], the top quark in the 1990s[8] and the tau neutrino in 2000[9]. The final particle in the standard model, the Higgs boson was discovered at CERN in July 2012[10, 11], completing the set of particles predicted by the SM. As well as forecasting these new particles, the SM has also been able to provide accurate predictions for a huge variety of physical phenomenon which have been confirmed by experiment. These range from the calculation of anomalous magnetic dipole moments and the results of scattering experiments using perturbation theory to the calculation of masses and lifetimes of QCD bound states using lattice techniques. Some of these predictions can have unprecedented precision (most notably those involving only QED), for example there is agreement between the theoretical expectation and experimental measurement of the Rydberg constant of around 11 significant figures[12, 13][1].

[1] The value of α_{em} is set by a measurement of the anomalous magnetic moment of the electron, which allows a prediction of the Rydberg constant which matches experiment to 11 significant figures.

1.2 Problems with the Standard Model

Even while experiments have been confirming SM predictions, there have also been a number of observations which it cannot describe, including:

1. *Neutrino oscillations*

   Neutrinos have been observed to oscillate in experiments involving neutrinos from the sun, the atmosphere following cosmic ray collisions, nuclear reactors and from beam experiments. This requires that the neutrinos have a mass, and the SM does not explain either neutrino oscillations or masses.

2. *Matter/Antimatter asymmetry*

   Today the observable universe is made up almost entirely of matter. This could be explained by a baryon asymmetry in the early universe, which can be estimated from the baryon to photon ratio today, and is of order 10^{-10}[14]. This must have arisen following inflation and reheating when any initial asymmetry would have been washed out, and cannot be explained by the SM.

3. *Cold Dark Matter*

   Evidence from galaxy rotation curves, the motion of galaxy clusters, colliding galaxy clusters such as the Bullet Cluster, gravitational lensing, the cosmic microwave background (CMB) and large scale structure formation in the early universe point towards the existence of non-relativistic ("cold"), or possibly semi-relativistic[15] ("warm"), neutral, massive, non-baryonic matter. In the SM, neutrons do not fit this description as their very small mass means that they would be relativistic ("hot") dark matter, and there are no other viable SM candidates.

4. *Dark Energy*

   The universe's expansion is accelerating, consistent with a cosmological constant or equivalently dark energy. If the SM is assumed to be valid up to the Planck scale, it overestimates this energy by a ridiculous factor of 10^{120}.

5. *Inflation*

   As well as providing solutions to the horizon, magnetic monopole and flatness

problems, inflation is consistent with the scale-invariant, Gaussian perturbations displayed by the CMB. The SM cannot explain inflation.

Furthermore, there are a number of theoretical considerations which also lead us to seek a model beyond the SM:

1. *Gravity*

   The SM does not include gravity. Whilst general relativity can be used as an effective theory of quantum gravity at low energies, it cannot be combined with the SM to give a consistent theory above the Planck scale. We require a new theory to be able to simultaneously describe all the forces in a way which would be valid above the Planck scale.

2. *The Gauge Hierarchy Problem*

   The Higgs mass has been experimentally measured to be around the weak scale. However, if there is new physics at higher scales such as the Grand Unified Theory (GUT) scale (10^{16}) GeV or Planck scale (10^{19}) GeV, we would expect radiative corrections to increase its physical mass to around these scales. To explain this we either require a remarkable fine-tuning of the cancellation that occurs between the radiative corrections and the bare mass of the Higgs boson, or new physics beyond the SM such as a new symmetry or lower cut-off scale.

3. *The strong CP problem*

   There is a CP-violating term allowed in the SM (QCD) Lagrangian which we would naively expect to be of order 1. However measurements such as that of the neutron dipole moment[16] show that the upper bound for this term is around 10^{-11}, which is not explained within the SM.

4. *Meta-stable vacuum*

   Given derivations based on the top quark and Higgs masses, we live in a false vacuum which has a lifetime longer than the age of the universe (metastable). This is often considered less desirable than a stable universe.

5. *Unexplained Structure in the Standard Model*

   There are 19 free parameters in the standard model[2]. Many physicists feel that a more fundamental theory would be able to derive relationships between a number of these currently independent quantities, reducing the number of free parameters. Some of the patterns that people are particularly interested in explaining are:

   - Why there are 3 families of particles.
   - The structure of the fermion masses and mixing.
   - Why the electromagnetic charge is quantised in units of $\frac{1}{3}$ when for a U(1) symmetry it could take any value.
   - Why the particular $\mathrm{SU(3)_c} \bigotimes \mathrm{SU(2)_L} \bigotimes \mathrm{U(1)_Y}$ group structure of the SM.
   - Why is there 3+1 spacetime dimensions.

As a result of these theoretical questions, and especially the experimental observations, a large number of beyond standard model theories have been developed which address some of these issues.

1.3 Going Beyond the Standard Model

An enormous range of beyond standard model (BSM) physics has been proposed. These include those that extend the theoretical framework beyond standard quantum field theory (QFT), such as string theory and loop quantum gravity. However even these beyond QFT theories are likely to be well described by a QFT at the energies we are currently able to experimentally probe with colliders, and we will stay within the QFT paradigm.

The first thing a BSM model needs to achieve is to recreate the highly successful predictions of the SM. For this reason, the majority of BSM models involve extending the SM with further fields and possibly further symmetries of the Lagrangian. I will not attempt to summarise or categorise all the different BSM models. Instead I'll limit myself to two topics with are relevant to the research presented later in this thesis. The first is that of Effective Field Theory (EFT), which uses the fact that for models

[2]There are 19 free parameters if we include the QCD CP violating term responsible for the strong CP problem, and exclude neutrino masses and mixing.

with a hierarchy of mass scales, the low energy physics can be well approximated by an effective Lagrangian which is only valid at energies well below the higher mass scale. This allows aspects of many BSM models to be studied simultaneously in a largely model independent way. The second topic is supersymmetry, a popular BSM model which predicts new particles which due to naturalness arguments have a reasonable likelihood to be light enough to be discoverable at the Large Hadron Collider (LHC).

1.3.1 Effective Field Theories

Using an effective field theory (EFT) is an excellent way of allowing us to study a large range of BSM models simultaneously. The basic idea is that in a model with a separation of scales, the high energy contributions to the action can be "*integrated out*", leaving a QFT which contains only the low mass fields. The remaining action is non-local in spacetime, however expanding in powers of the inverse of the heavy mass scale, Λ, gives us a local Lagrangian with an infinite series in the small power Λ^{-1}. For a specific process, as long as the energy, $E \ll \Lambda$, then the contribution to the action of each term in the series falls rapidly with increasing powers of $\left(\frac{1}{\Lambda}\right)$ and we can truncate the series at a desired order of Λ^{-1}. We thus have a Lagrangian containing light fields only, which can be used to calculate low energy observables, which in general is non-renormalizable but is otherwise valid.

To be more concrete, we can consider a theory which has both heavy particles with mass $\sim \Lambda$, and much lighter particles. In interactions with light particles in the initial state, with all momenta and energies, p,E $\ll \Lambda$, the heavy particles can never appear in the final state. They will still have physical effects by appearing in loops as well as at tree level as off-shell intermediate particles, and indeed may allow vertices which do not occur at tree level in the case of vertices which are loops at leading order. However at low energies these effects are not resolved, and can be taken account of by altering the parameters of the low energy Lagrangian and adding new contact interactions. The beauty of this approach is that any set of *different* high energy theories which contain the same low energy particles and symmetries, can be described by the *same* low energy Lagrangian, with the differences between high energy models manifesting only as differences in the masses and couplings at low energy. Therefore if we use data to set

limits on an EFT Lagrangian, we are simultaneously setting limits on the parameters of a wealth of high energy models. Moreover, we can even study effective field theories without any reference to a specific high scale model.

If we consider EFTs in the context of LHC phenomenology, we know exactly what the low energy fields and symmetries are; the fields and symmetries of the standard model. Therefore we should be able to describe the collider physics of any BSM theory which has new particles much too heavy to be produced at the LHC by using an effective field theory.

A note of caution is appropriate here. For such an effective field theory to be valid, it is required that the new physics is at a much higher scale than the SM. This is not an unreasonable assumption as the SM has been well studied, and tight bounds have been set on many of its parameters, meaning that the effect of new physics at this energy must be relatively small. Consequently any new particles associated with new physics is likely to be much heavier than the SM. However we cannot rule out the possibility of new light and very weakly interacting particles, and for these models the EFT approach is invalid.

To construct an effective field theory Lagrangian, we can use either a *top-down* or *bottom-up* approach. The *top-down* approach would be to start with a complete BSM model valid at high energies and follow the steps described above, integrating out high energy contributions and expanding in powers of $\left(\frac{1}{\Lambda}\right)$ where Λ is the scale of the high energy physics. This can have the advantage of telling us relations between parameters in the effective field theory which would otherwise be hidden, as well as giving us a simpler Lagrangian for calculations. The *bottom-up* approach more commonly used makes no reference to possible complete BSM models. We simply choose the particle content at the lower energies we're interested in and write down all terms allowed by the symmetries of Lagrangian up to whichever order in Λ^{-1} we wish to work. The order of Λ^{-1} is usually given in terms of the compensating mass dimension of its associated operator, for example terms with a Λ^{-2} coefficient are usually referred to as dimension-6 operators, i.e. $\mathrm{D} = 6$.

In chapters 2 and 3 we will be using an effective field theory for Higgs and vector boson scattering.

1.3.2 Supersymmetry

In the standard model, the symmetry group of the S-matrix is the direct product of the Poincaré group and the internal symmetry groups. It was shown in 1967 by Coleman and Mandula[17] that any extension of this must have generators which commute with all of the Poincaré group generators, and therefore the extended symmetry group would still be a direct product of the Poincaré group and a larger internal symmetry group. As the Poincaré group is the group of symmetries of spacetime, this showed that the spacetime symmetries of the S-matrix could not be extended non-trivially. However in 1974, Haag, Lopuszánski and Sohnius[18] discovered that if we also allow the possibility of fermionic generators (which Coleman and Mandula had not considered), then a non-trivial extension of the Poincaré group is indeed possible, allowing it to be embedded within a larger Super-Poincaré group which would not be a direct product of the Poincaré and internal symmetry groups. The new fermionic generators have the effect of taking bosons into fermions and vice versa, with the new symmetry being called supersymmetry (SUSY). The irreducible representations of this Super-Poincaré group are called supermultiplets, and contain in each case a SM particle and its SUSY partner[3].

For a supersymmetric theory to reproduce the SM predictions, it must include (at least) all of the SM particles in its Lagrangian. A realistic SUSY model therefore introduces many new particles, with at least one supersymmetric partner for each SM particle[4].

The reason that supersymmetry is popular is not only that it is the only possible non-trivial extension of the usual spacetime symmetries, but it's also able to solve many of the problems of the standard model listed in section 1.2. Some of the attractive features of SUSY are:

- It solves the gauge hierarchy problem. For each fermion loop which contributes to the Higgs self energy, there is a perfect cancellation from SUSY scalar loops, naturally allowing a light Higgs without fine-tuning. It should however be noted that in the simplest SUSY theory consistent with experiment, the Minimal Su-

[3]The supermultiplets also contain an auxiliary field which is required to ensure the SUSY algebra closes off-shell. However these can be eliminated from the Lagrangian by using the equations of motion to rewrite them in terms of the other fields.

[4]The minimum particle content of a realistic SUSY model is actually more than this as discussed in section 1.3.2 on the Minimal Supersymmetric Standard Model (MSSM).

persymmetric Standard Model (MSSM), it introduces a *new* fine-tuning problem, known as the μ-problem. This problem is to explain why μ, a mass parameter which appears in the Lagrangian, is at around the electroweak scale, rather than at around the Planck scale.

- It contains natural candidates for dark matter, such as the neutralino which is a mixture of the SUSY partners of the neutral gauge bosons and the Higgs. It is weakly interactive, massive and can be stable, as required for cold dark matter.

- Given certain parameters, it is able to explain the matter/antimatter asymmetry in the universe. For example, light (right handed) stops allow viable electroweak baryogenesis scenarios.

- It is able to explain the current 3.6σ disagreement between theory and experiment of the muon (g-2) anomalous magnetic moment by introducing new particles in the loops[19–24].

- In the context of grand unified theories it allows unification of the couplings at around 10^{16} GeV.

- There are SUSY models with areas of parameter space where the vacuum is entirely stable.

- In the simplest phenomenological SUSY model (the MSSM), the *maximum* value of the Higgs boson mass is around 140 GeV, consistent with its observed mass of around 126 GeV[5][25].

- It is possible to have radiative electroweak symmetry breaking in SUSY, i.e. spontaneous electroweak symmetry breaking via the running of the Higgs mass parameters.

Furthermore, supersymmetry is required by string theory for self consistency of the theory and to allow it to describe fermions.

[5]This is discussed further in section 4.2.

The Minimal Supersymmetric Standard Model (MSSM)

There is of course an infinity of different SUSY Lagrangian that could be written down. The Minimal Supersymmetric Standard Model (MSSM) is the minimal SUSY extension to the standard model that is possible. It contains a fermionic SUSY partner for each SM boson, and a bosonic SUSY partner for each chiral component of the SM fermions, as well as 2 Higgs doublets and their SUSY partners. There are two reasons why we are required to introduce an additional Higgs doublet compared to the SM. Firstly, the Yukawa terms in the MSSM appear in the superpotential which is holomorphic in the fields. This means that we are unable to use the complex conjugate of the Higgs field to give mass to the up-type quarks as we do in the SM, necessitating the introduction of a second Higgs field with opposite hypercharge. Secondly, with only a single Higgs doublet in the theory, its superpartner the Higgsino introduces an $\mathrm{SU}(2)_L^2\mathrm{U}(1)_Y$ triangle gauge anomaly, which can be cancelled by the SUSY partner of a second Higgs doublet with opposite hypercharge[6]. These two Higgs are know as *up* and *down* type, depending on which particle type they give a mass to. The MSSM is the most commonly studied SUSY model, and is the model I examine later in the thesis.

The particle content of the MSSM is three generations of chiral quark and lepton supermultiplets, the vector supermultiplets necessary to gauge the $SU(3)_C \times SU(2)_L \times U(1)_Y$ group of the SM and the two chiral $SU(2)$ Higgs doublet supermultiplets. The interactions involving vector supermultiplets are given by the gauge symmetry group of the theory, i.e. $SU(3)_C \times SU(2)_L \times U(1)_Y$, while the interactions between the chiral supermultiplets are described by the superpotential,

$$W = Y^E_{ij} L_i E^c_j H_d + Y^D_{ij} Q_i D^c_j H_d + Y^U_{ij} Q_i U^c_j H_u + \mu H_u H_d. \tag{1.1}$$

Here Q contains the $SU(2)$ (s)quark doublets and U^c and D^c the corresponding singlets, while the (s)lepton doublets and singlets reside in L and E^c, respectively. In addition, H_u and H_d denote Higgs supermultiplets with hypercharge $Y = \pm\frac{1}{2}$.

If SUSY is an unbroken symmetry then the SUSY particles would have exactly the

[6]The reason that this anomaly cancellation must occur can be seen by noting that the second Higgs doublet has the quantum numbers of the conjugate of the first Higgs doublet. Therefore its introduction is analogous to introducing the conjugate of the first Higgs, making their combination a real representation of its Lie groups, which therefore must be anomaly free.

same mass as their SM partners, and would have been observed by now. Therefore we know SUSY must be a broken symmetry and the SUSY particles have a different mass to their SM partners. This would initially seem to be a problem, as the exact cancellations required to solve the gauge hierarchy problem require the SM and SUSY partners to have the same mass. However if SUSY is only broken by the addition of Lagrangian terms whose coefficients have positive mass dimensions, known as *soft SUSY breaking* terms, the cancellation of the leading (quadratic in the cut-off) contribution to the Higgs mass parameter squared remain, and the substantially smaller logarithmic corrections become the largest contribution. This means that the main correction to the MSSM Higgs scalar mass parameter squared becomes $\propto m_{\text{soft}}^2 \ln\left(\frac{\Lambda_{\text{UV}}}{m_{\text{soft}}}\right)$ where Λ_{UV} is the UV cut-off scale of the model (generally M_{Planck}), and m_{soft} is the largest mass scale associated with the soft breaking terms. As the mass splitting between the SM particles and their SUSY particles are determined by m_{soft}, this correction to the Higgs squared mass parameter is small as long as the mass difference between the top and the stop masses is not too large, allowing SUSY to remain a solution to the gauge hierarchy problem. As a result of this requirement of soft SUSY breaking we have many additional free parameters in the Lagrangian, known as the soft SUSY breaking parameters. Writing down only gauge invariant terms with positive mass dimension, the soft SUSY terms in the MSSM are of the form[26]:

$$\begin{aligned}
\mathcal{L}_{\text{soft}}^{\text{MSSM}} = &-\frac{1}{2}\left(M_3\tilde{g}\tilde{g} + M_2\tilde{W}\tilde{W} + M_1\tilde{B}\tilde{B} + \text{c.c.}\right) \\
&- \left(\tilde{\bar{u}}\mathbf{a_u}\tilde{Q}H_u - \tilde{\bar{d}}\mathbf{a_d}\tilde{Q}H_d - \tilde{\bar{e}}\mathbf{a_e}\tilde{L}H_d + \text{c.c.}\right) \\
&- \tilde{Q}^\dagger\mathbf{m_Q^2}\tilde{Q} - \tilde{L}^\dagger\mathbf{m_L^2}\tilde{L} - \tilde{\bar{u}}\mathbf{m_{\bar{u}}^2}\tilde{\bar{u}}^\dagger - \tilde{\bar{d}}\mathbf{m_{\bar{d}}^2}\tilde{\bar{d}}^\dagger - \tilde{\bar{e}}\mathbf{m_{\bar{e}}^2}\tilde{\bar{e}}^\dagger \\
&- m_{H_u}^2 H_u^* H_u - m_{H_d}^2 H_d^* H_d - (bH_uH_d + \text{c.c})
\end{aligned} \tag{1.2}$$

where M_3, M_2 and M_1 are the masses of the gluino, wino and bino, which are the SUSY partners of the gauge bosons. The $\mathbf{a_u}$, $\mathbf{a_d}$, $\mathbf{a_e}$ are complex 3×3 matrices in family space, and the $\tilde{u}$, $\tilde{d}$, $\tilde{e}$, $\tilde{Q}$, $\tilde{L}$ are family triplets which are the SUSY partners (squarks and sleptons) of the their respective SM singlets/doublets. Likewise, $\mathbf{m_Q^2}$, $\mathbf{m_L^2}$, $\mathbf{m_{\bar{u}}^2}$, $\mathbf{m_{\bar{d}}^2}$ and $\mathbf{m_{\bar{e}}^2}$ are 3×3 Hermitian matrices in family space. The H_u and H_d are the scalar up-type and down-type Higgs, with the final line from Equation 1.2 being the soft-SUSY

breaking term of the Higgs potential.

More details of the Higgs sector of the MSSM, along with the masses and couplings of the top, bottom and tau SUSY partners, the stop, sbottom and stau respectively will be provided in chapter 4 as they are directly relevant to the research and results presented in that chapter.

1.4 Where to look for BSM physics

Since the Higgs discovery, the main purpose of the LHC is to find new physics. Broadly, BSM physics can be found either by finding new particles as an excess number of events in certain decay channels, or by finding deviations from SM predictions in the observables of SM processes. In this thesis, I use both of these techniques, focusing on deviations from SM cross sections in chapters 2–4, and new particle searches in chapter 5.

Following the first run of the LHC (run 1), which finished colliding protons at the end of 2012, we have observed that the Higgs couplings are broadly in agreement with SM predictions, but with large errors, still allowing significant deviations from these values (as is discussed in section 2.1[27–29]). Run 2 is due to start in spring 2015, which will greatly improve this precision.

With this in mind, the plan for the thesis is as follows. In chapter 2 I use an EFT Lagrangian to study the effects of a deviation of the Higgs-vector boson coupling on vector boson scattering and multiple Higgs production, and go on to examine techniques to improve the experimental sensitivity to vector boson scattering in chapter 3. The effects of supersymmetry on Higgs production and decay cross section are then studied in chapter 4, notably in scenarios with light stops, sbottoms and staus. Chapter 5 subsequently discusses work to extend the ATLAS search for stop squarks, ruling out an area of parameter space which still allows light stops, which are important for naturalness and baryogenesis. Finally I conclude in chapter 6.

Chapters 2 and 4 are heavily based on 2 papers published in JHEP[30, 31], chapter 3 is based on work published as part of the Les Houches 2013 Working Group Report[32] and an upcoming publication, and the work presented in chapter 5 will be submitted shortly after the completion of this thesis to arXiv and to JHEP for publication.

Chapter 2

Multiple Higgs and Vector Boson Production

2.1 Overview

The discovery of the Higgs in 2012[10, 11] means that we now have, in some sense, experimental confirmation for the mechanism responsible for electroweak symmetry breaking (EWSB). Data strongly favour a spin 0, CP even particle[33–35], and confirms that its coupling to other particles is related to their mass in the way predicted by the standard model Higgs mechanism, earning the particle the name *the* Higgs boson (as opposed to initial discussions of a "Higgs like particle"). However, despite this success, its couplings are still imprecisely measured. Possible deviations from SM values of Higgs coupling to vector bosons can be as large as 15% to 40% and for fermions as large as 30% to 100% depending on assumptions and particle type, whilst still being consistent with LHC data[1][27–29]. As many BSM models predict only small (0 - 30%) deviations from SM couplings (when constraints from outside the Higgs sector have been taken into account), these have not been ruled out. In particular, composite Higgs models are models where EWSB is caused by new strong dynamics with the Higgs arising as a pseudo-Goldstone boson (analogous to the pion in QCD). When these models are required to satisfy electroweak precision measurements, then they generally predict de-

[1]With such large deviations still possible, you may ask why is this hailed as such a success for the standard model. The reason is that the masses and related couplings vary over many orders of magnitude between particles, and in this context a $\sim 30\%$ deviation is very small.

viations from SM couplings $\lesssim 10\%$, and hence are also in agreement with current data[2]. In fact the Higgs arising in Technicolor models can be exactly SM-like in terms of their couplings to weak bosons, despite their compositeness[36].

To differentiate between the standard model Higgs, and one which arises due to strong dynamics, we note that it has been shown that a hallmark of strong interactions in the EWSB sector is multiple particle production at energies around the EWSB scale[37]. Therefore in a strongly coupled EWSB sector, one would expect copious production of longitudinal gauge bosons as long as enough energy is available to produce them. This is similar to the way large numbers of pions are produced in QCD at high energies. In fact, multi-W production was studied in a simplified scaled-up version of QCD over 20 years ago [38].

Here we study the inelastic production of longitudinally polarised W and Z bosons (denoted collectively by V_L) and Higgs bosons using a non-linear effective Lagrangian, where couplings can differ from their standard model values. As discussed in [39], the scale of new physics is likely to be where inelastic scattering becomes important. This is what occurs in QCD where multiple pion production indicates the scale at which quarks become important individual degrees of freedom. Analogously we are able to estimate the energy scale of new physics for different coupling values in our effective Lagrangian by calculating the energy at which multiple vector boson or Higgs boson processes become relevant.

As will be discussed in sections. 2.2 and 2.4, the cross section of such multiparticle production should be more sensitive to non-SM couplings than simple $2 \to 2$ processes. In particular, we're interested in how sensitive these multiparticle production cross section are to deviations from the SM couplings.

We first study as a simple case, unitarity violation in multi-V_L production in the Higgsless model [40], before considering models with partial unitarisation, such as the composite Higgs model. Even with partial unitarisation we show that provided enough energy is available to produce the particles, large enhancements of multiparticle cross section can occur. This effect becomes more acute as the final state multiplicity increases.

[2]Although it should be noted that these models are strongly tuned and do not solve the gauge hierarchy problem.

2.2 Multiparticle cross sections and unitarity

In an inelastic $2 \to n$ process, if we assume s-wave dominance, the perturbative unitarity bound on the cross section for a given centre-of-mass energy $\sqrt{s}$ is [40, 41]:

$$\sigma(2 \to n) < \frac{4\pi}{s}. \tag{2.1}$$

(The derivation is reproduced in Appendix A for convenience.)

This bound subsequently sets stringent constraints on the scattering amplitudes. The relativistic $n-$body phase space is proportional to s^{n-2} and therefore, taking into account the flux, the unitarity bound requires that the amplitude grows with energy no faster than

$$A(2 \to n) \sim s^{1-n/2}. \tag{2.2}$$

We can use this result to easily calculate whether scattering in a model will violate the unitarity bound unless there are precise cancellations between amplitudes. As an example, if we neglect transverse gauge bosons and the Higgs boson, we can describe vector boson scattering with a simple nonlinear sigma model (NLσM):

$$\mathcal{L}_{NL\sigma M} = \frac{v^2}{4}\mathrm{Tr}\left[\partial_\mu U \partial^\mu U^\dagger\right] \tag{2.3}$$

where $v = 246$ GeV is the usual scale of electroweak symmetry breaking and

$$U = e^{\frac{i\vec{\tau}\cdot\vec{\pi}}{v}}. \tag{2.4}$$

These scalar "pion" fields π^i $(i = 1, 2, 3)$ describe massless Goldstone bosons in a Higgsless model. The equivalence theorem [37] shows that in the high energy limit the scattering cross sections of longitudinal vector bosons asymptotes to that of their respective massless Goldstone bosons, allowing these π^i fields to be identified with the longitudinally polarised vector bosons.

Using power-counting, we see that the scattering amplitude in this model grows with energy as

$$A_{NL\sigma M}(2 \to n) \sim \frac{s}{v^n} \tag{2.5}$$

and hence naively

$$\sigma(2 \to n) \sim \frac{1}{s}\left(\frac{s}{v^n}\right)^2 s^{n-2}. \tag{2.6}$$

Therefore, we see that the growth of the cross section towards the unitarity bound in this model is faster for larger number of particles, due to the s^{n-2} factor from phase space.

In turn, this means that if we assume that unitarity is restored by new physics, then there must be larger cancellations between scattering amplitudes as the number of final state particles is increased. For example, equation 2.2 tells us that unitarity requires that $A(2 \to 2) \sim$ constant, while $A(2 \to 4) \sim 1/s$, whereas they both grow as $\sim s$ in the NLσM (2.5). Therefore, in the absence of a perfect cancellation between amplitudes, cross section will scale with energy more rapidly for multi-V_L production compared to $2 \to 2$ scattering, and this is likely to have a large impact on multi-V_L production cross sections. The purpose of the work in this chapter is to examine this impact.

2.3 Naive estimates of unitarity violation

The $n-$body phase space in the relativistic limit, (given for example by [42]) is:

$$R_n(s) = \int \prod_{i=1}^{n} \frac{d^3p_i}{(2\pi)^3(2E_i)^3}(2\pi)^4\delta^4(\sqrt{s} - \sum_{i=1}^{n} p_i) = \frac{(2\pi)^{4-3n}(\pi/2)^{n-1}}{(n-1)!(n-2)!}s^{n-2}. \tag{2.7}$$

Rearranging enables us to estimate the energy scale Λ_n at which perturbative unitarity is violated in $2 \to n$ processes in the NLσM:

$$\Lambda_n = \left[\frac{2(n-1)!(n-2)!}{(2\pi)^{3-3n}(\pi/2)^{n-1}}\right]^{\frac{1}{2n}} v. \tag{2.8}$$

Comparing different values of n, we see that the lowest limit occurs for $2 \to 2$ scattering, with unitarity being violated in $2 \to 4$ at an energy which is 2.4 times higher. In this rough estimate we do not include a proper phase space integration or the growth due to the combinatorial factors, however this estimate is in reasonable agreement with the results of a full numerical calculation given in [40].

2.4 Anomalous Higgs couplings and partial unitarisation

In order to recover unitarity, the non-linear sigma model must have a UV completion. The simplest possibility is the addition of a scalar field. This makes the theory consistent with the Higgs boson discovery, and the scalar can be identified with the Higgs. Given exactly SM couplings, new Feynman diagrams involving the Higgs cause large cancellations between amplitudes, restoring unitarity at all scales. However, if the Higgs arises as a composite particle in a strong theory it may have couplings which differ from the SM values. In this case, if the high scale theory giving rise to the composite Higgs isn't considered, then the theory isn't UV complete, cancellations are incomplete and unitarity is only partially restored. Such a theory can be described by an effective Lagrangian which parameterises the Higgs self-couplings and couplings to longitudinally polarised gauge bosons [43]:

$$\begin{aligned}\mathcal{L}_{\text{eff}} &= \frac{v^2}{4}\left(1+2a\frac{h}{v}+b\frac{h^2}{v^2}+b_3\frac{h^3}{v^3}+\cdots\right)\text{Tr}\left[\partial_\mu U\partial^\mu U^\dagger\right] \\ &+ \frac{1}{2}(\partial_\mu h)^2-\frac{1}{2}m_h^2h^2-d_3\lambda v h^3-d_4\frac{\lambda}{4}h^4+\cdots \end{aligned} \tag{2.9}$$

(couplings to fermions are not relevant to the results presented here).

This parameterisation describes the low energy behaviour of a large class of models, including composite Higgs models, and has been used to study anomalous Higgs couplings in $V_LV_L \to V_LV_L, hh$ processes at the LHC [43–45]. Unitarity is recovered for the SM values:

$$\begin{aligned} a = b = d_3 = d_4 = 1 \\ b_3 = 0 \end{aligned} \tag{2.10}$$

while for different values of these parameters the usual cancellation provided by the Higgs is incomplete. With SM coupling values, we can embed the h in the multiplet,

$$\Phi \equiv \left(1+\frac{h}{v}\right)U \tag{2.11}$$

from which we can recover the usual linear sigma model.

Whilst in general, the parameters in the Lagrangian can be independent, many models predict relations between them. For example, in Minimal Composite Higgs Model (MCHM4)[3], the couplings of the "pions" with the Higgs boson follows from an expansion around the vacuum $h(x) = 0$ of the effective Lagrangian [48]

$$\frac{f^2}{4}\sin^2\left(\theta + \frac{h(x)}{f}\right)\mathrm{Tr}\left[\partial_\mu U \partial^\mu U^\dagger\right] \tag{2.12}$$

with $v = f\sin\theta$, which comes from the mass term for the gauge fields. In the MCHM4 we therefore have a relation between the coupling, which can ultimately be parameterised in terms of a single variable ξ,

$$a = \sqrt{1-\xi};\;\; b = 1-2\xi;\;\; b_3 = -\frac{4}{3}\xi\sqrt{1-\xi};\;\; \cdots \tag{2.13}$$

Although not obvious from the Lagrangian in Equation 2.9, in a physically equivalent set of coordinates, this Lagrangian has a discrete symmetry under the parity transformation $h \to -h$ and $\pi \to -\pi$[48].

In order to study the $2 \to 4$ scattering, we must expand each field U to order $\mathcal{O}(\pi^6)$:

$$\begin{aligned}\frac{v^2}{4}\mathrm{Tr}\left[\partial_\mu U \partial^\mu U^\dagger\right] &= \frac{1}{2}\left(\partial^\mu\vec{\pi}\cdot\partial_\mu\vec{\pi}\right) + \left[1 - \frac{2}{15v^2}\vec{\pi}\cdot\vec{\pi}\right] \\ &\times\frac{1}{6v^2}\left[\left(\vec{\pi}\cdot\partial_\mu\vec{\pi}\right)^2 - \left(\vec{\pi}\cdot\vec{\pi}\right)\left(\partial^\mu\vec{\pi}\cdot\partial_\mu\vec{\pi}\right)\right] + \mathcal{O}(\vec{\pi}^8)\end{aligned} \tag{2.14}$$

The number of diagrams increases considerably with the number of final state particles, making it impractical to perform an analytic computation. Therefore we implemented the Lagrangian given in Equation 2.9 both in FormCalc [49] and MadGraph [50] using FeynRules [51] (with UFO output [52] for the higher dimensional operators) and in CalcHEP [53] using LanHEP package[54] with the help of auxiliary fields.

In the remainder of this section the $\pi^{0,+,-}$ fields will be referred to as "pions", but it should be remembered that these are identified with the Goldstones from the Higgs field and ultimately the longitudinally polarised vector bosons, V_L.

In the simplest case of $2 \to 2$ scattering, amplitudes only depend on the Mandel-

[3]In the MCHM the fermions can be embedded in either the spinorial or fundamental representation of $SO(5)$, denoted by MCHM4[46] and MCHM5 respectively[47].

stam variables s and t. For instance if we assume the pions are massless, which is valid in the high energy scenario, the $\pi^0\pi^0 \to \pi^+\pi^-$ amplitude arising from only 2 diagrams, one with a 4 point interaction and one with an s-channel Higgs, is given by:

$$\mathcal{M}_{\pi^0\pi^0;\pi^+\pi^-} = \frac{s\left[(1-a^2)s - m_h^2\right]}{v^2(s-m_h^2)} \underset{s\gg m_h^2}{\longrightarrow} (1-a^2)\frac{s}{v^2}. \tag{2.15}$$

Equation 2.2 tells us that unitarity requires in this case that the amplitude to be at most constant with s at high energies. We see therefore that there is a violation of unitarity even with the presence of the Higgs boson if its coupling is not SM-like, *i.e.*, $a \neq 1$. This also demonstrates that in the SM the amplitude is constant at high energies as required by unitarity.

The $2 \to 4$ amplitudes are far more complicated. They containing of the order of 100 diagrams and with multiple combinations of the scalar products of the different 4-momenta involved. However, we can elucidate the high energy behaviour of the cross section by focusing on a given point in phase space, with the assumption that the overall behaviour will be the same in general. In this particular case, all the particles lie in the same plane, in which case we obtain,

$$\begin{aligned}\mathcal{M}_{\pi^0\pi^0;\pi^0\pi^0\pi^+\pi^-} \propto \tfrac{1}{v^4}\big[&72s\left(13a^4 - a^2(7b+5) - 1\right) + \\ &3m_h^2\left(1580a^4 - 378a^3d_3 - 3a^2(245b+131) - 74\right) + \\ &\tfrac{m_h^4}{s}\left(9774a^4 - 3087a^3d_3 - a^2(4494b+1289) + 52\right) + \\ &\cdots\big]\end{aligned} \tag{2.16}$$

Once more, we see that it's leading term grows with s, as expected from power counting. However, in the SM (where $a = b = d_3 = 1$, see Equation 2.10) cancellations occur and the first two terms in powers of s vanish. In the $s \gg m_h^2$ limit we obtain:

$$\mathcal{M}_{\pi^0\pi^0;\pi^0\pi^0\pi^+\pi^-} \propto \frac{1}{s}\frac{m_h^4}{v^4} \tag{2.17}$$

demonstrating the behaviour change from $\sim s$ to $\sim 1/s$ required for unitarity. Equation 2.16 shows that the triple Higgs anomalous coupling parameterised by d_3 does not enter in the dominant contribution, and therefore in the following we will take $d_3 = 1$. Also

note that the d_4 and b_3 couplings do not contribute to the above processes.

For $2 \to 3$ processes a similar analysis can be performed. For $\pi^0\pi^0 \to hhh$, again for a given configuration in phase space, the result is

$$\begin{aligned}\mathcal{M}_{\pi^0\pi^0;hhh} \propto \tfrac{1}{4v^3}\Big[s\left(-4a^3+4ab-3b_3\right)\big) - \\ m_h^2\left(-8a^3+8ab+3b_3\right) + \\ \tfrac{4m_h^4}{s}\left(a^3+ab-6b_3-3a^2d_3\right)+\cdots\Big],\end{aligned} \tag{2.18}$$

while for $\pi^0\pi^0 \to \pi^+\pi^- h$ for a configuration where the 2 final state pions are collinear with each other but back-to-back with the Higgs boson we find

$$\begin{aligned}\mathcal{M}_{\pi^0\pi^0;\pi^+\pi^- h} \propto \tfrac{a}{192v^3}\Big[s\left(-1+2a^2-b\right)+ \\ \tfrac{m_h^2}{4}\left(-164+386a^2-213b-9ad_3\right)- \\ \tfrac{3m_h^4}{2s}\left(-262+291a^2-93b+81ad_3\right)+\cdots\Big]\end{aligned} \tag{2.19}$$

Once more we find that for the SM, the first two terms in these amplitudes vanish as required. It is also worth noticing that the $\mathcal{M}_{\pi^0\pi^0;hhh}$ amplitude depends on b_3, being the lowest multiplicity process which is sensitive to this coupling. In addition, if we substitute the values for the coupling in terms of ξ so that they obey the MCHM4 relations in Equation 2.13, we find that cancellations occur and the highest power of s in the amplitude of these $2 \to 3$ processes vanishes. In fact, this can be anticipated from the parity of the MCHM4 class of theories, under which $\pi \to -\pi$ and $h \to -h$ [48].

In summary, we see that neglecting any special symmetries such as in the MCHM4, if the couplings do not have their SM values, the amplitude always grows as s regardless of the number of final state particles. However the requirement for unitarity becomes more stringent as the numbers of final state particles increases due to the increase phase space, requiring the amplitude to grow no faster than $s^{1-\frac{n}{2}}$ at high energy for a $2 \to n$ process. Therefore, as predicted for the Higgsless scenario, the $2 \to 3$ and $2 \to 4$ processes have cross sections which increase more quickly with energy than they do for $2 \to 2$ processes, and depending on total cross sections these higher multiplicity channels may provide more sensitivity at the LHC to non-SM Higgs couplings. In the next section

we evaluate these cross sections in order to quantify this sensitivity.

2.5 Sensitivity of $2 \to 3, 4$ cross section to anomalous couplings

In this section, we analyse the cross sections for the $2 \to 2$, $2 \to 3$ and $2 \to 4$ processes at the parton level (i.e. for example $\pi^0\pi^0 \to \pi^+\pi^-\pi^+\pi^-$), with a fixed centre-of-mass energy of $\sqrt{s} = 1$ TeV, and Higgs mass of 125 GeV. We use a model given by the effective Lagrangian in Equation 2.9 which was implemented in CalcHEP using LanHEP to generate the model file from the Lagrangian.

In the SM, the Higgs does not decay to a pair of on-shell gauge bosons, and therefore is never on-mass-shell when coupled to two gauge bosons. On the other hand, in our effective model, the pions are massless, and so to ensure that the propagating Higgs in this case is also off shell, we implemented an invariant mass cut on our final state pions of $m_{\pi^+\pi^-} > 200$ GeV.

The effect on the cross-section of varying a, (which scales the hV_LV_L coupling, with $a = 1$ being the SM value) is shown in Figure 2.1, where the y-axis is presented in terms of the ratio of the cross section to the cross section when $a = 1$. In Figure 2.1(a), the parameter a is varied keeping all other parameters fixed, whilst in Figure 2.1(b) we model effects in the MCHM4 by altering the other parameters according to Equation 2.13 along with $d_3 = \sqrt{1-\xi}$[44].

We see that very large enhancements of the order of 10^3 – 10^5 with respect to the SM value are obtained, and that the majority of this increase is present even for relatively small deviations, with an $\mathcal{O}(10^2$ – $10^4)$ increase for $a = 0.9$. The largest increases are observed for triple Higgs production. Note that the cross section versus a for $2 \to 2$, $2 \to 3$ and $2 \to 4$ processes have 2, 3 and 4 dips respectively, which can be easily understood by noting from equations 2.15–2.19 that the amplitudes are 2^{nd}, 3^{rd} and 4^{th} order polynomials in a. We see that the enhancements in $2 \to 2$ processes are modest compared to the large enhancements which occur for higher multiplicities due to the increased phase space (at least at 1 TeV).

When the couplings are related as required for the MCHM4, the increases are

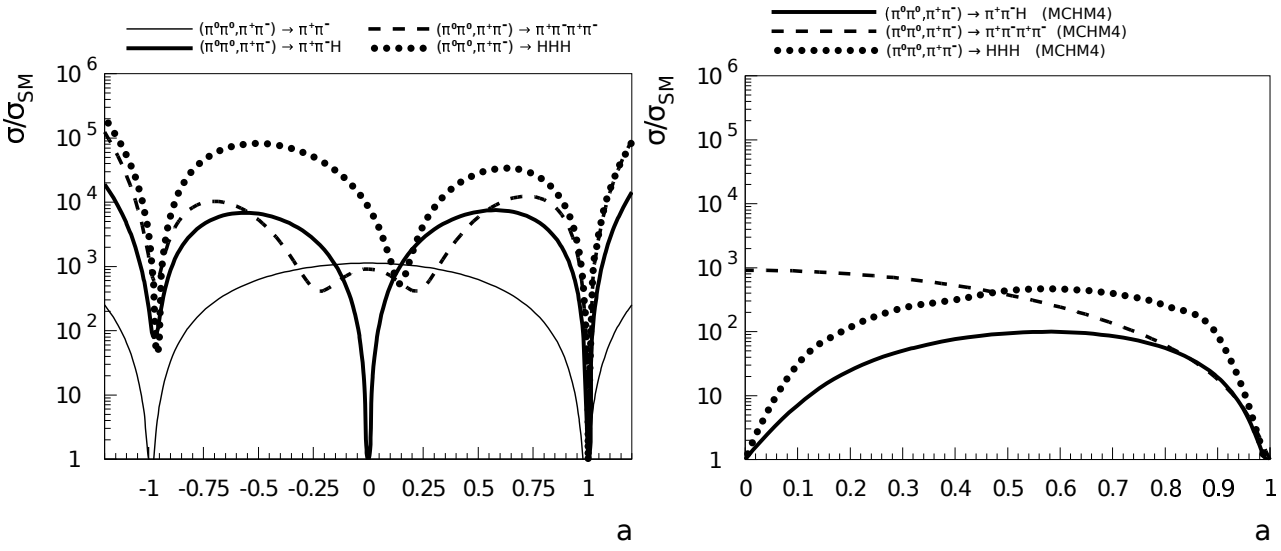

(a) (b)

Figure 2.1: *Ratio of the cross sections to the SM cross section as a function of the "a" coupling parameter, where $\sqrt{s} = 1$ TeV: (a) the general effective Lagrangian with all other parameters fixed at their SM values; (b) other couplings fixed according to the MCHM4 relations. The different channels are: $(\pi^0\pi^0, \pi^+\pi^-) \to \pi^+\pi^-\pi^+\pi^-$ (dashed line), $(\pi^0\pi^0, \pi^+\pi^-) \to \pi^+\pi^- h$ (thick solid line), $(\pi^0\pi^0, \pi^+\pi^-) \to hhh$ (dotted line), and $(\pi^0\pi^0, \pi^+\pi^-) \to \pi^+\pi^-$ (thin solid line) for comparison. The notation $(\pi^0\pi^0, \pi^+\pi^-)$ indicates that both $\pi^0\pi^0$ and $\pi^+\pi^-$ initial states were taken into account.*

smaller as expected from the parity symmetry of the coset. Since the MCHM4 always predicts smaller deviations, in what follows we will consider the more optimistic case where the parameter a varies independently, with the other parameters fixed.

We showed in section 2.4 that in the case of partial unitarisation, $\sigma(2 \to n) \sim \frac{1}{s}\left(\frac{s}{v^n}\right)^2 s^{n-2}$ as in the Higgsless case. To explore this, we next study the growth of the cross section with centre-of-mass energy for different numbers of final state particles. We consider a few different values of the anomalous coupling, namely $a = 0.9$, 0.95 and 1 (SM), keeping the other couplings at their SM values.

The results are shown in Figure 2.2(a) and (b), where the cross section of representative processes with $2, 3$ and 4 particles in the final state are plotted for different values of the coupling parameter a. The shaded area at the top right of each plot is the unitarity bound from equation 2.1. Both (a) and (b), demonstrate that as expected, the SM cross section (with $a = 1$) for each process quickly stabilises at a small value due to the cancellations between amplitudes, with the precise value depending on the final state. In the non-SM case, without these cancellations, the cross sections grow

rapidly with energy, reaching up to order 100 pb and violating unitarity at centre-of mass energies of the order of a few TeV. Also, as anticipated we see that for processes with higher numbers of particles in the final state, the incomplete cancellation between amplitudes allows the increased phase space to lead to a faster growth in cross section with energy. However, what was somewhat unexpected is the relatively low energy scale at which multiparticle cross sections can become comparable to $2 \to 2$ processes. The $2 \to 3$ cross sections start to become larger than that of the $2 \to 2$ process at energies of $\mathcal{O}(1\text{TeV})$. This might be signalling the onset of non-perturbative behaviour well before the unitarity bound is reached, and it may be that new physics such as the appearance of new resonances must come in at these scales. However, for this work we assumed that this is not the case. For the $2 \to 4$ process the cross section grows very rapidly for non-SM couplings, however as it starts off very suppressed, it only surpasses the $2 \to 2$ at high energies of the order of $\mathcal{O}(5\text{TeV})$.

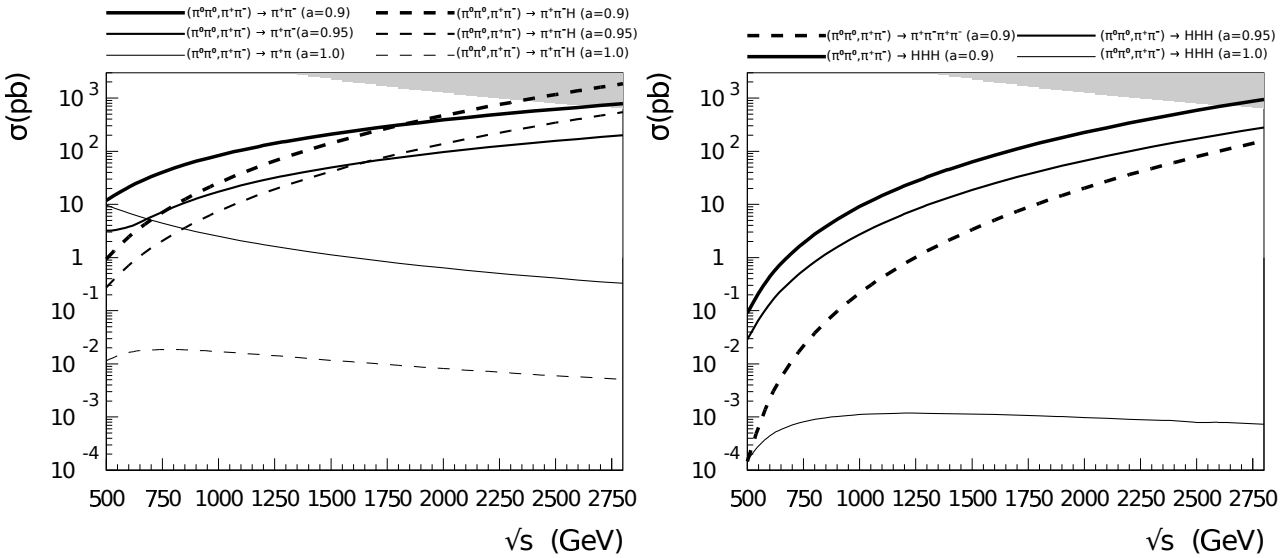

(a) (b)

Figure 2.2: *Comparison of cross sections as a function of the centre-of-mass energy for processes with* $2, 3$ *and* 4 *particles in the final state. (a) the solid lines are for* $(\pi^0\pi^0, \pi^+\pi^-) \to \pi^+\pi^-$ *for* $a = 0.9$ *(thick),* $a = 0.95$ *(medium thick) and* $a = 1$ *(thin). Dashed lines are for* $(\pi^0\pi^0, \pi^+\pi^-) \to \pi^+\pi^- h$*, with the same pattern for the thickness of the lines. (b) The same pattern of lines show the results* $(\pi^0\pi^0, \pi^+\pi^-) \to hhh$ *and the process* $\pi^0\pi^0 \to \pi^+\pi^-\pi^+\pi^-$ *is shown as a dashed line for* $a = 0.9$*. In these plots only the coupling parameter a deviates from the SM value. The unitarity bound is shown as a shaded area in the top right corner.*

2.6 Cross sections in the SM with anomalous Higgs couplings

So far we've only analysed the scattering of the longitudinally polarised gauge bosons. In an experimental setting, it's difficult to separate out these contributions from the transversely polarised bosons. Therefore, it's important to understand how the large enhancements in the scattering of longitudinally polarised will affect the full, unpolarised cross section. To do this, we promote the partial derivatives of our effective Lagrangian (Equation 2.9) to full covariant derivatives and adopt the unitary gauge ($U = \mathbf{1}$).

The results are presented in Table 2.1, where these unpolarised cross sections are compared to the pure longitudinally polarised vector boson scattering as describe in the previous section. We keep the notation π^0, $\pi^\pm$ to indicate longitudinally polarised scattering and $Z, W^\pm$ to denote the unpolarised gauge bosons. We compare results with partonic centre-of-mass energy of both 1 TeV and 2 TeV, both of which are below the unitary bound for the $a = 0.9$ case considered due to partial unitarisation.

Channel	$a = b = 1$ (SM)	$a = 0.9; b = 1$
$\pi^0\pi^0 \to \pi^+\pi^-$	0.53 (0.13)	66.4 (295)
$ZZ \to W^+W^-$	629 (610)	646 (655)
$\pi^0\pi^0 \to \pi^+\pi^- h$	4.6×10^{-3} (2.0×10^{-3})	18.7 (350)
$ZZ \to W^+W^- h$	5.49 (10.9)	6.17 (46.2)
$\pi^0\pi^0 \to hh$	0.64 (0.18)	43.0 (158)
$ZZ \to hh$	7.18 (7.61)	4.31 (15.7)
$\pi^0\pi^0 \to hhh$	5.6×10^{-4} (4.9×10^{-4})	4.5 (112)
$ZZ \to hhh$	1.7×10^{-2} (4.7×10^{-2})	0.61 (13.6)

Table 2.1: *Comparison of* $2 \to 2$ *and* $2 \to 3$ *cross sections (in picobarns) at* $\sqrt{s} = 1$ *TeV* ($\sqrt{s} = 2$ *TeV in parenthesis). The notation* π^0, $\pi^\pm$ *indicates longitudinally polarised bosons and* $Z, W^\pm$ *denotes unpolarised gauge bosons.*

The first thing to note is the large degree to which longitudinal polarisations are subdominant in the standard model, with the unpolarised cross section being $\mathcal{O}(10^1$ – $10^3)$ larger than the purely longitudinally polarised case. However, as discussed, they are greatly enhanced with a 10% deviation where $a = 0.9$, and come to dominate the cross section in all the cases with a Higgs in the final state. As anticipated, the enhancements are larger for larger final state multiplicities, with for example a $\mathcal{O}(10^2)$ enhancement in $\sigma(\pi^0\pi^0 \to \pi^+\pi^-)$ and an $\mathcal{O}(10^{3-4})$ enhancement for $\sigma(\pi^0\pi^0 \to \pi^+\pi^- h)$ at 1 TeV when

going from $a = 1$ to $a = 0.9$.

Unfortunately, we also see that when all polarisations are included, the large increase observed in purely longitudinal scattering is often masked. This is due in part to the fact that whilst the longitudinally polarised contribution to the cross section increases when $a(1.0 \to 0.9)$, the initially larger transverse component reduces. This is to be expected because for processes involving transverse polarisations the couplings are also scaled with a, and hence the amplitude scales with a power of a which depends on the number of relevant vertices in the Feynman diagram. For example for $\sigma(\pi^0\pi^0 \to \pi^+\pi^- h)$, a enters as a^3 for some diagrams. If these were the dominant diagrams, this would naively give us a scaling of the cross section of $a^6 \sim 50\%$ for $a = 0.9$. If we combine this with the fact that the longitudinally polarised cross sections quoted in Table 2.1 assume that both incoming partons are longitudinally polarised, and so should be divided by 9 due to averaging over spins before comparing to the unpolarised cross sections, we see why many of the cross sections do not increase much. In fact for $ZZ \to hh$ the cross section decreases. Interference between diagrams involving transversely polarised bosons may also play a role but this was not explored further. As a concrete example, despite the cross section for $\pi^0\pi^0 \to \pi^+\pi^- h$ being 3 times larger (18.7 pb) than for the unpolarised case, $(\sigma(ZZ \to W^+W^- h) = 6.17)$ when $a = 0.9$, the total increase in the unpolarised cross section is only $\sim 10\%$ at 1 TeV.

On the other hand, in cases where the initial contributions from the transverse polarisations are small, as in $ZZ \to hhh$, enhancements factors of around 35 and 300 are obtained at 1 TeV and 2 TeV respectively. Its enhanced cross section is however still 1 to 2 orders of magnitude smaller than the other processes considered.

Finally, in all channels, the degree of enhancement for anomalous couplings were larger for 2 TeV than 1 TeV as expected due to the $\mathcal{M} \propto s$.

It is difficult at this point to conclude for certain which process offers the best channel to study anomalous couplings, and the answer is likely to depend on the energy of collision. Triple Higgs production is a promising channel due to the low transverse background and very large factors of increase in cross sections, although the fact that its cross section is still relatively low is against it. $ZZ \to W^+W^- h$ on the other hand has a more modest factor of increase (at 2 TeV), but a higher overall cross section.

2.7 Impact of multiparticle production at the LHC and future colliders

Thus far we have studied scattering at parton level, essentially simulating the collision of beams of vector bosons. In order to estimate how these results would manifest at the LHC or other future colliders, we used Madgraph5 (v1.4.8) to perform a full calculation of $pp \to jj + X$, where $j = u, \bar{u}, d, \bar{d}, s, \bar{s}$ and $X = W^+W^-, W^+W^-h, hhh$. We evaluated tree-level cross sections at $\sqrt{s} = 14$ TeV and 33 TeV[4], using the CTEQ6L1 parton density function and the QCD scale equal to M_Z.

Such proton-proton collisions, as well as containing the vector-boson fusion/scattering discussed in the previous section, also contain many additional diagrams leading to the requested final products. Many of these additional diagrams do not contain the anomalous Higgs-vector-vector coupling, and so they will not exhibit the cross section enhancements discussed, likely simply contributing to the overall cross section, acting as a background to our BSM process and obscuring the enhancements we seek. If we are able to select mainly events *with* vector boson fusion (VBF), then we limit ourselves to diagrams which *do* contain the relevant processes discussed previously and we are more likely to observe enhancements. Therefore, we evaluated 2 sets of cross sections, one with and one without cuts selecting for vector boson fusion.

The acceptance cuts which we applied to all events are:

$$\begin{aligned} \text{Acceptance cuts:} \qquad & p_{T_j} > 30 \text{ GeV} \\ & |\eta_j| < 5.0 \\ & \Delta R_{jj} = \sqrt{\Delta\phi_{jj}^2 + \Delta\eta_{jj}^2} > 0.4 \end{aligned}$$

In addition, we produced a set of events with additional VBF cuts:

$$\text{VBF cuts:[56]} \quad E_j > 300 \text{ GeV} \tag{2.20}$$

$$\Delta\eta_{jj} > 4. \tag{2.21}$$

[4] At the time of this study, 33 TeV was being discussed as a possible energy for the High Energy LHC upgrade. Now the possibility of a 100 TeV collider is being considered for which we are updating these results[55].

The basic idea behind the VBF cuts is that the vector bosons tend to be radiated from a high energy quarks, one from each proton, which then continue with a small angle from the beam pipe. Therefore the signature is of 2 high energy jets which are back to back and therefore have a large rapidity gap between them. The QCD background on the other hand tends to produce more central jets and generally fail to pass these cuts. (For a more detailed motivation of this choice of cuts see e.g. [56]).

In Table 2.2 we present these results both with vector boson fusion cuts, and without these cuts in parenthesis.

Process	14 TeV		33 TeV	
	with (without) VBF cuts		with (without) VBF cuts	
	a=1.0 b=1.0	a=0.9 b=1.0	a=1.0 b=1.0	a=0.9 b=1.0
$pp \to jjW^+W^-$	95.2 (1820)	99.3 (1700)	512 (5120)	540 (5790)
$pp \to jjW^+W^-h$	0.011 (0.206)	0.0088 (0.172)	0.0765 (0.914)	0.0626 (0.758)
$pp \to jjhhh$	1.16×10^{-4} (3.01×10^{-4})	0.0566 (0.0613)	0.00151 (0.00237)	2.02 (2.07)

Table 2.2: *Cross section (in fb) for $pp \to jjW^+W^-$, $pp \to jjW^+W^-h$ and $pp \to jjhhh$ processes evaluated with Madgraph5. There are two values of the cross sections for each entry, with the number in parenthesis being the cross section without VBF cuts.*

The first thing to note is that the overall pattern is similar to that found for the parton level scattering in the previous section. In processes with gauge bosons in the final state, we see either a small increase or a small reduction in cross sections as $a(1.0 \to 0.9)$, occurring as discussed previously due to the reduction in amplitudes involving transverse bosons. We also see that the VBF cuts (results *not* in parenthesis), successfully isolate a larger proportion of processes involving longitudinal scattering for $pp \to jjW^+W^-$, leading to an small increase in cross section for anomalous coupling instead of a reduction in the more inclusive case. For $pp \to jjW^+W^-h$ this does not occur, presumably as the overall increase in the longitudinal scattering was too small.

For the triple Higgs production on the other hand, the enhancements remain substantial. With anomalous couplings, there's roughly a factor of 500 increase for $\sqrt{s} = 14$ TeV (LHC14) and 1300 for $\sqrt{s} = 33$ TeV (LHC33), with VBF cuts.

As this remains the only promising channel at the energies considered, we show in Figure 2.3 the results for the $pp \to jjhhh$ cross section for both LHC14 and LHC33 with anomalous coupling $0.5 < a < 1.5$. We also include the results for where the other parameters are altered simultaneously according to the MCHM4 relations given in Equation 2.13. We observe that for anomalous couplings, the enhancements with respect to the SM case ($a = 1$) are large. The majority of this increase occurs by $\Delta a \sim 0.1$, so that there is little advantage in terms of cross section in having deviations $> 10 - 15\%$ from the standard model (which are anyway generally disfavoured in composite Higgs models). As in section (2.5) the increases for the MCHM4 as smaller due to the parity symmetry of the coset.

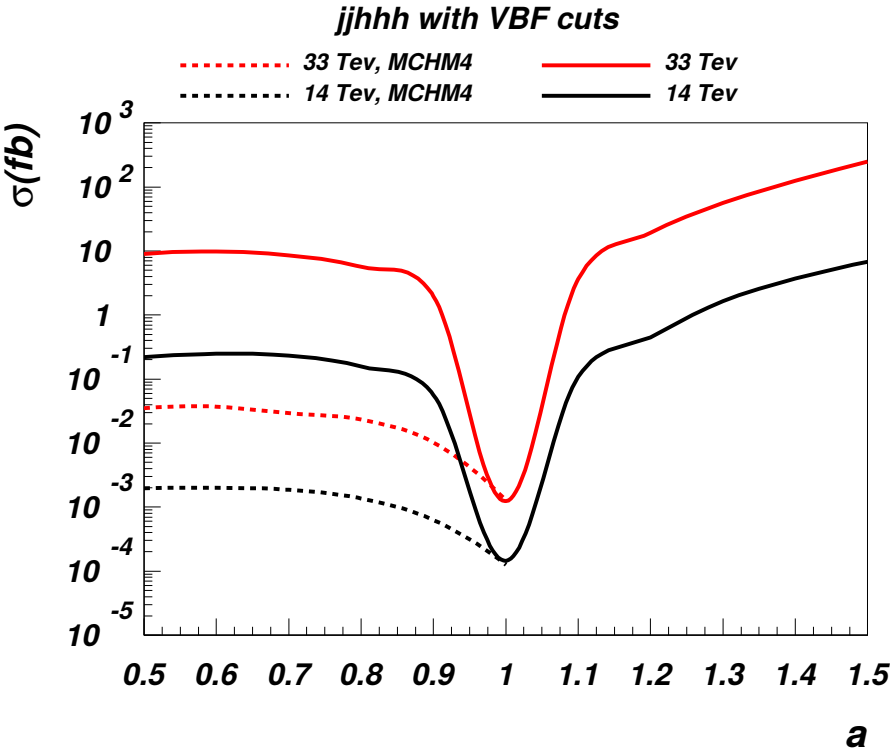

Figure 2.3: *Cross section for triple Higgs production $pp \to jjhhh$ with VBF cuts as a function of the anomalous coupling a for LHC14 (dark lines) and LHC33 (light lines). Solid lines are for other parameters fixed to SM values and dashed lines are for parameters given by MCHM4 relations (Equation 2.13).*

For the case where other couplings are set to their SM value (solid line), the

enhancement can be as large as 10^5 for $a = 1.5$. However even in this extreme case, the absolute value of the cross section is quite low (about 10 fb for $\sqrt{s} = 14$ TeV with VBF cuts) making the study of these processes challenging at the LHC. A dedicated analysis would be required to accurately understand the LHC14 or LHC33 sensitivity, however we can already see that to have any realistic prospect of observing this process we would require high integrated luminocities. There are currently early proposals for a future 100 TeV hadron collider. As the increase in cross section scales rapidly with energy, such a collider seems likely to be able to probe these couplings and processes, but would be the subject of further study[55].

2.8 Conclusion

We have studied multiparticle production in models with anomalous Higgs couplings, such as the composite Higgs models. These modified couplings result in a partial unitarization of the scattering amplitudes. We found that at high energies, the amplitudes scale linearly with centre-of-mass energy squared, s, irrespective of the number of particles in the final state. Therefore, due to the phase space, the cross section increases more rapidly with energy for larger multiplicity processes, and very large enhancements in cross sections compared to the SM can arise. These can be as large as $\mathcal{O}(10^5)$, even for relatively small deviations of the couplings. The increased growth of the cross sections with energy for larger multiplicities is however in competition with the fact that more energy is required to produce the larger number of final state particles, with the results that $2 \to 4$ processes are less relevant than $2 \to 3$ processes at the energies investigated. On the other hand $2 \to 3$ processes can become as important as $2 \to 2$ even at relatively low energies of the order of 1 TeV, which may be signalling the onset of nonperturbative effects. When accounting for the contributions from the transverse polarisations, the enhancements are somewhat diluted but remain important in some processes, especially triple Higgs production.

We also showed with a realistic calculation that even with these large enhancements the search for multiparticle processes will remain a challenge for the LHC run 2 at 14 TeV and for any future upgrade or new experiment at 33 TeV. On the other hand, the enhancements studied increase rapidly with energy, and multiple gauge and Higgs

boson production could be an important way of studying anomalous Higgs couplings in future experimental programs such as a 100 TeV collider.

Chapter 3

$V_L V_L \to V_L V_L$ scattering as a model independent probe of the Higgs coupling to Vector Bosons

3.1 Motivation

The discovery of the Higgs boson at the LHC [10, 11] has ushered in a new era in the study of the electroweak symmetry breaking (EWSB) sector. Since the longitudinal polarisations of the electroweak gauge bosons (V_L's, $V = W^{\pm}, Z$) have their origin in EWSB, determining their interactions is of fundamental importance to unravel the mechanism of EWSB. In Chapter 2, we studied the properties of this sector concentrating on multi-boson production, namely with 3 or 4 particles in the final state, as in this case the relative increase in cross section is larger than for $2 \to 2$ scattering. What we found was that whilst large increases did occur for longitudinally polarised bosons, this increase was obscured by the much larger cross section from transversely polarised bosons, so called "*transverse pollution*", making such processes difficult to observe at the LHC. In this chapter, we look at ways of reducing this transverse pollution. In particular, we consider the simpler $V_L V_L \to V_L V_L$ process with 2 bosons in the final state rather than the multi-boson scattering of Chapter 2. Whilst in this case the increase in cross section is smaller than for multi-boson scattering, the total cross section is generally larger, and it is a sensible simple starting point to begin.

This importance of the scattering of longitudinally polarised gauge bosons has been known for many years. The first calculations of $V_L V_L$ scattering were performed in the context of the so-called Effective W Approximation[1] (EWA) in the 1980s [57–59], with the use of the Goldstone equivalence theorem[60][2]. The first realistic study of $V_L V_L$ scattering in a strongly coupled EWSB sector but assuming the equivalence theorem and EWA and adopting several unitarisation prescriptions were performed in the 1990s [61, 62] (see also [63]). Basic techniques such as forward jet tagging, central jet vetoing, and cuts on the transverse momenta were introduced to select processes with vector boson fusion (VBF). The first studies that went beyond the EWA performing a complete calculation of WW scattering were [64, 65].

As discussed, one of the most difficult issues in extracting the physics of EWSB from VV scattering is the so-called transverse pollution. Much work has been done to devise cuts that can reduce the transverse pollution and this is the subject of this chapter. Below we start with a brief review some of the most recent developments in these efforts.

3.2 Recent developments

Recent developments are based on the different angular distributions of the decay products of transverse and longitudinal gauge bosons. In the gauge boson rest frame, the probability of a fermion decaying at an angle θ^* to the direction of boost to the boson's rest frame depends both on the boson's and the fermion's polarisation, and can be calculated from a simple spin-analysis. For longitudinally polarised vector bosons, this probability is given by

$$P_L(\cos\theta^*) = \frac{3}{4}(1 - \cos^2\theta^*). \tag{3.1}$$

This is consistent with what we would expect from spin considerations, for example, a scattering with $\cos\theta^* = \pm 1$ is disallowed as in this case the sum of the angular momenta of the decay products cannot equal zero in the direction described. For transversely

[1] The Effective W Approximation essentially assumes that we can factorise proton-proton scattering involving vector boson scattering into a term describing the $q \to q'W$ splitting within the proton, and the hard $WW \to WW$ scattering.

[2] The equivalence theorem was introduced in Chapter 2. It states that at high energies the amplitudes for $V_L V_L$ scattering can be calculated using their corresponding Goldstone bosons.

polarised bosons, the distributions are different depending on whether the polarisation of the boson V and respective fermion ψ *coincide* or are *opposite*. P_+ corresponds to a V_{left} (V_{right}) gauge boson decaying to a ψ_{left} (ψ_{right}) fermion, while P_- corresponds to a V_{left} (V_{right}) gauge boson decaying to a ψ_{right} (ψ_{left}) fermion. $P_\pm$ is given by

$$P_\pm(\cos\theta^*) = \frac{3}{8}(1 \pm \cos\theta^*)^2, \tag{3.2}$$

which is consistent with the scattering favouring $\cos\theta^* = +1$ for P_+ and $\cos\theta^* = -1$ for P_- due to the spins of the final state particles summing to +1 and -1 in the chosen direction in these limits. For ease of visualisation and comparison with later results, $P_L(\cos\theta^*)$ and $(P_+(\cos\theta^*) + P_-(\cos\theta^*))$ are plotted in Figure 3.1 (a) and (b). The sum $(P_+ + P_-)$ is plotted as we will usually sum over the two transverse polarisations. Note the very obvious difference in theses two distributions with longitudinally and transversely polarised bosons tending to have small and large values of $|\cos\theta^*|$ respectively.

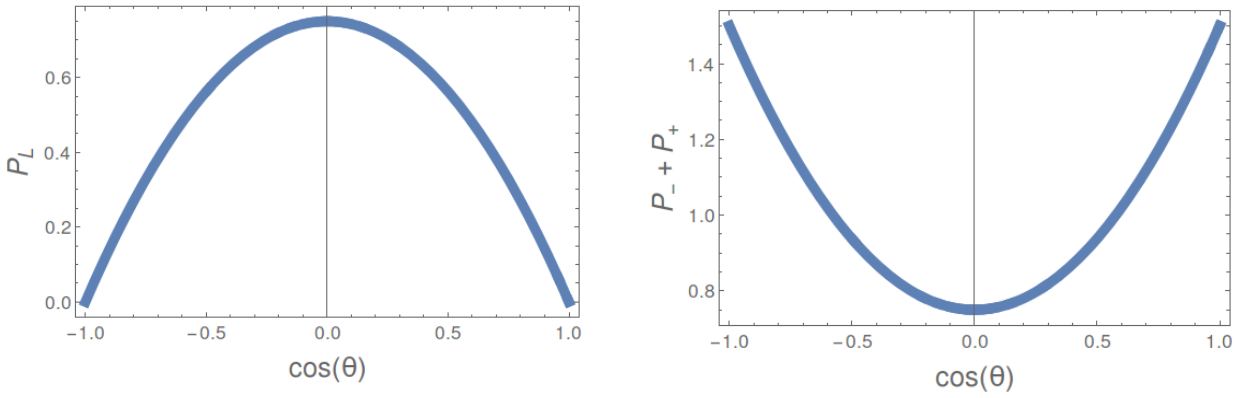

(a) (b)

Figure 3.1: *Plot of; (a)* $P_L(\cos\theta^*) = \frac{3}{4}(1 - \cos^2\theta^*)$*, (b)* $P_+ + P_-$ *where* $P_\pm(\cos\theta^*) = \frac{3}{8}(1 \pm \cos\theta^*)^2$.

Han *et al.* [66] proposed to directly reconstruct the 4-momenta of the decay products of the gauge bosons. This would then enable us to measure the θ^* distribution, and fit it to

$$P(\cos\theta^*) = f_L P_L(\cos\theta^*) + f_+ P_+(\cos\theta^*) + f_- P_-(\cos\theta^*) \tag{3.3}$$

with $f_L + f_- + f_+ = 1$, thus allowing us to directly measure the proportion of gauge

bosons with each polarisation. They showed that the fit is robust against full hadronisation.

Doroba *et al.* [67] proposed a new variable to isolate W_LW_L scattering in same-sign WW production. This variable arose from the observation that W_L's tend to be emitted at smaller angles with respect to the initial quarks compared to the transversely polarised bosons, and hence the final quarks are more forward. Therefore, they required a small transverse momenta of the forward jets in order to improve W_T rejection. Jet substructure techniques used by Han *et al.* to reconstruct hadronically decaying gauge bosons were recently further improved in [68], where a multivariate W jet tagging method is employed. They also used the cuts suggested by Doroba *et al.* [67]. Freitas and Gainer [69] showed that the significance of the VBF signal can be increased by using the matrix element method but further investigation including showering and detector simulation is still required to quantify their findings. More recently, Chang *et al.* [70] used WW scattering to study the sensitivity to additional Higgs bosons in a complete calculation without relying on EWA, employing the usual selection cuts to maximise the VBF contribution.

3.3 Goal of study

In the previous chapter we saw how the problem of transverse pollution can make it very difficult to measure anomalous Higgs couplings at the LHC. Our ultimate goal here is to use the variables and techniques discussed above to find ways to increase the LHC sensitivity to this anomalous coupling and therefore new physics, via VV scattering. We achieve this by, among other things, reducing the transverse pollution. Whilst in chapter 2 we compared the standard model ($a = 1.0$) case with a range of values of a, concentrating mainly on a 10% deviation ($a = 0.9$), in this chapter we compare the 2 most extreme cases, i.e. we compare the SM ($a = 1.0$) with the Higgsless ($a = 0.0$) case. We do this for simplicity, as this is a first study, which could then be expanded later to include intermediate values of a. Also from the work in chapter 2, and in particular Figure 2.1, we know that the increase in cross section in going from $a(1.0 \to 0.9)$ is much larger than the modest further increase in going from $a(0.9 \to 0.0)$, and so we would expect our results for $a = 0$ to be qualitatively valid for the $a = 0.9$ case.

One important point to stress is that the current way to measure a is from direct Higgs production in gluon fusion through the decay $H \to VV^*$. This is somewhat model dependent because of the loop-induced gluon-gluon-Higgs coupling, which is sensitive to any new heavy particles which couple to the Higgs which could enter the loops. In contrast, by relying only on tree level VV scattering, the method describe in this study is more model-independent.

This chapter is organised as follows. In the next section we discuss in a parton level analysis the selection criteria we propose to implement in order to enhance the contribution from the longitudinally polarised gauge bosons. In section 3.5 a preliminary analysis is performed to understand whether the efficiency of the proposed criteria survive at the full proton-proton, $2 \to 6$ level at the LHC. Finally, we conclude the study in section 3.6.

3.4 Analysis at the $VV \to VV$ level

Here we consider the properties of vector boson scattering in the $VV \to VV$ processes, where $V = W^{\pm}, Z$. Although the set of Feynman diagrams for these processes depends on which bosons are present, a representative set of diagrams given in Figure 3.2, in this case for $W^+, W^- \to Z, Z$.

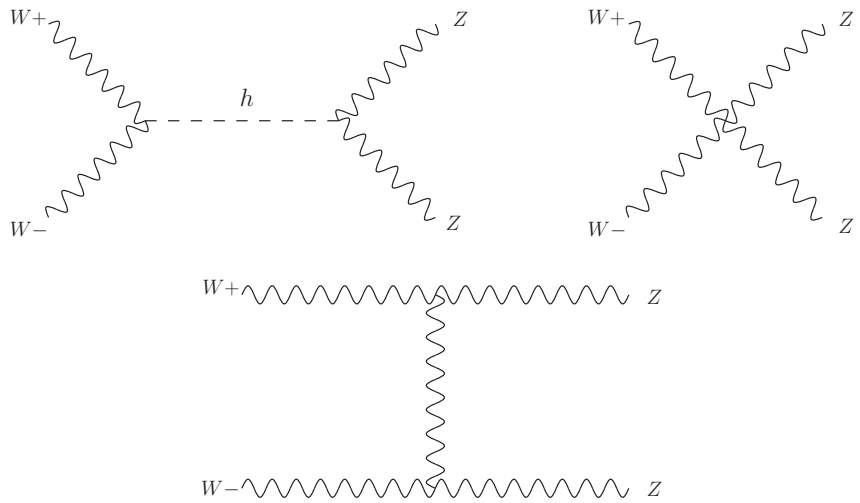

Figure 3.2: *Diagrams contributing to the $W^+, W^- \to Z, Z$ process.*

This simple parton level analysis will enable us to see clearly the properties and relations between the cross section and angles that we will consider without the compli-

cation of a full proton-proton process. The first parameter we consider is an angle, θ_V, which is the angle between an incoming and outgoing vector boson in the rest frame of the scattering. We consider the dependence of the differential cross section on this angle, comparing the standard model to the Higgsless case. It should be remembered that it is the Higgs which provides the cancellation in amplitudes for purely longitudinal vector boson scattering, and that this cancellation means that in the SM the contribution to the overall cross section from pure longitudinal scattering is very small. The Higgsless case on the other hand does not have these cancellations and has a much larger contribution due to longitudinally polarised bosons. As a result, cross sections for the SM Higgs ($a = 1.0$) scenario should be considered to be demonstrating the behaviour of scattering involving transverse bosons, whilst cross sections for the Higgsless scenario will be demonstrating the behaviour of scattering which includes a larger proportion of longitudinally polarised bosons.

In Figure 3.3 we plot the differential cross section for various $VV \to VV$ process with respect to θ_V, at $\sqrt{s} = 1$ TeV. Due to the t- and u-channels corresponding to the exchange of an electroweak (EW) gauge boson (as exemplified in Figure 3.2) or a Higgs boson, the angular distributions are peaked in the forward-backward directions. In the elastic processes on the right, we measured the angle θ_V between the same particle type in the incoming and outgoing set, which is why our plots demonstrate a forward peaking only. The processes described by the left plots on the other hand have symmetric final states, and hence the distributions are symmetric with peaks in the backward direction also. We observe that in the absence of a Higgs boson ($a = 0$) when the contribution from longitudinally polarised bosons is larger, there is both a larger cross section and less pronounced peaking in the forward-backward direction, as shown by the red curves. This provides the first important observation: the forward-backward regions in $VV \to VV$ scattering are mainly related to the transversely polarised gauge bosons, with longitudinally polarised bosons having a much larger differential cross section in the central $-0.4 < \theta_V < 0.4$ region.

This observation immediately gives us one obvious cut which could be useful in increasing the proportion of scattering due to longitudinally polarised bosons, namely any cut which removes the forward-backward contributions in terms of θ_V. The effect

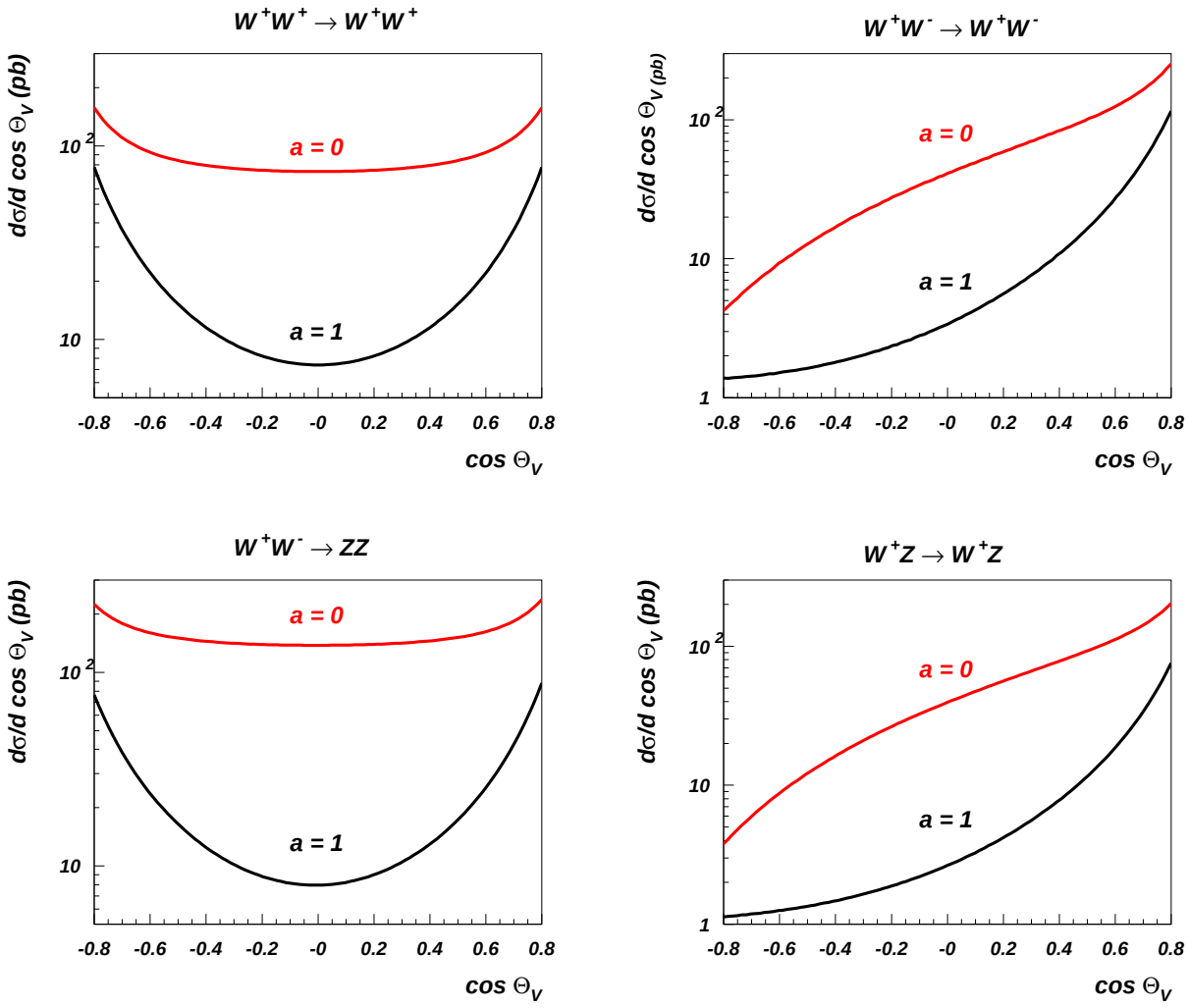

Figure 3.3: $\cos\theta_V$ *angular distributions for* $VV \to VV$ *process for* $\sqrt{s} = 1$ *TeV with (black curves,* $a = 1$*, SM case) and without Higgs boson (red curves,* $a = 0$*).* $\cos\theta_V$ *is the angle between an incoming and outgoing boson in the rest frame of scattering.*

of such a cut is evident in Figure 3.4 where the total cross section for $W^+W^- \to ZZ$ as a function of centre-of-mass energy $\sqrt{s}$ and anomalous coupling a is shown with *no cut* in figure (a) and a cut of $|\theta_V < 0.5|$ applied in figure (b). In both cases we see that for $a \neq 1$ we get the expected increase in cross section due to non-cancellation of amplitudes, which increases with the energy of collision. However when the cut is applied, the increase in cross section is much more acute and larger. At $\sqrt{s} = 2$ TeV, without the cut, the difference in cross section between the SM and Higgsless case is a factor of around 3, whilst adding the cut increases this factor to $\mathcal{O}(10^2)$.

In order to proceed further we decay one of the final state EW bosons and analyse

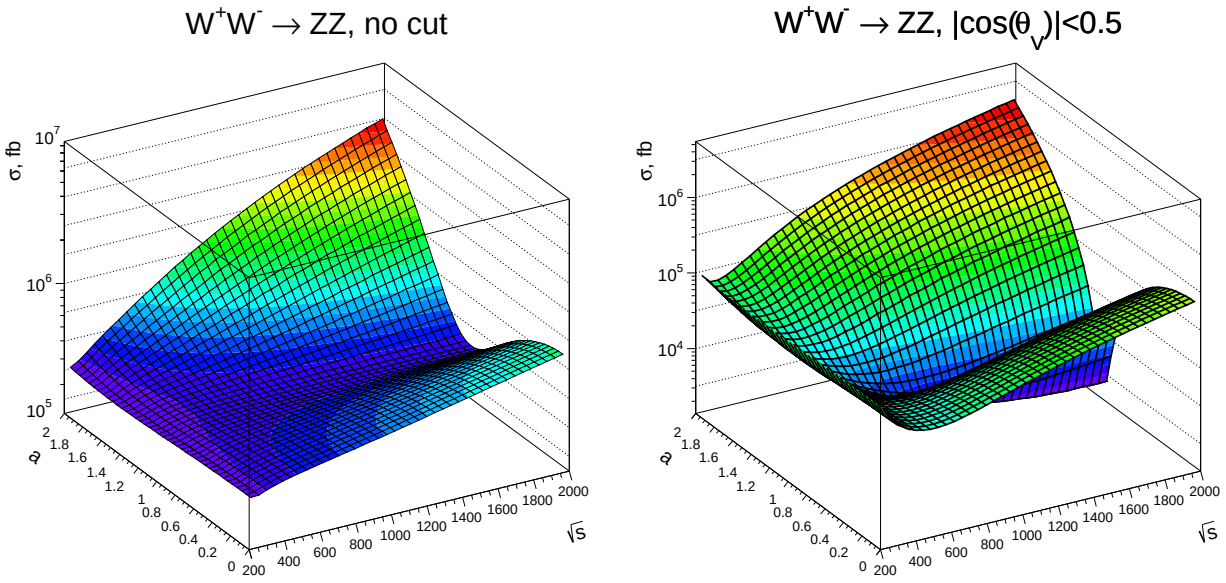

(a) (b)

Figure 3.4: *Total $W^+W^- \to ZZ$ cross section (a) without cuts and (b) with $|\cos(\theta_V)| < 0.5$ as a function of centre-of-mass energy $\sqrt{s}$ and anomalous coupling a.*

the angular distribution in terms of $\cos\theta^*$ as described in section 3.2. This is sensitive to the degree of polarisation of the parent EW gauge boson as described by equations.(3.1–3.3). The results for a number of processes are presented in Figure 3.5.

Firstly, these plots clearly show that for the SM case (black), the shape of distribution is more similar to that in Figure 3.1(b), and hence the polarisation is primarily transverse. For the Higgsless case on the other hand the shape is similar to Figure 3.1(a), showing that in this case the vector bosons have a large longitudinally polarised component. We also compare the cases with a small $|\theta_V| < 0.9$ cut (solid) with a larger $|\theta_V| < 0.5$ cut (dashed), which as expected shows that the stronger cut produces a larger difference between the SM and Higgsless case, as it removes a substantial proportion of the transverse scattering in the Higgsless case. At this point we can note two things about these results. Firstly they provide a further way of removing scattering involving transverse vector bosons, by cutting on θ^* to be in the central region (e.g. $|\theta^*| < 0.5$), which cuts a larger proportion of SM (transverse) than Higgsless (longitudinal) events. Secondly, we see that the differences in distributions can be substantial, and hence θ^* is an important observable to discriminate between events involving longitudinal and transversely polarised gauge bosons.

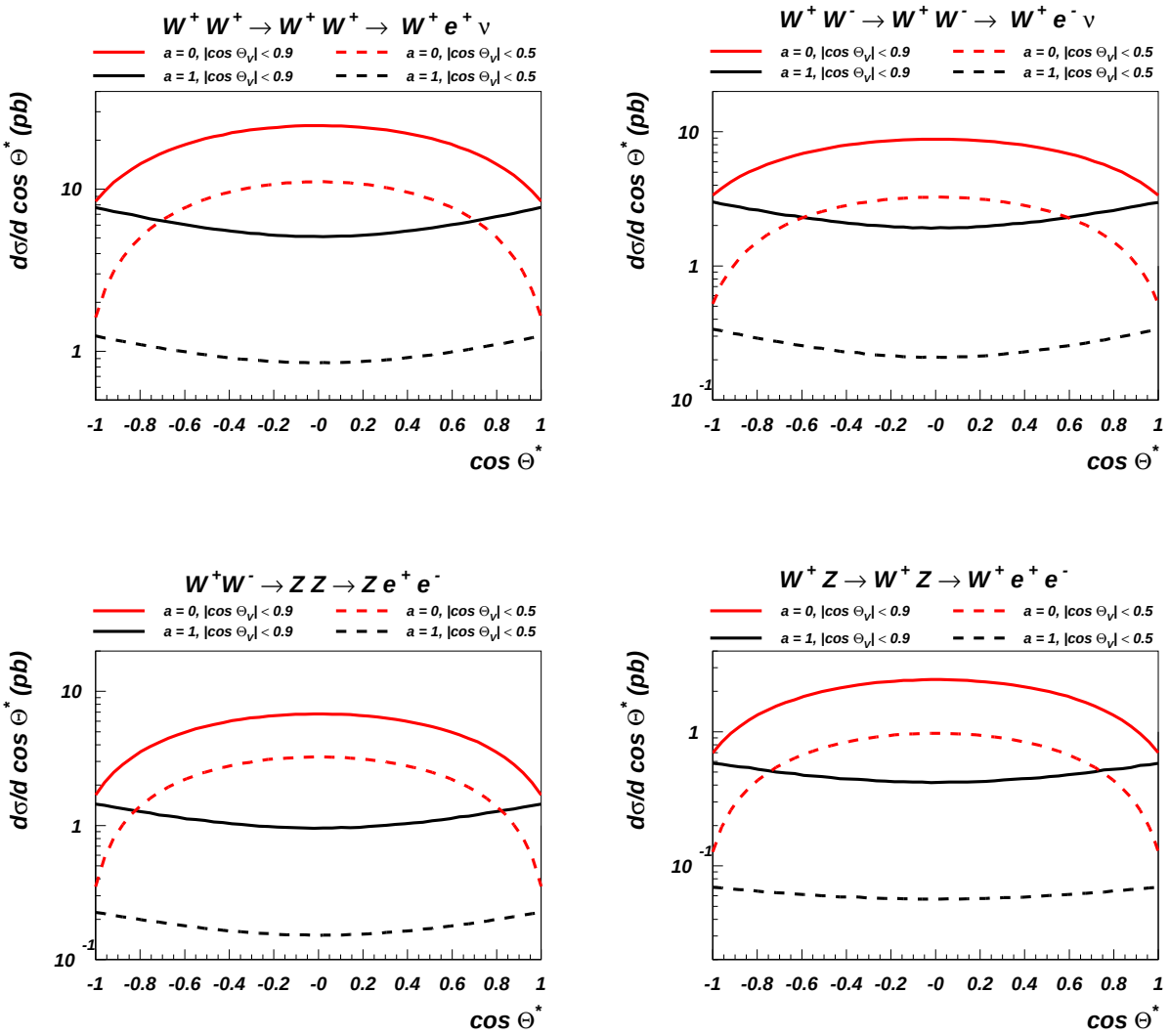

Figure 3.5: $\cos\theta^*$ *angular distributions for* $VV \to VV \to Vll(Vl\nu)$ *process for* $\sqrt{s} = 1$ *TeV with (black curves,* $a = 1$*, SM case) and without Higgs boson (red curves,* $a = 0$*).*

In Figure 3.6 we explicitly show that this is possible, by using Equation 3.3 to recover the degree of polarisation of the parent EW boson.

We see that when $\sqrt{s} = 0.5$ TeV with a cut $|\theta_V| < 0.9$, in the SM 12% of the decaying bosons are longitudinally polarised, whilst in the Higgsless case, 35% are longitudinally polarised. It also confirms that we can enrich this fraction from 35% $\to$ 53% by increasing the cut to $|\cos\theta_V| < 0.5$. Of course this increase is at the expense of reducing the total cross section of events passing the cuts. In (b), we use this fitting to show that the fraction of longitudinally polarised gauge boson increases as expected with centre-of-mass energy, reaching near 100% at 2 TeV in the Higgsless scenario (red).

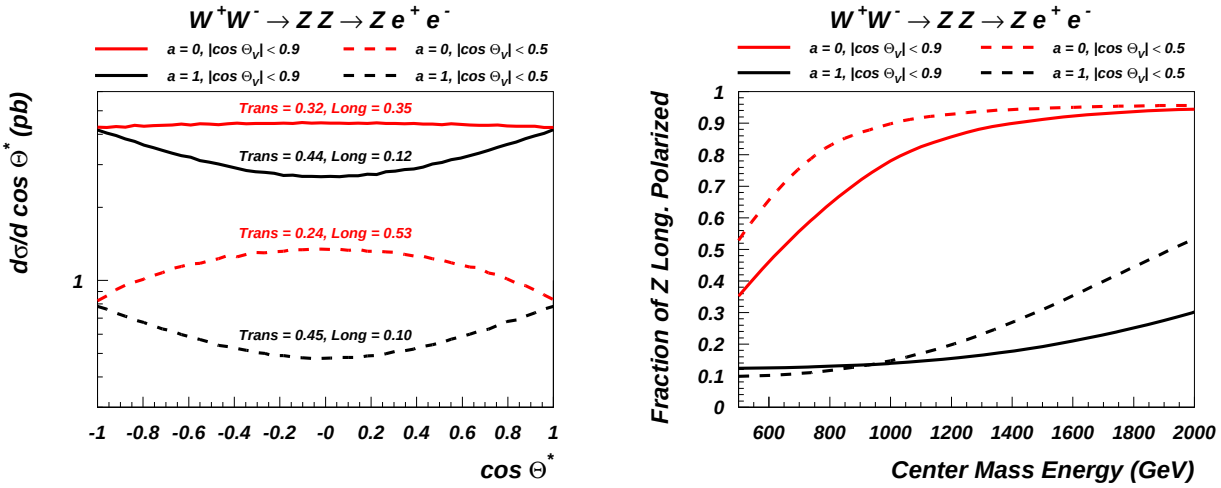

(a) (b)

Figure 3.6: *(a): Fitting parameter results of the Z boson polarisation at* $\sqrt{s} = 0.5$ *TeV. Left and Right polarisations were fitted separately but results were identical to accuracy given in plot. The result displayed is per type of transverse polarisation, i.e. the total transverse polarisation fraction is double the value given. (b): Fraction of the Z bosons which are longitudinal as a function of energy for* $a = 0, 1$ *with* $|\cos\theta_V| < 0.9$ *and* 0.5.

The ability to use $\cos(\theta^*)$ fits to measure the degree of polarisation of decaying gauge bosons, along with the large difference between the standard model and Higgsless scenario raises an interesting possibility: For a fixed centre-of-mass energy, the fraction of polarisation will be related to the anomalous coupling a. Therefore, if for intermediate values of a between 0 and 1 we calculate the expected fraction to be longitudinally polarised, then by measuring this fraction, we are able to directly measure this hVV coupling.

3.5 LHC sensitivity to longitudinal vector boson scattering and Higgs boson couplings to gauge bosons

Thus far, our analysis has been at the parton $VV \to VV$ level, with promising results with regards to cuts to reduce transverse-pollution and fits to directly measure the polarisation of decaying gauge bosons. In this section we investigate how this translates into sensitivity to probe the fraction of longitudinal polarisation in vector boson fusion at the LHC (i.e. in proton-proton collisions), and subsequently the LHC's ability to measure the hVV coupling.

The particular channel analysed in this section is $pp \to jjZZ \to e^+e^-\mu^+\mu^-jj$ ($p = u, \bar{u}, d, \bar{d}$, $j = u, \bar{u}, d, \bar{d}$). This should be representative of all the relevant scattering and decay channels as the angular distributions will be the same for hadronic and leptonic decays, with only a difference in the overall cross section. Of course in an experimental setting there will also be differences in the efficiencies of reconstruction between hadronic and leptonic decays. At the LHC this would probably make it too difficult to analyse fully hadronic decays ($VV \to 4 \times hadron$), but analysis of both fully-leptonic and semi-leptonic ($VV \to 2 \times lepton, 2 \times hadron$), is likely to be possible and would be a topic of a more complete analysis.

We used MadGraph5 [50] for the matrix element calculation and event generation, where we also used VBF cuts to select a larger proportion of diagrams which contain the relevant coupling, as we did in Section 2.7. In this case we used the following kinematic cuts[3]:

$$\begin{aligned} \text{Acceptance cuts:} \quad & p_T^j > 30 \text{ GeV}, \ |\eta_j| < 4.5 \\ & p_T^e > 20 \text{ GeV}, \ |\eta_e| < 2.5 \\ & p_T^\mu > 20 \text{ GeV}, \ |\eta_e| < 2.5 \qquad (3.4) \\ \text{VBF cuts:[56]} \quad & \Delta\eta_{jj} > 4, \ E_j > 300 \text{ GeV} \qquad (3.5) \\ \text{Z boson ID cuts:} \quad & |M_{ee,\mu\mu} - M_Z| \leq 10 \text{ GeV} \qquad (3.6) \end{aligned}$$

For our calculations we used CTEQ6L1 PDF parameterisation and fixed the QCD scale to M_Z.

We were able to calculate the required angles for this process. To find the angle θ_V of vector boson scattering in the VV mass frame, first of all we find the momenta p_1 and p_2 of the initial quarks q_1, q_2 in the $q_1q_2 \to q_3q_4ZZ$ process from a) total invariant mass of the final state particles and b) from the total momentum of the final state particle along the z-axis. Then we find two pairs of the final and initial quarks, say, (q_1, q_3) and (q_2, q_4) with the minimal angle between them in the centre-of-mass frame. This will give us access to the four momentum of each virtual vector boson, p_1^V, p_2^V in the initial state: $p_1^V = q_3 - q_1$ and $p_2^V = q_4 - q_2$ which along with invariant masses of the final state

[3]These are not identical to the VBF cuts used in section 2

particles subsequently allows us to calculate the θ_V angle in the centre-of-mass frame of the $VV \to VV$ scattering. θ^* is easy to calculate from the invariant masses of final state particles.

For the standard model, the cross section for this process was 0.0298 fb, while there was a modest increase to 0.0362 fb when the Higgs boson contribution was removed ($a = 0$). This cross section is quite low since it requires leptonic decays for both Z-bosons, where the decay branching ratio in any leptonic channel is just over 3%. This means that for a given di-Z-boson event, the probability of our specific $ZZ \to e^+e^-\mu^+\mu^-$ decay is only $\sim 0.23\%$. If we allow any semi-leptonic decay of the Z-bosons, the cross section is about 40 times larger. Furthermore, we can estimate that including all of the other relevant $VV \to VV$ channels, namely WW and WZ processes with semi-leptonic decays would lead to an event rate which is around a factor of 250 higher than that for the $pp \to jjZZ \to e^+e^-\mu^+\mu^-jj$ process discussed above. We should keep this in mind when discussing the experimental applicability of our results.

For this $pp \to jjZZ \to e^+e^-\mu^+\mu^-jj$ processes we assume an integrated luminosity of 1.5 ab^{-1}, which is being discussed as one of the high luminosity benchmarks at the future LHC, for which we would have about 50 events from this process for analysis.

Firstly we look at the invariant mass distribution of the ZZ pair. This is calculated from the invariant mass of the 4 leptons in the final state, M_{4l}, and presented in Figure 3.7. The left (right) figure shows the M_{4l} distribution for $|\cos\theta_V| < 0.9(0.5)$ cuts

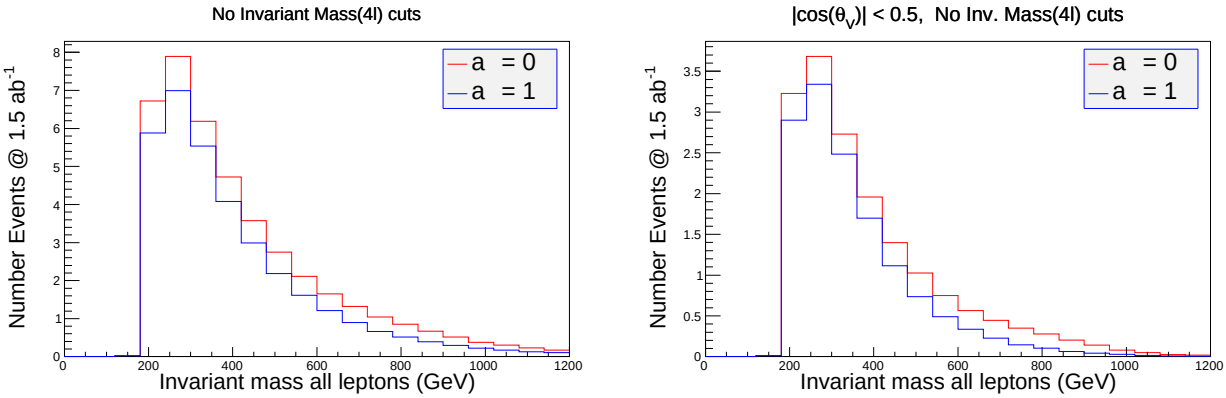

(a) (b)

Figure 3.7: *Four-lepton invariant mass distribution, M_{4l} for 1.5 ab^{-1} @LHC13TEV representing the invariant mass of the vector-boson scattering in $pp \to jjZZ \to e^+e^-\mu^+\mu^-jj$ process: the M_{4l} distribution for (a) $|\cos\theta_V| < 0.9$ cuts, (b) $|\cos\theta_V| < 0.5$ cuts. The red histogram is for $a = 0$, the blue one represents $a = 0$ (SM) case.*

respectively. We can see that as in the $VV \to VV$ analysis, the cross section for the Higgsless (red, $a = 0$) case is larger than for the SM (blue). The effect of increasing the $|\cos\theta_V|$ cut from 0.9 to 0.5 on this distribution is relatively small, and can be observed in that the difference in cross section between $a = 0$ and $a = 1$ becomes greater in the region where M_{4l} is large. This is to be expected as a higher M_{4l} translates to a larger $\sqrt{s}$ of the vector boson collision, with its associated larger cross-sectional increase the Higgsless case.

For the next step we study the ability of a cut on M_{4l} to increase the sensitivity to longitudinal VV scattering and the consequent sensitivity to the hVV coupling. This is analogous to cutting on $\sqrt{s}$ in the $VV \to VV$ scattering, which we know increases the fraction of gauge bosons which are longitudinally polarised as we saw in Figure 3.6. The effect of this cut on the $\cos(\theta_V)$ distribution is visible in Figure 3.8 where we compare (a) no cut on M_{4l}, with (b) a cut $M_{4l} > 500$ GeV applied.

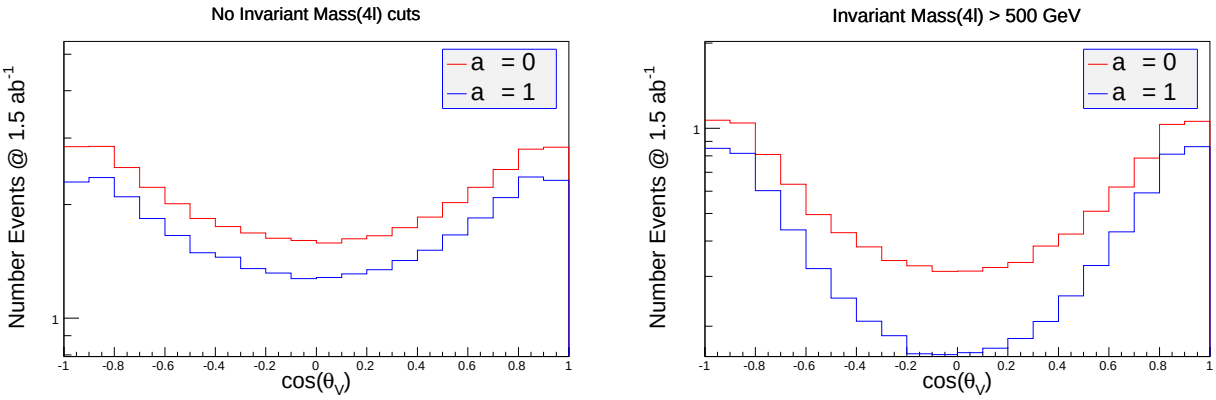

(a) (b)

Figure 3.8: *The $\cos(\theta_V)$ distribution for 1.5 ab^{-1} @LHC13TEV for $pp \to jjZZ \to e^+e^-\mu^+\mu^-jj$ process. (a) no M_{4l} cut applied, (b) the distributions after $M_{4l} > 500$ GeV cut.*

We can see the clear effect of the M_{4l} cut. Without this cut, there is an overall increase in cross section for $a(1 \to 0)$, but the shapes are very similar to each other, representing similar (mainly transverse) polarisation fractions. This is due to the large phase space with M_{4l} relatively low, where the transversely polarised scattering dominates. Following the cut there is a marked difference in shape, with the Higgsless scenario having a much larger cross section in the central region of the distribution. Comparing to Figure 3.3 we see that we now reproduce the results that we found at the $VV \to VV$ level.

Finally, we look at the $\cos(\theta^*)$ distribution whose results are presented in Figure 3.9. For the analysis, we defined $\cos(\theta^*)$ as being between the electron in the

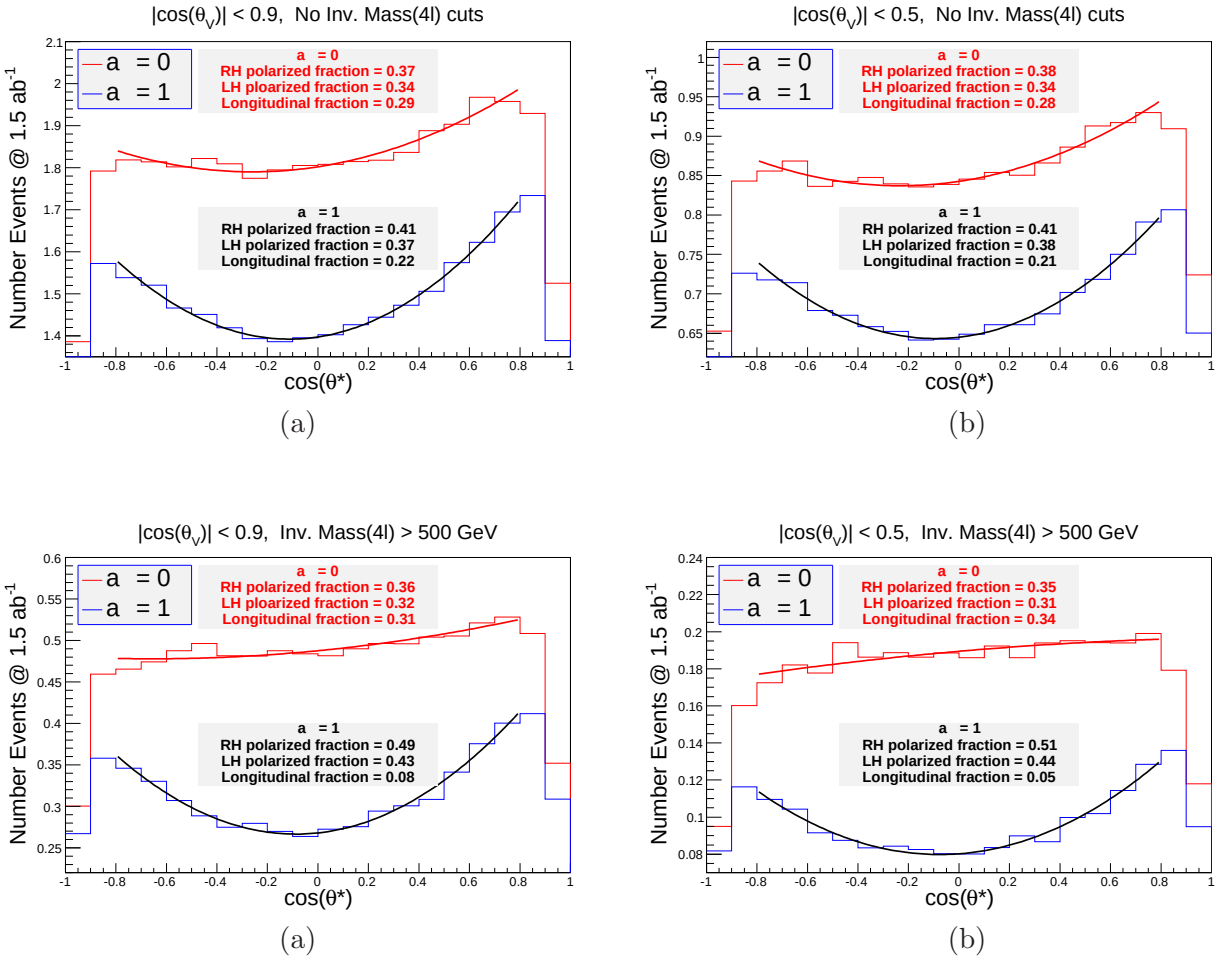

Figure 3.9: *The* $\cos(\theta^*)$ *distribution for* $pp \to jjZZ \to e^+e^-\mu^+\mu^-jj$ *at 1.5* ab^{-1} *@LHC13TEV for four different sets of cuts: (a)* $|\cos(\theta_V)| < 0.9$*; (b)* $|\cos(\theta_V)| < 0.5$*; (c)* $|\cos(\theta_V)| < 0.9$ *and* $M_{4l} > 500$ *GeV (d)* $|\cos(\theta_V)| < 0.5$ *and* $M_{4l} > 500$ *GeV.*

centre-of-mass of the e^+e^- system and the direction of the boost to this system. The ultimate goal here is to be able to measure the fraction of the decaying gauge boson in the $pp \to jjZZ \to e^+e^-\mu^+\mu^-jj$ process which are longitudinally polarised, enabling us to subsequently measure the VVh coupling a. With this in mind, the four frames in Figure 3.9 show $\cos(\theta^*)$ distributions with four different combinations of kinematic cuts, with the aim of increasing the fraction which are longitudinally polarised in the Higgsless case, and enhancing the difference between the $a = 0$ and $a = 1$ scenarios. The cuts are: a) $|\cos(\theta_V)| < 0.9$; b) $|\cos(\theta_V)| < 0.5$; c) $|\cos(\theta_V)| < 0.9$ and $M_{4l} > 500$ GeV; d) $|\cos(\theta_V)| < 0.5$ and $M_{4l} > 500$ GeV. In each case, we fit the $\cos(\theta^*)$ distribution to Equa-

tion. 3.3 using the standard fitting routines of the ROOT data analysis package [71], allowing us to find the fraction of the longitudinal and transverse Z-bosons.

In (a), where there is no cut on M_{4l} and only a small angular cut of $|\cos(\theta_V) < 0.9|$, we see that there is only a small difference in the fraction of gauge bosons which are longitudinally polarised (22% in the SM, 29% for $a = 0$). If we then apply only the cut $|\cos(\theta_V)| < 0.5$ as we do in (b) then this makes little difference to the longitudinal fraction. This is to be expected as we are cutting to select the central region of Figure 3.8(a), where the distribution is similar for the $a = 1$ and $a = 0$ cases. However if we ensure that the energy of $VV \to VV$ scattering is high by applying the cut $M_{4l} > 500$, we produce a large difference between the two scenarios as shown in (c) with longitudinal fractions of 8% and 31% respectively for the SM and Higgsless cases. Finally in (d) we see that if we now apply a $|\cos(\theta_V)| < 0.5$ cut *after* applying this $M_{4l} > 500$ cut on invariant mass, this difference increases even further with the difference in longitudinal fraction of between scenarios of 5% versus 34%. The success of the $|\cos(\theta_V)| < 0.5$ cut can be explained by the fact that the invariant mass cut means that we are selecting the central region of Figure 3.8(b) where it would be expected to increase the longitudinal fraction.

These results seem promising, however for the single process considered, we only have 50 events in total, which leads to large statistical errors on the fitting function and therefore the longitudinal polarisation fraction[4]. Considering purely statistical errors, this is approximately 100% for cut (a), increasing to 300% for cut (d) due to the factor 9 decrease in events passing the cuts. However, these 50 events and consequent errors are for the single $pp \to jjZZ \to e^+e^-\mu^+\mu^-jj$ process considered. A complete analysis would involve the complete set of $VV \to VV$ processes (ZZ, WW, WZ), along with semi-leptonic decay channels, which as previously discussed, would increase the statistics by a factor of around 250. This would decrease the fit statistical error down to around 5% to 10% for for 1.5 ab^{-1} of integrated luminosity for cut (a) and to about 25% for cut (d). The sensitivity to the a parameter would be expected to be similar. Moreover, these results are following a crude trial of different cuts. The optimisation of cuts on

[4]The fits on the plot look like their errors (which are not presented on the plot) would be small, but this is artificial as I produced a large number of events with the total number of events then scaled down according to cross section and luminosity. If I had produced only 50 events, then each bin in the histogram would have to be an integer value, and the large error would be clear.

M_{4l} and $\cos(\theta_V)$, as well as involving the total cross section as another variable to discriminate between different values of a should allow us to improve this accuracy further. It should be noted however that the fully leptonic decay considered here is the most favourable channel, and that including additional channels, either involving hadronic decays or missing energy in the form of neutrinos will be more difficult to reconstruct experimentally, and will be part of the systematic error in an experimental setting. We plan to take this into account in a future study.

3.6 Conclusions

In this chapter we presented our preliminary results of the LHC sensitivity to the hVV couplings via the vector boson fusion process. This method of measuring a is *independent* of the current method from direct Higgs searches. Moreover, this is an important cross-check on this traditional measurement which is model dependent as it is derived from the combined production and decay cross section, where the production includes several different production channels, with the main contribution coming from the loop induced gluon fusion which is very sensitive to new physics in the form of new heavy particles in the loop. Even without new particles this cross section depends on other Higgs couplings, such as htt and hbb. However, for the VBF process which we have studied, only one Higgs couplings, hVV is relevant, allowing a cleaner more model-independent measurement. Furthermore, this measurement is robust against systematic errors since it relies on the *shape* of the $\cos(\theta^*)$ distribution rather than the absolute cross section.

The reason vector boson fusion is able to provide this method to measure the hVV coupling is because the Higgs boson unitarises the $VV \to VV$ amplitudes. This means that any deviation from $a = 1$ leads to a large enhancement in the cross section of longitudinal VV scattering. We have found important correlations between the fraction of vector bosons which are longitudinally polarised and both the scattering angles θ_V and θ^*, as well as a correlation with the invariant mass of the VV system, $M_{VV} = M_{4l}$.

Using a combination of cuts on these observables, we showed that for the process $pp \to jjZZ \to e^+e^-\mu^+\mu^-jj$ which should be representative of all the relevant production and decay channels, we are able to perform a fit of the θ^* distribution. This subsequently allows us to find the fraction of decaying gauge bosons which are longitu-

dinally polarised. In a more complete analysis, where we have calculated the fraction of bosons which would be longitudinally polarised for different intermediate values of a between 0 and 1, this would enable us to measure the hVV coupling. In our current analysis, the statistics would be too low, producing an unacceptably large error on the results, however allowing all $VV \to VV$ channels with both leptonic and semi-leptonic decays would increase our statistics by a factor of around 250. This would allow us to measure the a coupling to between 5% and 25% with 1.5 ab^{-1} depending on which cuts are used, although further study is required to improve the accuracy of these estimations.

Chapter 4

Supersymmetric Higgs

4.1 Overview

As discussed in the introduction, supersymmetry is one of the most popular extensions of the standard model. It's theoretical simplicity and elegance in being the only possible non-trivial extension of the Poincaré group, along with its ability to solve the hierarchy problem, provide promising dark matter candidates, provide a viable mechanism for baryogenesis, and a number of other points as previously discussed mean it is one of the main BSM models which will be searched for at the LHC in run 2.

Analyses of Higgs boson properties reported by ATLAS [72, 73] and CMS [74, 75] are based on 4.7 fb^{-1} at 7 TeV and 13 - 20.7 fb^{-1} at 8 TeV of data (ATLAS) and 5.1 fb^{-1} at 7 TeV and 19.6 fb^{-1} at 8 TeV of data (CMS). The results are presented for various Higgs boson production and decay channels. The production modes include gluon-gluon Fusion (ggF), Vector Boson Fusion (VBF), Higgsstrahlung (VH) and associated production with top-quarks (ttH), while the studied decay modes include $h \to \gamma\gamma$, ZZ, WW, $\tau^+\tau^-$ and $b\bar{b}$[1].

The magnitude of the signal is usually expressed via the "signal strength" parameters μ, defined for either the entire combination of or the individual decay/production modes, relative to the SM. In this study we define individual μ_{XY} for a given production (X) and decay (Y) channel, in terms of production cross sections σ and decays widths Γ (in preference to Branching Ratios (BRs)):

[1]Sensitivity to the $h \to Z\gamma$ mode is much less in comparison, though some limits already exist. Similarly, for Higgs boson invisible decays [76]

$$\mu_{X,Y} = \frac{\sigma_X^{\rm MSSM}}{\sigma_X^{\rm SM}} \times \frac{{\rm BR}_{\rm Y}^{\rm MSSM}}{{\rm BR}_{\rm Y}^{\rm SM}} = \kappa_X \times \frac{\Gamma_Y^{\rm MSSM}/\Gamma_{\rm tot}^{\rm MSSM}}{\Gamma_Y^{\rm SM}/\Gamma_{\rm tot}^{\rm SM}} = \kappa_X \times \frac{\Gamma_Y^{\rm MSSM}}{\Gamma_Y^{\rm SM}} \times \frac{\Gamma_{\rm tot}^{\rm SM}}{\Gamma_{\rm tot}^{\rm MSSM}} = \kappa_X \times \kappa_Y \times \kappa_h^{-1}, \tag{4.1}$$

where, generally, $X = ggF, VBF, VH, ttH$ and $Y = \gamma\gamma$, WW, ZZ, $b\bar{b}$, $\tau\bar{\tau}$, etc. Notice that, in the above equations, κ_X and κ_Y are equal to the respective ratios of the couplings squared while κ_h is the ratio of the total Higgs boson width in the MSSM relative to the SM. For example, for $gg \to h \to \gamma\gamma$, we have

$$\mu_{X,Y} \equiv \mu_{ggF,\gamma\gamma} = \kappa_{ggF} \times \kappa_{\gamma\gamma} \times \kappa_h^{-1} = \frac{\sigma_{ggF^{\rm MSSM}}}{\sigma_{ggF^{\rm SM}}} \times \frac{\Gamma_{h^{\rm MSSM}\gamma\gamma}}{\Gamma_{h^{\rm SM}\gamma\gamma}} \times \kappa_h^{-1}. \tag{4.2}$$

The combination of individual production and decay channels which has been done by experimental papers is a non-trivial procedure which takes into account the efficiency of the various channels determining in turn the corresponding weights in the overall combination.

The results as reported by ATLAS are given by [73]:

$$\mu(h \to \gamma\gamma) = 1.57 \pm 0.3 \tag{4.3}$$

$$\mu(h \to ZZ^{(*)}) = 1.44 \pm 0.4 \tag{4.4}$$

$$\mu(h \to WW^{(*)}) = 1.0 \pm 0.3 \tag{4.5}$$

$$\mu(h \to b\bar{b}) = 0.2 \pm 0.7 \tag{4.6}$$

$$\mu(h \to \tau\bar{\tau}) = 1.4 \pm 0.5. \tag{4.7}$$

where the $h \to b\bar{b}$ value given is for Higgsstrahlung production. For the CMS collaboration they are [74]:

$$\mu(h \to \gamma\gamma) = 0.77 \pm 0.27 \tag{4.8}$$

$$\mu(h \to ZZ) = 0.92 \pm 0.28 \tag{4.9}$$

$$\mu(h \to WW) = 0.68 \pm 0.20 \tag{4.10}$$

$$\mu(h \to b\bar{b}) = 1.15 \pm 0.62 \tag{4.11}$$

$$\mu(h \to \tau\bar{\tau}) = 1.10 \pm 0.41. \tag{4.12}$$

It isn't possible to perform this combination accurately in this phenomenological study as for this we would need to know all the details of various experimental efficiencies for all production and decay channels which are not publicly available. Moreover, the overall signal strength μ most commonly reported combines all production channels to give a single value. This single value can miss signs of new physics since in many BSM scenarios the main production channels ggF and VBF are non-universally altered in comparison to the SM.

Luckily, both experiments have produced results for the $\mu_{X,Y}$ parameters for ggF and VBF separately. These results are in terms of Confidence Levels (CL) for each different decay channel, and are shown in Figure 4.1[72, 74].

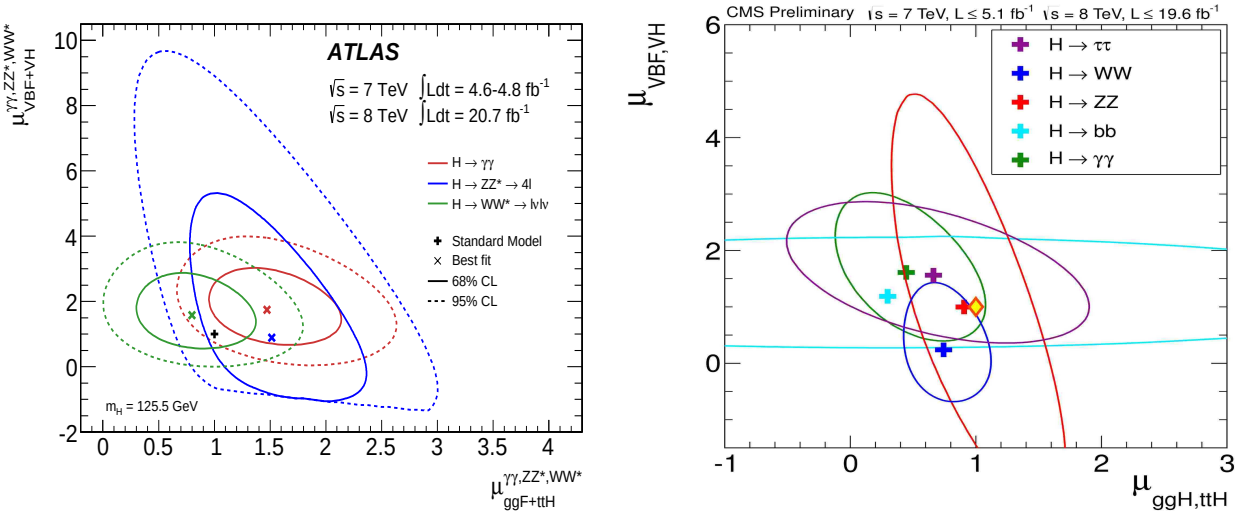

(a) (b)

Figure 4.1: *Likelihood contours and best fit values in the $(\mu_{VBF+VH}, \mu_{ggF+ttH})$ plane for different decay channels observed at the LHC: (a) ATLAS results [72] with 68% (solid lines) and 95% (dashed lines) CL contours and SM expectation (+ symbol); (b) CMS results [74] with 68% (solid line) CL contours and SM expected value ($\diamond$ symbol). (Herein, the label ggH corresponds to our ggF.)*

The first thing to note of these results is that they are indeed consistent with the SM model at 95% CL, which is one of the reasons this newly discovered scalar is called *the* Higgs boson. On the other hand, there is still clearly a lot of room to accommodate deviations from the SM, at least in the $\pm 30\%$ range even at the 68%CL. We also see that for the $h \to \gamma\gamma$ measurement, the ATLAS result is about 2σ above the SM prediction for both ggF and VBF production processes, while the CMS result is approximately 1σ below the SM value for ggF and 1σ above the SM for VBF, respectively. Thus, we also

see that there is currently some tension between the ATLAS and CMS results. From Figure 4.1 we can nonetheless see an interesting general pattern (still within the 1-2σ error interval) that $\mu_{VBF,\gamma\gamma}$ is actually bigger than $\mu_{ggF,\gamma\gamma}$ for both ATLAS and CMS, noting that for the CMS collaboration $\mu_{ggF,\gamma\gamma}$ is essentially below one[2]. This trend has now been quantified by both ATLAS and CMS collaboration, with ATLAS's best fit value being[73]

$$\frac{\mu_{VBF}}{\mu_{ggF+ttH}} = 1.30^{+0.12}_{-0.12}(\text{stat})^{+0.14}_{-0.11}(\text{sys}) \tag{4.13}$$

for a combination of the $\gamma\gamma$, ZZ and WW data, and CMS's best fit value being[75]

$$\frac{\mu_{VBF}}{\mu_{ggF+ttH}} = 1.25^{+0.63}_{-0.45} \tag{4.14}$$

On the basis of this pattern of measured $\mu_{X,Y}$, it is clear that BSM solutions to the LHC data ought to be investigated thoroughly. This is the main motivation for this chapter. In particular, we study the Minimal Supersymmetric Standard Model (MSSM). We assess how supersymmetry effects can affect the Higgs production or decay dynamics (or indeed both), and find the preferred SUSY parameter space in the light of the Higgs LHC data.

In our analysis, we concentrate on the VBF and ggF productions channels only, which are the leading ones, and limit the study of the decay signatures to the cases of $h \to \gamma\gamma, WW, ZZ$ final states, as these are the production and decay modes with the most accurate experimental results. We should also remark that we carried out our investigation using renormalisation-group-improved diagrammatic calculations, including higher-order logarithmic and threshold corrections, using CPsuperH [77, 78] (version 2.3).

Apart from the fact that current data shows a tendency for $\mu_{VBF,YY} > \mu_{ggF,YY}$, the LHC measurements also point to a rather light Higgs mass. As briefly mentioned previously, while the possibility of the Higgs having such a mass is unnatural in the standard model requiring fine tuning, in the MSSM in contrast, the mass of the lightest Higgs boson at tree level has an upper bound of M_Z. Loop effects are able to increase this mass further by up to approximately 45 GeV, and therefore in the MSSM the lightest Higgs with SM-like behaviour is naturally confined to be $\lesssim 135$ GeV [25, 79]. Therefore, in some sense, the Higgs boson mass which is measured at the LHC favours the MSSM (or some other low energy SUSY realisation) over the SM, making it important to test the validity of this SUSY hypothesis against the LHC Higgs data and to establish the viable parameter space.

[2]We should also mention that, initially, both collaborations had initially observed a generic enhancement in the $h \to \gamma\gamma$ channel, however CMS results have since shifted down and even below the SM value.

The MSSM Higgs sector consists of five Higgs bosons: two CP-even neutral bosons, h, H (with masses such that $m_h < m_H$)[3], one CP-odd, A, and a pair of charged Higgs, $H^{\pm}$. At tree level, the Higgs sector can be uniquely defined by just two independent parameters. These can be taken as the mass of any of the five physical Higgs states (hereafter we take M_A) and the ratio between the Vacuum Expectation Values (VEVs) of the two Higgs doublets, denoted by $\tan\beta$. There is a mixing between the two CP-even neutral Higgs bosons parameterised by the mixing angle α, which can be derived using M_A, M_Z and $\tan\beta$. However, we need to consider loop effects, not only for accuracy but also because the hgg and $h\gamma\gamma$ couplings used in our analysis are loop diagrams at lowest order. In this case, we also need to account for the sparticle sector of the MSSM, which in turn implies the introduction of a number of additional parameters.

There has been much previous literature which has explored the Higgs sector in a variety of SUSY scenarios, such as the MSSM [80–99] (also the constrained version [100–106]), Next-to-MSSM[107–114] and (B–L)SSM[115–118], including scenarios with light charginos [119], staus[88, 120] and stops [88].

In this study we re-examine the light stop, sbottom and stau scenarios, but also extend previous research by allowing any combination of MSSM quantum corrections, mixing effects and/or light MSSM fermions entering loops. In particular, we are the first to discuss how the MSSM could explain a non-universal alteration in $\mu_{VBF,YY}$ versus $\mu_{ggF,YY}$ from their SM values such that $\frac{\mu_{VBF}}{\mu_{ggF}} \neq 1$, and use these to examine the compatibility of the MSSM against LHC data. We also examined its ability to produce enhanced (with respect to the SM) rates in the di-photon channel, such that $\mu_{VBF} > 1$ and/or $\mu_{ggF} > 1$.

The plan of this chapter is as follows. In Section. 4.2 we introduce the general setup and the MSSM parameter space that we explore, specific to the Higgs sector. In Section. 4.3 we study the possible generic MSSM effects on the relevant dynamics, namely, on Higgs production, decay and total width. In Sections. 4.3.2 and 4.3.3 we study the effects of stops and sbottoms, respectively, where we find that both can give rise to non-universal alterations in μ_{VBF} versus μ_{ggF} as both particles are able to affect the ggF fusion rate but not the VBF one. Section. 4.3.4 explores the stau contribution, where we find that it can only produce a universal increase in cross section in the di-photon channel, irrespective of the production channel, as it only appears in the $\gamma\gamma$ (and $Z\gamma$) decay loops. In view of the Higgs data potentially indicating a non-universality in the production channels compared to SM predictions, in Section. 4.3.5 we look at the combined effects of these scenarios as well as perform a χ^2 fit of the MSSM parameter space with respect to LHC data. We draw our conclusions in Section. 4.4.

[3]We have deliberately used so far the symbol h to signify both the SM Higgs state and the lightest MSSM CP-even one, as our MSSM solutions to the Higgs data will only involve the latter amongst the possible neutral Higgs states.

4.2 MSSM setup and the parameter space

As discussed in the thesis introduction, the MSSM is essentially a straightforward supersymmetrisation of the SM with the minimal number of new parameters and is the most widely studied potentially realistic SUSY model. Different assumptions about the SUSY breaking dynamics can be made, and these in turn lead to quite different phenomenological predictions and physics at the electroweak scale (EW). The approach used here is to directly study the low energy MSSM without making any assumptions about the high energy physics, by scanning over the relevant SUSY parameters at the EW scale.

The interactions between the Higgs and chiral matter superfields are described by the superpotential, which as discussed in section 1.3.2 is

$$W = Y^E_{ij} L_i E^c_j H_d + Y^D_{ij} Q_i D^c_j H_d + Y^U_{ij} Q_i U^c_j H_u + \mu H_u H_d, \tag{4.15}$$

where Q and U^c contains the $SU(2)$ (s)quark doublets and singlets, L and E^c contain (s)lepton doublets and singlets respectively, and H_u and H_d denote the up-type and down-type Higgs superfields. The soft SUSY breaking terms also previously discussed are categorised as trilinear scalar couplings A^f_{ij}, gaugino masses M_a, sfermion mass-squared terms $\tilde{m}^f_{ij}$, and the bilinear scalar coupling b.

In the MSSM, the SM-like Higgs is either the heaviest CP-even Higgs with all the other Higgs masses ~ 100 GeV[99, 121] or it's the lightest CP-even Higgs, with all other Higgs being heavier. The first scenario with the heavier CP-even Higgs being SM-like is disfavoured by flavor constraints[121]. Therefore we assume that the SM-like Higgs is the lightest CP-even Higgs, which is defined as

$$h = \sin\alpha \ \mathrm{Re}(H^0_d) + \cos\alpha \ \mathrm{Re}(H^0_u),$$

with mixing angle α given by

$$\tan 2\alpha = \tan 2\beta \ \frac{M_A^2 + M_Z^2}{M_A^2 - M_Z^2}. \tag{4.16}$$

As stated previously, the maximum tree level mass of the lightest CP-even Higgs, m_h, is M_Z with loop effects able to increase this further by a maximum of ~ 50 GeV, giving a maximum Higgs mass at one loop of ~ 140 GeV[25]. In order to achieve this, or indeed 125 GeV which is what we require, both the tree level and loop contributions need to be near their maximum. The tree level mass is saturated for $M_A >> M_Z$ and therefore to have the required Higgs mass it becomes essential in our model that we are at or near this limit. This $M_A >> M_Z$ limit is known as the *decoupling limit*, so named as in this scenario it is possible to focus on an effective

low energy theory below the scale of M_A. In this limit, all of the tree level couplings go to their standard model values, which is the reason that the largest cause of deviations from the SM will be loop effects.

At one loop, the mass of the MSSM Higgs can be written as [122–124]

$$m_h^2 \simeq M_Z^2 \cos^2 2\beta + \frac{3}{4\pi^2}\frac{m_t^4}{v^2}\left[\log\left(\frac{M_S^2}{m_t^2}\right) + \frac{X_t^2}{M_S^2}\left(1 - \frac{X_t}{12M_S^2}\right)\right], \tag{4.17}$$

where $M_S^2 = \frac{1}{2}(M_{\tilde{t}_1}^2 + M_{\tilde{t}_2}^2)$ and $X_t = A_t - \mu\cot\beta$. From this expression, it can be easily shown that the maximum value of m_h is obtained at $X_t = \sqrt{6}M_S$, which is known as the "*maximal mixing*" scenario[25]. Also, in order to have $m_h = 125$ GeV, we generally require at least one stop to have a mass of $\mathcal{O}(1)$ TeV so that the logarithmic term is not too small, while the other stop can be light.

In our analysis we are interested in the stop, sbottom and stau states as light particles. The squared mass matrices of these particles in the basis of the gauge eigenstates $(\tilde{f}_L, \tilde{f}_R)$ are

$$M_{\tilde{f}}^2 = \begin{pmatrix} m_f^2 + m_{LL}^2 & m_f X_f \\ m_f X_f & m_f^2 + m_{RR}^2 \end{pmatrix}, \tag{4.18}$$

where

$$m_{LL}^2 = m_{\tilde{f}_L}^2 + (T_{3f} - Q_f s_W^2) M_Z^2 \cos 2\beta, \tag{4.19}$$

$$m_{RR}^2 = m_{\tilde{f}_R}^2 + Q_f s_W^2 M_Z^2 \cos 2\beta, \tag{4.20}$$

$$X_f = A_f - \mu(\tan\beta)^{-2T_{3f}}, \tag{4.21}$$

with T_{3f} the third component of the weak isospin, and Q_f the electric charge. Diagonalising the mass matrices, we find that the sfermion physical masses are given by

$$m_{\tilde{f}_{1,2}}^2 = m_f^2 + \frac{1}{2}\left[m_{LL}^2 + m_{RR}^2 \mp \sqrt{(m_{LL}^2 - m_{RR}^2)^2 + 4m_f^2 X_f^2}\,\right], \tag{4.22}$$

and the mixing angles are given by

$$\tan 2\theta_f = \frac{2m_f X_f}{m_{LL}^2 - m_{RR}^2}. \tag{4.23}$$

Note that the mixing in the stop sector can be large, hence one of the stops, $\tilde{t}_1$, can be very light. Also, with large $\tan\beta$ and $|\mu|$, the mixing in the sbottom and stau sectors can also be strong, leading to light $\tilde{b}_1$ and $\tilde{\tau}_1$.

LHC constraints on SUSY masses are generally quoted as around 600–700 GeV for stops

and sbottoms and in the region of 300 GeV for staus [72, 74], depending on assumptions regarding the decay processes and the masses of decay products. However, these results all rely strongly on a sizeable mass splitting between these sparticles and the Lightest Supersymmetric Sparticle (LSP), a neutralino, to which they decay. These limits are drastically reduced in the region of low mass splittings: *e.g.*, if $m_{\tilde{t}} \approx m_t + m_{\tilde{\chi}^0}$, then the stop signal becomes difficult to distinguish from the $t\bar{t}$ background and the LHC data are unable to constrain the stop mass. A similar situation arises for other mass splitting scenarios, such as when the stop mass is close to the mass of the LSP $m_{\tilde{t}} \approx m_c + m_{\tilde{\chi}^0}$. In this case the stop mass limit is reduced down to the LEP limit $\sim$ 95 GeV [125]. The limits for sbottom and stau masses can also be markedly reduced down to LEP limits ($\sim$ 95 GeV for sbottoms and $\sim$ 85 GeV for staus [125]) for appropriate mass splittings.

In the present study, we performed a large scan of parameter space using CPsuperH to produce the data points, concentrating on those parameters with an important role in the masses and couplings of the stops, sbottoms and staus as well as the mass of the Higgs boson and its couplings to the bottom quark[4]. These masses and couplings are largely independent of the M_1 mass parameter (they vary only $\sim 0.1\%$ for M_1 ranged from 0.1 TeV - 100 TeV). However when $M_1 \ll (M_2, \mu)$, the lightest neutralino mass, $m_{\tilde{\chi}^0_1} \approx M_1$, so that for any point in our parameter scan its values can be chosen to give whichever LSP mass is required to be consistent with cosmological and LHC constraints, without otherwise altering our conclusions. In Tab. 4.1, we list the range of parameters of this scan.

Parameter	Range	Parameter	Range
$\tan\beta$	$[2, 50]$	M_{Q3}	$[0.1, 10]$ TeV
$M_{H^\pm}$	$[0.2, 2]$ TeV	M_{U3}	$[0.1, 5]$ TeV
μ	$[0.1, 5]$ TeV	M_{D3}	$[0.1, 20]$ TeV
A_t	$[0.1, 10]$ TeV	M_{L3}	$[0.1, 5]$ TeV
A_b	$[0.1, 10]$ TeV	M_{E3}	$[0.1, 5]$ TeV
A_τ	$[0.1, 5]$ TeV	M_3	$[0.1, 5]$ TeV
$A_e, A_\mu, A_u, A_d, A_c, A_s$	fixed at 10 GeV	M_2	fixed at 3 TeV

Table 4.1: *Range of scanned parameters. M_1 can be chosen to provide an LSP (neutralino) mass to overcome cosmological and LHC constraints without altering any other relevant results.*

To increase the number of points in the parameter space of interest, three further localised scans were performed, in each case reducing the scanned range of one variable, with the other variable ranges remaining as described in Tab. 4.1. The altered ranges in these additional scans were:

[4]Recall, in fact, that the dominant component of the Higgs boson width for masses of order 125 GeV is typically the partial width in $b\bar{b}$ pairs.

1. 100 GeV $\leq M_{U3} \leq$ 300 GeV to produce light stops;

2. 100 GeV $\leq M_{D3} \leq$ 400 GeV to produce light sbottoms;

3. 100 GeV $\leq M_{E3} \leq$ 400 GeV and 100 GeV $\leq M_{L3} \leq$ 400 GeV to produce light staus.

In order to avoid colour breaking minima of the $\tilde{t}$ or $\tilde{b}$ fields, we apply the constraints[126–128]

$$|A_t|, |\mu| \leq 1.5(M_{Q3} + M_{U3}) \tag{4.24}$$

to all plots and numerical results unless otherwise stated. These requirements are somewhat conservative, in the light of a recent analysis in Ref. [129], yet we maintained them in order to simplify our study.

4.3 MSSM effects in Higgs production and decay

In this section, which is divided into 5 subsections, we discuss MSSM effects which may alter the Higgs event rates at the LHC as compared to those of the SM. Section/ 4.3.1 examines the MSSM effects on Higgs production, decay to di-photons and total width. The remaining four subsections deal with effects of the stop, sbottom, stau and their combined effects, respectively.

4.3.1 The three contexts for MSSM effects

MSSM Higgs production

We start our discussion with MSSM Higgs boson production via the gluon-gluon fusion process, which is the dominant channel for Higgs searches at the LHC. In the SM, this mode is predominantly mediated by top quarks via a one-loop triangle diagram while the contribution from other quarks, even the bottom one, is only at the level of a few percent.

In the MSSM, however, strongly interacting superpartners of the SM quarks, *i.e.*, the squarks, could provide a sizeable contribution to this triangle loop.

The lowest order parton-level cross section can be written as

$$\hat{\sigma}_{\rm LO}(gg \to h) = \frac{\pi^2}{8m_h}\Gamma_{\rm LO}(h \to gg)\Delta(\hat{s} - m_h^2), \tag{4.25}$$

where $\hat{s}$ is the centre-of-mass energy at the partonic level and $\Delta(\hat{s} - m_h^2)$ is the Breit-Wigner form of the Higgs boson propagator, which is given by

$$\Delta(\hat{s} - m_h^2) = \frac{1}{\pi}\frac{\hat{s}\Gamma_h/m_h}{(\hat{s} - m_h^2)^2 + (\hat{s}\Gamma_h/m_h)^2},$$

and Γ_h is the total Higgs boson decay width, while its partial decay width, $\Gamma_{\rm LO}(h \to gg)$, is given by

$$\Gamma_{\rm LO}(h \to gg) = \frac{\alpha_s^2 m_h^3}{512\pi^3}\Big|\sum_f \frac{2Y_f}{m_f} F_{1/2}(x_f) + \sum_S \frac{g_{hSS}}{m_S^2} F_0(x_S)\Big|^2, \tag{4.26}$$

where Y_f and g_{hSS} are the respective MSSM Higgs couplings to the (s)particle species for fermion (spin-1/2) and scalar (spin-0) particles entering the triangle diagram. The loop functions $F_{1/2,0}$ can be found, for example, in [87] and are re-created for convenience in Appendix B. Here, x_i is defined as $4m_i^2/m_h^2$, with m_i being the mass running in the loop. In the decoupling (or quasi-decoupling) regime, as in the SM, the top quark contribution is dominant among the quarks, since it has the largest Yukawa coupling, while the contribution from the other quarks (mainly coming from the bottom quark) is at the percent level. The role of the bottom quark can be dramatically different though in the non-decoupling regime, when the *hbb* Yukawa coupling, $Y_b^{\rm MSSM} = -\frac{m_b}{v}\frac{\sin\alpha}{\cos\beta} = Y_b^{\rm SM}\frac{\sin\alpha}{\cos\beta}$ is enhanced by $\sin\alpha/\cos\beta \simeq \tan\beta$ in comparison to the SM, enabling the bottom quark contribution to the triangle loop to increase and even dominate over the top quark for large values of $\tan\beta$. However, this is not a realistic possibility, since LHC data does not indicate such significant deviations of the Higgs couplings from SM values, while as discussed, data on the Higgs mass measurement indicate that, if the MSSM is realised in nature, then we are in the decoupling or quasi-decoupling regime. In fact, the Higgs boson mass is close to the one reached in the decoupling limit, requiring $\alpha \approx \beta - \frac{\pi}{2}$, hence $Y_b^{\rm MSSM} \approx Y_b^{\rm SM}$ as well as $Y_t^{\rm MSSM} \equiv \frac{m_t}{v}\frac{\cos\alpha}{\sin\beta} \approx Y_t^{\rm SM}$.

From Equation 4.26 one can see that the g_{hSS} coupling has dimension one, while it is more convenient to define a dimensionless $\hat{g}_{hSS}$ to be used hereafter:

$$\hat{g}_{hSS} = \frac{g_{hSS}}{M_W/g} = \frac{g_{hSS}}{(4\sqrt{2}G_F)^{-\frac{1}{2}}} = g_{hSS}\sqrt{4\sqrt{2}G_F}, \tag{4.27}$$

where G_F is the Fermi constant. So $\Gamma_{\rm LO}(h \to gg)$ will have a form

$$\Gamma_{\rm LO}(h \to gg) = \frac{\alpha_s^2 m_h^3}{512\pi^3}\Big|\sum_f \frac{2Y_f}{m_f} F_{1/2}(x_f) + \sum_S \frac{\hat{g}_{hSS}}{m_S^2}\frac{M_W}{g} F_0(x_S)\Big|^2. \tag{4.28}$$

The functions $F_{1/2}(x)$ and $F_0(x)$ reach a plateau very quickly for $x = 4m_i^2/m_h^2 > 1$ and their values are about 1.4 and 0.4, respectively. This fact has important consequences, which we will discuss together with the Higgs decay into two photons, in the next subsection. The specific effects of stop and sbottom loops will be discussed in sections 4.3.2 and 4.3.3.

MSSM Higgs decay into di-photons

In the SM, the one-loop partial decay width of the h state into two photons is given by [130] [131]

$$\begin{aligned}\Gamma(h\to\gamma\gamma) &= \frac{G_F\alpha^2 m_h^3}{128\sqrt{2}\pi^3}\Big|F_1(x_V)+\sum_f N_{c,f}Q_f^2 F_{1/2}(x_f)\Big|^2 \\ &= \frac{\alpha^2 m_h^3}{1024\pi^3}\frac{g^2}{M_W^2}\Big|F_1(x_V)+\sum_f N_{c,f}Q_f^2 F_{1/2}(x_f)\Big|^2 \\ &= \frac{\alpha^2 m_h^3}{1024\pi^3}\Big|\frac{g_{hWW}}{M_W^2}F_1(x_V)+\sum_f \frac{2Y_f}{m_f}N_{c,f}Q_f^2 F_{1/2}(x_f)\Big|^2 \qquad (4.29)\end{aligned}$$

while in the MSSM the one-loop partial decay width of the h state into two photons also gets a contribution from scalar particles, namely sfermions and the charged Higgs boson and is given by

$$\begin{aligned}\Gamma(h\to\gamma\gamma) &= \frac{\alpha^2 m_h^3}{1024\pi^3}\Big|\frac{g_{hWW}}{M_W^2}F_1(x_V)+\sum_f \frac{2Y_f}{m_f}N_{c,f}Q_f^2 F_{1/2}(x_f) \qquad (4.30)\\ &\quad +\sum_S \frac{\hat{g}_{hSS}}{m_S^2}\frac{M_W}{g}N_{c,S}Q_S^2 F_0(x_S)\Big|^2. \qquad (4.31)\end{aligned}$$

Here V, f, and S stand for the Vector, fermion and Scalar particles respectively entering the one-loop triangle diagram, g_{hWW} is the MSSM Higgs coupling to W-boson, and Y_f and $\hat{g}_{hSS}$ are the MSSM couplings of Higgs boson to fermions and scalars defined in the previous subsection.

The SUSY contributions to $\Gamma(h\to\gamma\gamma)$ are mediated by charged Higgs, charginos and charged sfermions. The SM-like part is dominated by W-gauge bosons, for which $F_1(x_W)\simeq -8.3$, whereas the top quark loop is subdominant and enters with opposite sign, $N_{c,f}Q_f^2F_{1/2}(x_f)\simeq 1.8$, with all other fermions contributing negligibly. It is also worth mentioning that as $F_0(x_S)\sim 0.4$, this is about a factor 20 smaller than $F_1(x_W)$ and approximately a factor 4 smaller than $F_{1/2}(x_f)$. Keeping this in mind, if we consider discuss possible sources of enhancement of the $h\to\gamma\gamma$ effective coupling in the MSSM, we see that we have the following possibilities:

1. Via modification of the Yukawa couplings of top and bottom quarks in the loop.
2. Via charged Higgs boson contributions.
3. Via chargino contributions.
4. By the induction of a large scalar contribution, due to the light stop or/and sbottom or/and stau, with negative coupling $\hat{g}_{hSS}$ so that it interferes constructively with the dominant W-contribution.

In the decoupling or quasi-decoupling regimes which we must consider as discussed above,

scenario (1) does not occur. As for case (2), taking into account that the charged Higgs mass is limited to be above 200 GeV (see e.g. [99, 132] and references therein) the fact that its loop contribution is suppressed by a factor of $(M_W/M_{H^\pm})^2$ and that $\hat{g}_{hH^+H^-}$ is of the order of the electroweak coupling (contrary to the $\hat{g}_{hSS}$ coupling for squarks and sleptons which can be large as we discuss below), we have found that the contribution from charged Higgs bosons is generally negligible. In case (3), the chargino contribution can be bigger than that of the charged Higgs, because of the ratio $F_{1/2} : F_0 \simeq 4$ and because the chargino has a lower mass limit of approximately 100 GeV (coming from LEP2 [133]). We have found that the maximum chargino contribution is reached in the $\mu \to M_2, \quad \tan\beta \to 1$ limit (where μ is the Higgs mass parameter while M_2 is the gaugino soft breaking mass) and can enhance the SM $h \to \gamma\gamma$ partial decay width by about 30%. This agrees with the recent results of [119]. This scenario with very light charginos is not the focus of our paper, where we assume charginos to have a mass of at least a few hundred GeVs, and for which the virtual chargino contribution to the $h \to \gamma\gamma$ decay is negligible. Moreover, light charginos could only alter the $h \to \gamma\gamma$ decay, which is qualitatively similar to the effect from the light staus. However the maximum effect of light staus is much larger [120], and is considered in this study in great detail, together with the light sbottom and light stop scenarios. Therefore, in this study we concentrate on scenario (4) in which sizeable MSSM contributions via scalar loops are possible.

It's worth stressing again some important details related to the scalar contribution to $h \to \gamma\gamma$ and $gg \to h$. Firstly, the smallness of the loop function F_0 with respect to both $F_{1/2}$ and F_1, along with the mass suppression factor, $(M_W/M_S)^2$, tend to make scalar loop contributions small. Therefore the only way to have a sizeable effect from scalar loops is to be in a scenario with large coupling $\hat{g}_{hSS}$ and light scalars.

Secondly, the W-boson is the dominant contribution to $h \to \gamma\gamma$, with the top loop amplitude being smaller. However the $gg \to h$ loop obviously doesn't contain a W-boson, and so the leading contribution is smaller and comes from the top (in the SM). This means that when coloured SUSY scalars enter these loops, their relative contribution to the $gg \to h$ loop is larger than for $h \to \gamma\gamma$.

Finally, the amplitude of the loop contribution from the W-boson and top quark have different signs due to their loop factors ($F_1(x_W) \simeq -8.3$, $N_{c,f}Q_f^2 F_{1/2}(x_f) \simeq 1.8$). Therefore, the effect of light coloured squarks is opposite for Higgs production via gluon-gluon fusion compared to di-photon decay: depending on the sign of $\hat{g}_{hSS}$, they will destructively (constructively) interfere with top quarks in production loops and constructively (destructively) interfere with W-boson loops in Higgs boson decays. Therefore, any squark loop which causes an increase (decrease) in $\Gamma(h \to \gamma\gamma)$ will cause a proportionally larger decrease (increase) in $\Gamma(h \to gg)$.

MSSM Higgs total decay width

The total Higgs decay width in the MSSM is given, similarly to the SM, by the sum of all the Higgs partial decay widths, *i.e.*, $\Gamma_{\rm tot} = \Gamma_{b\bar{b}} + \Gamma_{WW} + \Gamma_{ZZ} + \Gamma_{\tau\bar{\tau}}$. Other partial decay widths into SM particles are much smaller and can safely be neglected. As per decays into SUSY states, we assume that the lightest neutralino is heavy enough, so we do not have invisible decay channels with large rates. In the SM with a 125 GeV Higgs mass, these partial decay widths are given by $\Gamma_{b\bar{b}} = 2.4 \times 10^{-3}$ GeV, $\Gamma_{WW} = 8.8 \times 10^{-4}$ GeV, $\Gamma_{ZZ} = 1.0 \times 10^{-4}$ GeV and $\Gamma_{\tau\bar{\tau}} = 2.4 \times 10^{-4}$ GeV.

In the MSSM, when $m_h \approx 125$ GeV, this width is dominated, as in the SM, by the partial width to $b\bar{b}$, $\Gamma(h \to b\bar{b})$, which is controlled by the bottom quark Yukawa coupling, Y_b. In the SM, it is given by the expression $Y_b \equiv g_{hb\bar{b}} = m_b/v$.

At large $\tan\beta$, sbottom-gluino and stop-chargino loops give corrections to this Yukawa, which can be approximated by [134]

$$Y_b \approx -\frac{m_b \sin\alpha}{\cos\beta(1+\Delta m_b)v}\left(1 - \frac{\Delta m_b}{\tan\alpha\tan\beta}\right) \tag{4.32}$$

where

$$\Delta m_b = \frac{2\alpha_3}{3\pi} m_g \mu \tan\beta I(m^2_{\tilde{b}_1}, m^2_{\tilde{b}_2}, |m_{\tilde{g}}|^2) + \frac{|h_t|^2}{16\pi^2} A_t \mu \tan\beta I(m^2_{\tilde{t}_1}, m^2_{\tilde{t}_2}, |\mu|^2) \tag{4.33}$$

and

$$h_t = \frac{m_t}{v\sin\beta} \tag{4.34}$$

with α_3, $m_{\tilde{g}}$ and A_t being the strong coupling constant, gluino mass and top quark trilinear parameter respectively, and where the loop function $I(a,b,c)$ is defined as

$$I(a,b,c) = \frac{ab\ln(a/b) + bc\ln(b/c) + ca\ln(c/a)}{(a-b)(b-c)(a-c)}. \tag{4.35}$$

$I(a,b,c)$ is a positive definite function, therefore with positive m_g, μ and A_t, the correction Δm_b is positive, and Y_b is reduced. In particular, we see that this correction is large for large values of μ.

As the total width of the Higgs is dominated by the partial width to $b\bar{b}$, a reduction in Y_b will lead to a reduction in both $\Gamma(h \to b\bar{b})$ and $\Gamma_{\rm tot}$, with a subsequent universal increase in all other BRs $= \frac{\Gamma^{\rm MSSM}_{\rm partial}}{\Gamma^{\rm MSSM}_{\rm tot}}$ and $\mu_{X,Y} = \kappa_X \times \kappa_Y \times \frac{\Gamma^{\rm SM}_{\rm tot}}{\Gamma^{\rm MSSM}_{\rm tot}}$ irrespective of the production channel.

However, in the decoupling limit ($M_A >> M_Z$), $\tan\alpha \to -\cot\beta$, therefore

$$\left(1 - \frac{\Delta m_b}{\tan\alpha \tan\beta}\right) \to (1 + \Delta m_b) \tag{4.36}$$

which along with $\frac{\sin\alpha}{\cos\beta} \to -1$ means that Y_b reduces to its SM value.

Therefore, to have the possibility of some reduction of Y_b, we also consider the parameter space with values of M_A not too large (the quasi-decoupling regime), such that Y_b can be reduced to be below its SM value. This will need to be balanced by the fact that the values of M_A should be large enough such that $M_h \approx 125$ GeV is possible.

We have analysed one aspect of our scan looking specifically for evidence of this reduction in Y_b. The results of the scan is presented in term of values of $\kappa_{b\bar{b}} = \frac{\Gamma_{bb}^{\rm MSSM}}{\Gamma_{bb}^{\rm SM}}$ in Figure 4.2, where $\kappa_{b\bar{b}} = 1$ is equivalent to having $Y_b^{\rm MSSM} = Y_b^{\rm SM}$ and $\kappa_{b\bar{b}} < 1$ signifies a reduction in Y_b. The lightest Higgs mass was required to be between 124 GeV and 126 GeV for the scan. Different

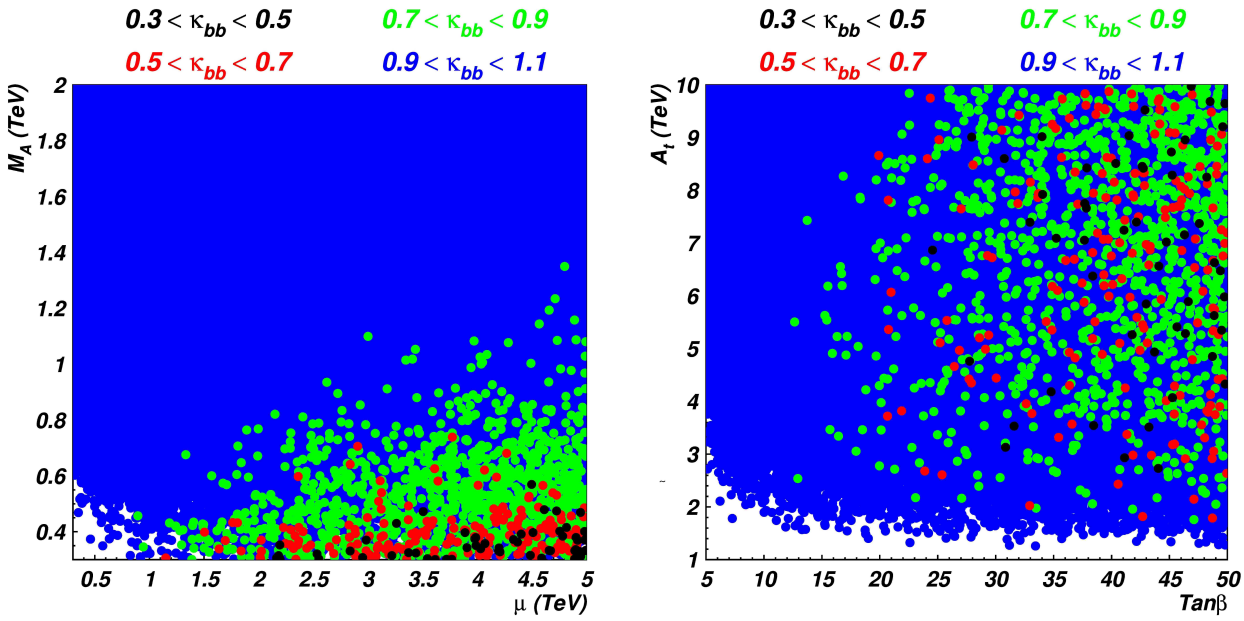

(a) (b)

Figure 4.2: *Results of the scan for $\kappa_{b\bar{b}}$ in the (a) (M_A, μ), and (b) $(A_t, \tan\beta)$ planes respectively, where we have required 124 GeV $\leq m_h \leq$ 126 GeV.*

values of $\kappa_{b\bar{b}}$ are signified by different colours, and are plotted in the (M_A,μ) and ($A_t, \tan\beta$) plane. We can see that large radiative SUSY corrections affecting Y_b are indeed correlated to small values of M_A and large values of μ (Figure 4.2(a)) as well as with large values of $\tan\beta$ (Figure 4.2(b)), as predicted by equations.4.32– 4.33, confirming that this area of parameter space can give rise to large values of Δm_b. Therefore, we confirm that relatively low (down to 300 GeV) values of M_A can lead to an alteration of Y_b, and that even for values of M_A as large

as $\simeq 500$ GeV, a reduction in Y_b such that $\kappa_{bb} < 0.5$ is possible. Only a very weak correlation between A_t and Δm_b is observed in Figure 4.2(b) since we require $M_h = 125 \pm 1$ GeV, and this drives in turn the value of $X_t = A_t - \mu \cot\beta$, and therefore the value of A_t (unless μ is very large with $\tan\beta$ small) to be around $\sqrt{6}M_{\rm SUSY}$, i.e. near the maximal mixing scenario (which is discussed further in the next section). Thus $A_t I(m^2_{\tilde{t}_1}, m^2_{\tilde{t}_2}, |\mu|^2) \approx \sqrt{6}M_{\rm SUSY} I(m^2_{\tilde{t}_1}, m^2_{\tilde{t}_2}, |\mu|^2)$ which can be shown to decrease for large $M_{\rm SUSY}$, limiting its maximum contribution to Δm_b.

4.3.2 Stop quark effects

As previously discussed, since $\frac{F_1}{F_0} \approx -20$, in order for stops to have a significant effect on $(h \to \gamma\gamma)$, $\hat{g}_{h\tilde{t}_1\tilde{t}_1}$ is required to be very large. Furthermore, a positive $\hat{g}_{h\tilde{t}_1\tilde{t}_1}$ coupling will decrease $\kappa_{\gamma\gamma}$ whilst a negative coupling will increase $\kappa_{\gamma\gamma}$.

In the decoupling limit, the Higgs coupling to the lightest stop is given by [25]

$$\hat{g}_{h\tilde{t}_1\tilde{t}_1} = \frac{1}{2}\cos 2\beta\Big[\cos^2\theta_{\tilde{t}} - \frac{4}{3}\sin^2\theta_W \cos 2\theta_{\tilde{t}}\Big] + \frac{m_t^2}{M_Z^2} + \frac{1}{2}\sin 2\theta_{\tilde{t}}\frac{m_t X_t}{M_Z^2}, \tag{4.37}$$

where $\theta_{\tilde{t}}$ is the stop mixing angle defined by

$$\sin 2\theta_t = \frac{2m_t X_t}{m^2_{\tilde{t}_1} - m^2_{\tilde{t}_2}} \tag{4.38}$$

and X_t is given in terms of the the Higgs-stop trilinear coupling as $X_t = A_t - \mu\cot\beta$.

The first term in the equation is small compared to $\frac{m_t^2}{M_Z^2}$ and so can be largely ignored. When X_t is also small, then $\hat{g}_{h\tilde{t}_1\tilde{t}_1} \simeq \frac{m_t^2}{M_Z^2} > 0$ will lead to a decrease of $k_{\gamma\gamma}$. For large X_t, if $m_{\tilde{t}_1} < m_{\tilde{t}_2}$, it can be shown that $\sin 2\theta_{\tilde{t}} \simeq -1$ and therefore the Higgs coupling to the lightest stop is strongly enhanced and negative. However, since $m_h \approx 125$ GeV, the scenario with light stops requires that the Higgs should be near the maximal mixing scenario, *i.e.*, $X_t \approx \sqrt{6}M_{\rm SUSY}$, where $M_{\rm SUSY} = \frac{1}{2}(m_{\tilde{t}_1} + m_{\tilde{t}_2})$. Hence, we are not free to consider very large values of X_t as an independent parameter. In this case, one has

$$\hat{g}_{h\tilde{t}_1\tilde{t}_1} \sim \frac{m_t^2}{M_Z^2} + \frac{3}{2}\frac{m_t^2}{M_Z^2}\frac{(m_{\tilde{t}_1} + m_{\tilde{t}_2})^2}{(m^2_{\tilde{t}_1} - m^2_{\tilde{t}_2})}. \tag{4.39}$$

Thus, if $m^2_{\tilde{t}_2} \approx m^2_{\tilde{t}_1}$, it is possible to get a very large Higgs coupling to stops. However, with a light stop, such that $m^2_{\tilde{t}_1} \ll m^2_{\tilde{t}_2}$, one finds

$$\hat{g}_{h\tilde{t}_1\tilde{t}_1} \to \frac{m_t^2}{M_Z^2} - \frac{3}{2}\frac{m_t^2}{M_Z^2} = -\frac{1}{2}\frac{m_t^2}{M_Z^2}. \tag{4.40}$$

Therefore $\hat{g}_{h\tilde{t}_1\tilde{t}_1}$ is both negative (making the overall stop loop contribution of the same sign as

the W loop), thereby increasing $k_{\gamma\gamma}$, and fixed, which limits the overall contribution to $(h \to \gamma\gamma)$ of a stop loop of a particular mass. Small deviations from this prediction should be expected as in practice we only require *near* maximal mixing.

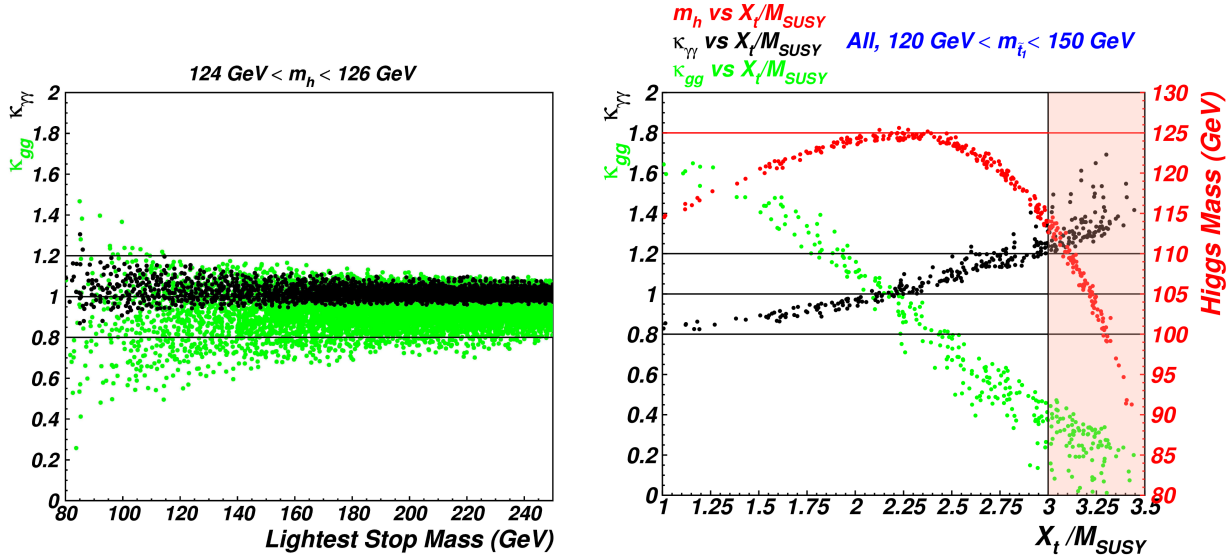

(a) (b)

Figure 4.3: *Left: $\kappa_{\gamma\gamma}$ (black) and κ_{gg} (green) as a function of lightest stop mass for 124 GeV $< m_h <$ 126 GeV. (b) $\kappa_{\gamma\gamma}$ (black), κ_{gg} (green) and m_h (red) as functions of $\frac{X_t}{M_{\rm SUSY}}$ for 120 GeV $\leq m_{\tilde{t}_1} \leq$ 150 GeV. Cuts have been applied such that only points with a Higgs mass within 2 GeV of the maximum value for each value of $\frac{X_t}{M_{\rm SUSY}}$ are kept. The pink-shaded window indicates the $X_t/M_{\rm SUSY} > 3$ region, where the majority of points do not pass the colour breaking minima conditions. To isolate the influence of light stops, the following cuts are also applied to both plots: $m_{H^\pm}$, $m_{\chi^\pm_{1,2}}$, $m_{\tilde{\tau}_{1,2}}$, $m_{\tilde{b}_{1,2}}$, $m_{\tilde{t}_2} > 300$ GeV.*

Figure 4.3(b), where the values of $\kappa_{\gamma\gamma}$ (black), κ_{gg} (green) and m_h (red) versus $X_t/M_{\rm SUSY}$ are plotted for the scan described in section 4.2 provides a clear visual illustration of the algebraic argument discussed above in equations 4.37 to 4.40 as to why the Higgs-stop coupling, $\hat{g}_{h\tilde{t}_1\tilde{t}_1}$, is relatively fixed. We see clearly that there is only a narrow range of values of $X_t/M_{\rm SUSY}$ (near the maximal mixing value[5] of $\sqrt{6} \approx 2.4$) for which the Higgs mass $\sim$ 125 GeV. However as $\hat{g}_{h\tilde{t}_1\tilde{t}_1}$ also depends on X_t, this fixes the value of $\kappa_{\gamma\gamma}$ (and also κ_{gg}) to a narrow range of around $0.9 \lesssim k_{\gamma\gamma} \lesssim 1.2$. In brief, the requirement for a 125 GeV Higgs, near the maximum possible in the MSSM, narrows the available parameter space and leads to a correlation between $\hat{g}_{h\tilde{t}_1\tilde{t}_1}$ and the Higgs mass. In Figure 4.3(a) we show results for $\kappa_{\gamma\gamma}$ (black) and κ_{gg} (green) as a function of the lightest stop mass, $m_{\tilde{t}_1}$, where we have required 124 GeV $< m_h <$ 126 GeV. We see that even if the stop is as light as $m_{\tilde{t}_1} \sim$ 120 GeV, the maximum possible increase would give us $\kappa_{\gamma\gamma} \approx 1.2$. However due to the lack of W-boson in the loop for $gg \to h$, the stop effect here

[5]The maximum value of m_h displayed in Figure 4.3(b) occurs for $X_t/M_{\rm SUSY}$ slightly smaller than $\sqrt{6}$ as it is calculated at two loops, where the maximal mixing value is slightly smaller and closer to 2.

is larger, giving a minimum $\kappa_{gg} \sim 0.6$ for $m_{\tilde{t}_1} \sim 120$, despite the same correlation in coupling. Looking again at Figure 4.3(b), it's worth noting that the effects of light stops on $\kappa_{\gamma\gamma}$ and κ_{gg} could be much larger if this correlation between m_h and $\hat{g}_{h\tilde{t}_1\tilde{t}_1}$ didn't occur such that X_t could be larger, only being limited to $X_t/M_{\rm SUSY} < 3$ by the colour breaking minima conditions discussed in section 4.2 (red shaded region). In this case, for $m_{\tilde{t}_1} \sim 120$, $\kappa_{\gamma\gamma}$ could be as large as ~ 1.5, and κ_{gg} as small as 0.1. This is relevant as for sbottoms such a correlation between its Higgs coupling and the Higgs mass does not occur, as will be discussed in section 4.3.3.

Let us consider the overall effect of light stops on $\mu_{ggF,\gamma\gamma} = k_{gg} \times k_{\gamma\gamma} \times k_h^{-1}$ via its effects on $k_{\gamma\gamma}$ and k_{gg} in the parameter space where the total width is close to the SM one. From Figure 4.3 (b) we would expect that, in general, either $k_{\gamma\gamma}$ is increased with a relatively larger decrease in k_{gg}, causing an overall decrease in $\mu_{ggF,\gamma\gamma}$, or $k_{\gamma\gamma}$ is decreased with a relatively larger increase in k_{gg}, causing an overall increase in $\mu_{ggF,\gamma\gamma}$. This is demonstrated in Figure 4.4(a), where we see that (other than for a few points very near $\mu_{ggF,\gamma\gamma} = 1$ where other factors such as small changes in the total width play a role) we have $\mu_{ggF,\gamma\gamma} > 1$ when $k_{gg} > 1$ (red) and vice versa (black). This means that if the total width of the Higgs boson is unchanged, then stop loops alone can produce a universal increase in all decay channels ($\mu_{ggF,Y} > 1$) via increasing the ggF production channel, but will not produce an isolated increase in $(h \to \gamma\gamma)$, as this will always be cancelled by a relatively larger decrease in ggF production.

We are naturally lead to consider the possibility of counteracting the effect of a reduced κ_{gg} caused by light stops by reducing $\Gamma_{b\bar{b}}$ as discussed in section 4.3.1. This would mean that when the stop coupling is negative, producing an increase in $k_{\gamma\gamma}$ and bigger relative decrease of κ_{gg}, the reduction in $\Gamma_{b\bar{b}}$ causes an in crease in the BRs of all channels other than $b\bar{b}$, such that the overall value for $\mu_{ggF,Y}$ remains ≈ 1. In this scenario, $\mu_{VBF,\gamma\gamma} > \mu_{ggF,\gamma\gamma}$ as the VBF channel will be increased by both $k_{\gamma\gamma} > 1$ and the increased BR to photons from the reduced total width, without the reduced production rate of the loop induced ggF channel. This is demonstrated in Figure 4.4 (b) where the effects of light stops and reduced $\Gamma_{b\bar{b}}$ (via a reduction in the bottom Yukawa coupling) are combined together, and the resulting $\mu_{VBF,\gamma\gamma}$ and $\mu_{ggF,\gamma\gamma}$ values along with current best fit CMS and ATLAS data are plotted. We can see in Figure 4.4 (b)(i) that the smaller the κ_{bb} values, the larger the *universal* $\mu_{VBF,\gamma\gamma}$ and $\mu_{ggF,\gamma\gamma}$ increases it will cause. Figure 4.4 (b)(ii) demonstrates how decreasing stop quark masses lead to an increase of the *non-universal* alteration of these couplings as we would expect, although over the squark masses considered this correlation is fairly weak, which is explained by observing that in Figure 4.3 the lowest possible values of κ_{gg} only varies relatively slowly for 150 GeV $< m_{\tilde{t}_1} <$ 300 GeV requiring $m_{\tilde{t}_1} \lesssim$ 140 GeV before a significant decrease with decreasing mass occurs. By comparing Figure 4.4(b)(i) and (ii) we see that the lightest stops, with masses 120 GeV

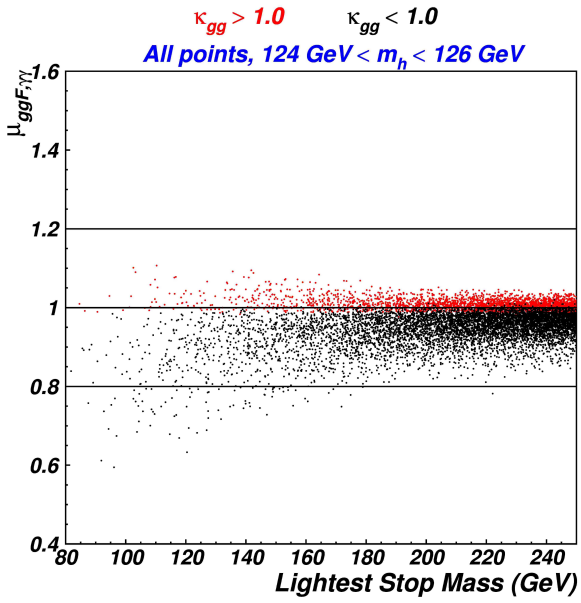

(a)

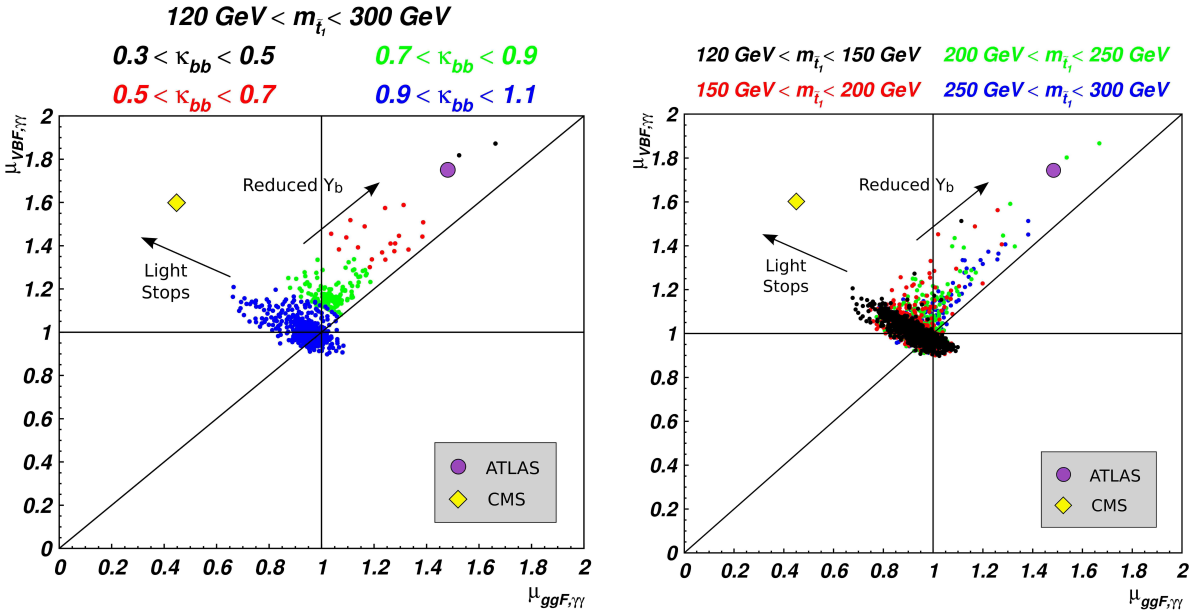

(b)(i) (b)(ii)

Figure 4.4: *(a) $\mu_{ggF,\gamma\gamma}$ vs lightest stop mass for $\kappa_{gg} > 1$ (red) and $\kappa_{gg} \leq 1$ (black). We have cut for $0.98 \leq \kappa_{bb} \leq 1.02$ to remove the possible effect of a reduced $\Gamma_{hb\bar{b}}$. (b) Each point of the scan with 120 GeV $\leq m_{\tilde{t}_1} \leq$ 300 GeV is plotted on the (μ_{VBF}, μ_{ggF}) plane, with colours to indicate (i) different values for κ_{bb}, (ii) different $m_{\tilde{t}_1}$ masses. The results from ATLAS (purple circle) and CMS (yellow diamond) are indicated for comparison. For their 95% CL contours, see Figure 4.10. (They are removed here for clarity). In all the plots, 124 GeV $\leq m_h \leq$ 126 GeV, and to isolate the influence of light stops the following cuts are also applied: $m_{H^\pm}$, $m_{\chi^\pm_{1,2}}$, $m_{\tilde{\tau}_{1,2}}$, $m_{\tilde{b}_{1,2}}$, $m_{\tilde{t}_2} >$ 300 GeV.*

$< m_{\tilde{t}_1} < 150$ GeV, rarely have $\kappa_{bb} < 0.9$, which occurs because in the area of parameter space with very light stops, the Higgs mass is lower due to logarithmic terms in loop corrections, and so we are forced from the quasi-decoupling to the decoupling regime in order to increase the tree level component of the mass enough to have $m_h \sim 125$ GeV.

In this light stop, reduced $\Gamma_{b\bar{b}}$ scenario, the same non-universal situation, (i.e. $\mu_{VBF,WW/ZZ/\tau\tau/\gamma\gamma/bb} > \mu_{ggF,WW/ZZ/\tau\tau/\gamma\gamma/bb}$), takes place for all other decay channels, as will be discussed further in section 4.3.5, while the light stop in the decay loop means that the di-photon decay channel can be increased up to a factor of up to 1.2 relative to the other decays.

Of note, as briefly mentioned above, the area of parameter space with light stops and a Higgs mass of ~ 125 GeV is relatively small, because a heavy $M_{\rm SUSY}$ is preferred to give large logarithmic parts to the radiative corrections to the Higgs Mass. The scenario where $M_{U3} \sim M_{Q3} \gtrsim 300$ GeV requires fine-tuning of the stop mixing parameter X_t in order to achieve a lightest stop with mass ≤ 300 GeV. However, as X_t is fixed by the near maximal mixing requirement ($X_t \approx \sqrt{6} M_{\rm SUSY}$), this is not possible. Hence, the area of parameter space with $m_h \sim 125$ GeV and light stops (with mass ≤ 300 GeV) is where $M_{U3} \ll M_{Q3}$, generally with $M_{U3} \leq 300$ GeV and $M_{Q3} \gtrsim 2$ TeV. In this region it is easy to show that $m_{\tilde{t_1}} \approx M_{U3}$ and $m_{\tilde{t_2}} \approx M_{Q3}$. This explains the reason for choosing the reduced range of M_{U3} described in section 4.2 for the additional scan. The relationship between M_{U3}, M_{Q3} and the lightest stop mass is shown in Figure 4.5, where we have required 124 GeV $\leq m_h \leq$ 126 GeV. It clearly demonstrates a strong correlation between $m_{\tilde{t_1}}$ and M_{U3} when $M_{U3} \ll M_{Q3}$ as discussed. In Tab. 4.2, we give three different benchmark points for scenarios where light stops give rise to $\frac{\mu_{VBF}}{\mu_{ggF}} > 1$, where we have also included a value for the minimum fine-tuning for each of the benchmark points.

Our fine-tuning parameter is based on the electroweak fine-tuning parameter[135–137]. This value is derived by noting that the minimisation condition for the Higgs potential gives rise to the equation for the Z-boson mass,

$$\frac{M_Z^2}{2} = \frac{m_{H_d}^2 + \Sigma_d^d - \left(m_{H_u}^2 + \Sigma_u^u\right) \tan^2\beta}{\tan^2\beta - 1} - \mu^2 \tag{4.41}$$

where Σ_u^u and Σ_d^d are the radiative corrections to $m_{H_u}^2$ and $m_{H_d}^2$. The electroweak fine-tuning parameter is then defined as

$$\Delta_{EW} \equiv max_i(C_i)/(M_Z^2/2) \tag{4.42}$$

where $C_{H_u} = |-m_{H_u}^2 \frac{\tan^2\beta}{(\tan^2\beta - 1)}|$ is defined from the coefficient of $m_{H_u}^2$ in Equation 4.41, with

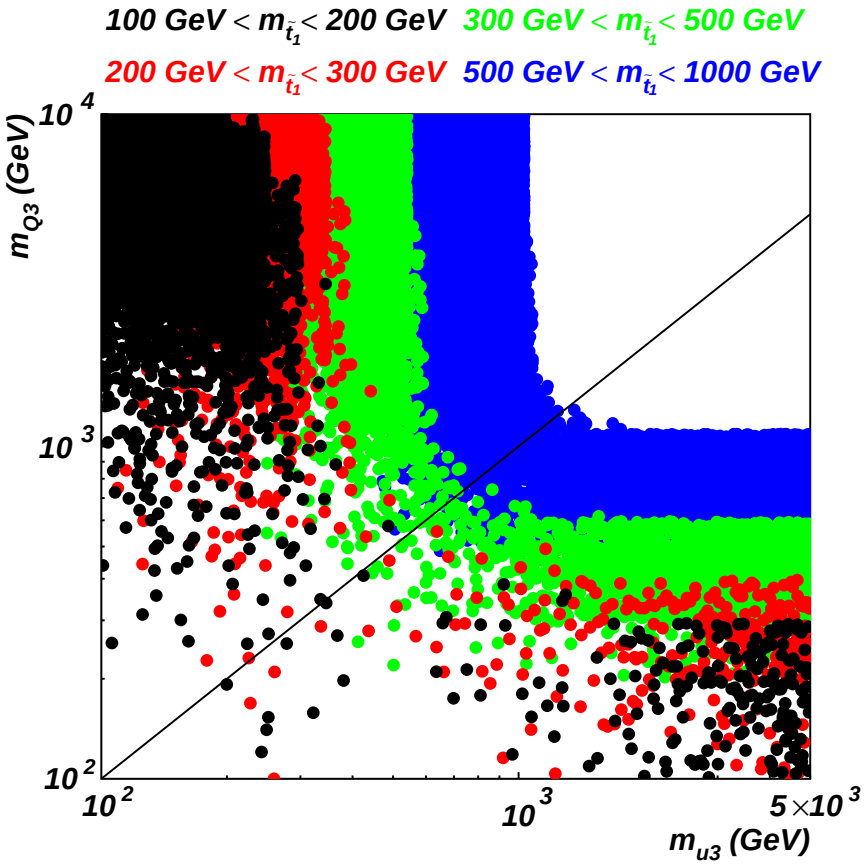

Figure 4.5: *Different values for $m_{\tilde{t}_1}$ in the M_{U3} versus M_{Q3} plane. We have required* 124 *GeV* $\leq m_h \leq$ 126 *GeV.*

analogous definitions for C_{H_d}, C_μ, $C_{\Sigma_u^u}$ and $C_{\Sigma_d^d}$. If $\tan\beta$ is moderate or large, we have

$$\frac{M_Z^2}{2} \approx -\left(m_{H_u}^2 + \Sigma_u^u\right) - \mu^2. \tag{4.43}$$

Σ_u^u is defined with regard to the derivatives of the radiative corrections to the Higgs potential, but as our starting point is the theory at the EW scale (rather than the GUT scale) it is not defined in our case. Therefore the measure of fine-tuning,

$$\Delta \equiv |\mu^2|/(M_Z^2/2) \tag{4.44}$$

gives a minimum value for Δ_{EW}. It should be stressed that this is a *minimum* value, which could be larger if there is a large cancellation between $m_{H_u}^2$ and Σ_u^u as discussed by Baer et. al. in [137], especially in view of the large M_{D3} of $\mathcal{O}(10$ TeV) used for our benchmark points. Keeping this in mind we will be using this definition of fine-tuning in this chapter.

We see that for Benchmark points 1 and 3, $\Delta^{-1} \sim 2 - 5\%$, as $k_{bb} \sim 1$ so there is no

Parameter	Benchmark 1	Benchmark 2	Benchmark 3
$\tan\beta$	37	48	44
μ	300 GeV	2 TeV	400 GeV
$M_{H^\pm}$	1.7 TeV	1 TeV	750 GeV
M_{Q3}	2.5 TeV	2.5 TeV	1.3 TeV
M_{U3}	165 GeV	230 GeV	320 GeV
M_{D3}	11 TeV	12 TeV	7 TeV
M_{L3}	4 TeV	3 TeV	2 TeV
M_{E3}	1.2 TeV	500 GeV	5 TeV
M_3	1.9 TeV	3.2 TeV	2 TeV
M_2	3 TeV	3 TeV	3 TeV
M_1	125 GeV	172 GeV	250 GeV
A_t	3.1 TeV	3.6 TeV	2.1 TeV
A_b	5.5 TeV	100 GeV	7 TeV
A_τ	500 GeV	0 GeV	2.5 TeV
$m_{\tilde{t}_1}$	125 GeV	177 GeV	254 GeV
$m_{\tilde{\chi}_1^0}$	121 GeV	172 GeV	245 GeV
m_h	124.1 GeV	124.0 GeV	124.2 GeV
$\frac{\mu_{VBF,\gamma\gamma}}{\mu_{ggF,\gamma\gamma}}$	$\frac{1.11}{0.78} = 1.42$	$\frac{1.65}{1.16} = 1.42$	$\frac{1.08}{0.80} = 1.35$
κ_{gg}	0.71	0.70	0.74
$\kappa_{\gamma\gamma}$	1.10	1.10	1.08
κ_{bb}	1.01	0.55	1.04
κ_h	0.99	0.67	1.01
$\mu_{ggF,bb}$	0.72	0.58	0.76
Δ^{-1}	4.6%	0.1%	2.6%

Table 4.2: *Benchmark points with light stops and* $\frac{\mu_{VBF}}{\mu_{ggF}} > 1$

requirement for a large μ. However Benchmark 2 has a reduced k_{bb} which requires a large Δm_b and hence a large μ, leading to a larger minimum fine-tuning, with $\Delta^{-1} \sim 0.1\%$.

We should also mention here that the light stop scenario has been discussed in connection to Electroweak Baryogenesis [138, 139], a scenario where light stops allows a strong first order phase transition in the early universe, which is able to explain the high matter/antimatter ratio we observe in the universe today. This requires that $A_t \lesssim M_{Q3}/2$ (or $X_t/M_{\rm SUSY} \lesssim \frac{1}{\sqrt{2}}$) in order to achieve a strong phase transition, and therefore electroweak baryogenesis is not realised in the maximal mixing scenario which we consider in our paper. For these lower values of $X_t/M_{\rm SUSY}$, the 125 GeV Higgs mass can only be achieved for extremely large values of $M_{Q3} \simeq 10^6$ TeV [139], and we also find that $\hat{g}_{h\tilde{t}_1\tilde{t}_1} > 0$, leading to a constructive interference of the light stops inside ggF production and an enhancement of the ggF rate. In [139], which discusses the light stop electroweak baryogenesis scenario, they suggest that a viable option is that this overall enhancement of ggF production does occur, but is compensated by a significant invisible Higgs boson decay into light neutralinos. Our analysis of altered Y_b as discussed above offers an alternative method to compensate for this ggF enhancement. Analogous to the decrease

of Y_b which can occur with a large positive μ as discussed in section 4.3.1, a large negative μ can increase Y_b. This would cause an increase in the BR($h \to b\bar{b}$) and subsequent decrease in all other branching ratios, compensating for the ggF enhancement in these other channels. Of course, $\mu_{ggF,bb}$ would be > 1 in this scenario, but this is still compatible with current LHC data given the very large error in this channel.

4.3.3 Sbottom quark effects

Similarly to stops, light sbottoms loops may also alter Higgs production via ggF and decay to di-photons. However, there are some important differences between the sbottom loop contribution and the stop loops.

In the decoupling limit, the Higgs coupling to sbottoms is given by

$$\hat{g}_{h\tilde{b}_1\tilde{b}_1} = \cos 2\beta \left(-\frac{1}{2}\cos^2\theta_{\tilde{b}} + \frac{1}{3}\sin^2\theta_W \cos 2\theta_{\tilde{b}} \right) + \frac{m_b^2}{M_Z^2} + \frac{m_b X_b}{2M_Z^2}\sin 2\theta_{\tilde{b}}, \tag{4.45}$$

where $\theta_{\tilde{b}}$ is the sbottom mixing angle defined by

$$\sin 2\theta_{\tilde{b}} = \frac{2m_b X_b}{m^2_{\tilde{b}_1} - m^2_{\tilde{b}_2}} \tag{4.46}$$

with $X_b = A_b - \mu \tan\beta$.

The first major difference with respect to the stop case is that this coupling does not have any dependence on X_t, and hence is not constrained by the requirement of $m_h \approx 125$ GeV. In particular, when $m_{\tilde{b}_1} < m_{\tilde{b}_2}$ with a large positive μ and $\tan\beta$, leading to a large negative X_b, it can be shown than $\sin 2\theta_{\tilde{b}} \sim 1$. The last term in Equation (4.45) therefore dominates, giving

$$\hat{g}_{h\tilde{b}_1\tilde{b}_1} \simeq \frac{m_b X_b}{2M_Z^2} \tag{4.47}$$

and leading to a large negative coupling due to the negative X_b. As the Higgs-sbottom coupling ultimately depends on X_b^2, via the $\sin 2\theta_{\tilde{b}}$ term (Equation 4.46), it is also possible to get a large negative coupling if μ is large and negative such that X_b is large and positive. However, as we are interested in the parameter space where Y_b has the possibility of being small, which requires a positive μ (see section. 4.3.1), we have only considered positive μ.

The second important difference with respect to the stop case is that for sbottoms $N_{c,b}Q_b^2 = 1/3$ compared with $N_{c,t}Q_t^2 = 4/3$ for stops. This will not affect gluon fusion, but the $\frac{N_{c,s}Q_S^2}{m_S^2}$ factor in equation. 4.31 tells us that the sbottom mass will need to be $\frac{1}{2}$ that of a stop mass with the same coupling strength to the Higgs boson in order to produce the same alteration in decay to di-photons.

The result of the two factors discussed above is that firstly, due to the opposing effects of the sbottom coupling having a larger maximum magnitude compared to stops, but the sbottom loop effects on decay to di-photons being suppressed by a factor of $\frac{Q_t^2}{Q_b^2}$ compared to stops, the relative effects of sbottom loops on $\kappa_{\gamma\gamma}$ compared to stop loops is difficult to predict. Secondly, the maximum effect of sbottom loops on gluon fusion can be larger than that of a stop with the same mass. This is because the coupling isn't constrained by the Higgs mass, and can become larger in magnitude than the stop coupling, while the loop contribution isn't constrained by a charge factor as is the case for di-photon decay.

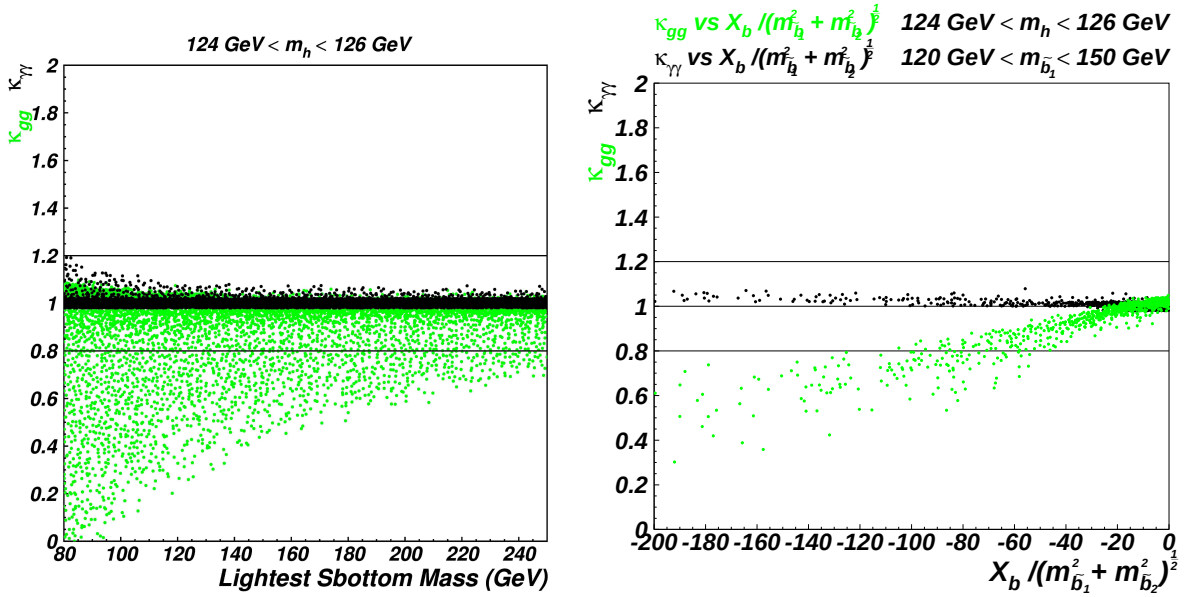

(a) (b)

Figure 4.6: *(a) $\kappa_{\gamma\gamma}$ (black) and κ_{gg} (green) as a function of lightest sbottom mass for 124 GeV $< m_h <$ 126 GeV. (b) $\kappa_{\gamma\gamma}$ (black) and κ_{gg} (green) as functions of $\frac{X_b}{(m^2_{\tilde{b}_1}+m^2_{\tilde{b}_2})}$ for 120 GeV $\leq m_{\tilde{b}_1} \leq$ 150 GeV. To isolate the influence of light sbottoms, the following cuts are also applied: $m_{H^\pm}$, $m_{\chi^\pm_{1,2}}$, $m_{\tilde{t}_{1,2}}$, $m_{\tilde{\tau}_{1,2}}$, $m_{\tilde{b}_2} > 300$ GeV.*

Both of these effects can be observed in Figure 4.6(a). We see that the largest possible increase in $\kappa_{\gamma\gamma}$ (black) for a given sbottom mass is smaller than that for a stop of the same mass, and only very light sbottoms $\simeq 80$ GeV are able to produce $\kappa_{\gamma\gamma} \approx 1.2$ (compared to $m_{\tilde{t}_1} \approx 120$ GeV). Also, as expected, κ_{gg} (green) has a larger reduction for sbottoms compared to stops of similar mass, with κ_{gg} as low as 0.7, even for $m_{\tilde{b}_1} \approx 250$ GeV.

Figure 4.6(b) shows how $\kappa_{\gamma\gamma}$ (black) and κ_{gg} (green) depend on $\sqrt{\frac{X_b}{m^2_{\tilde{b}_1}+m^2_{\tilde{b}_2}}}$ for 120 GeV $< m_{\tilde{b}_1} <$ 150 GeV, confirming that the largest deviations from the SM occur for large negative X_b, and that the effect on κ_{gg} is much larger than for $\kappa_{\gamma\gamma}$.

The combined effect of the sbottom loops can be seen in Figure 4.7(a), where the lightest sbottom mass is plotted against $\mu_{ggF,\gamma\gamma}$. We see that for the majority of parameter space,

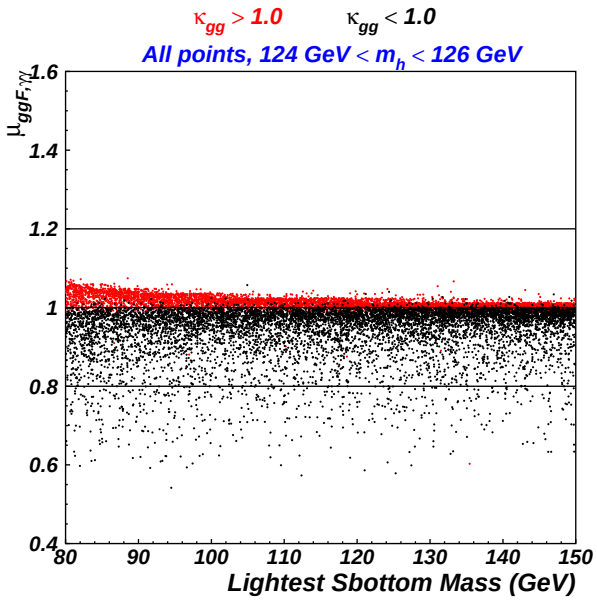

(a)

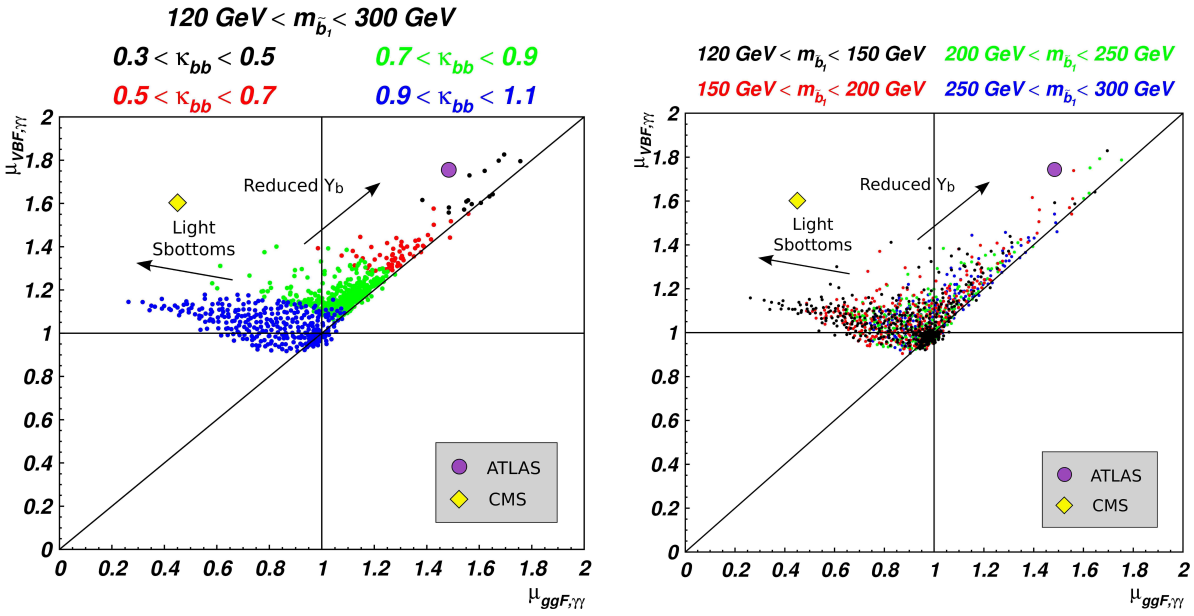

(b)(i) (b)(ii)

Figure 4.7: *(a) $\mu_{ggF,\gamma\gamma}$ vs lightest sbottom mass for $\kappa_{gg} > 1$ (red) and $\kappa_{gg} \leq 1$ (black). We have cut for $0.98 \leq \kappa_{bb} \leq 1.02$ to remove the possible effect of a reduced $\Gamma_{hb\bar{b}}$. (b) Each point of the scan with $120\ GeV \leq m_{\tilde{b}_1} \leq 300\ GeV$ is plotted on the (μ_{VBF}, μ_{ggF}) plane, with colours to indicate (i) different values for κ_{bb}, (ii) different $m_{\tilde{b}_1}$ masses. The results from ATLAS (purple circle) and CMS (yellow diamond) are indicated for comparison. In all the plots, $124\ GeV \leq m_h \leq 126\ GeV$, and to isolate the influence of light sbottoms the following cuts are also applied: $m_{H^\pm}$, $m_{\chi^\pm_{1,2}}$, $m_{\tilde{t}_{1,2}}$, $m_{\tilde{\tau}_{1,2}}$, $m_{\tilde{b}_2} > 300\ GeV$.*

$\mu_{ggF,\gamma\gamma}$ is suppressed, other than a small region where it is increased due an increased κ_{gg}. This small region of increased κ_{gg} occurs for very small values of X_b where the final term of

Equation (4.45) does not dominate and the coupling is small and positive.

If we consider the possibility of counteracting the effect of a reduced κ_{gg} by reducing $\Gamma_{b\bar{b}}$ as we did for the stops, we find that we would expect sbottom loops to have a qualitatively similar effect to stop loops in the $(\mu_{VBF+VH}, \mu_{ggF+ttH})$ plane. As in the stop case, VBF production channels will be unaffected by the gluon fusion rate, but the decays to all particles (other than sbottoms) will still be increased by the reduction in $\Gamma_{b\bar{b}}$, such that $\mu_{VBF,\gamma\gamma} > \mu_{ggF,\gamma\gamma}$.

This is demonstrated in Figure 4.7(b)(i), which is analogous to Figure 4.4(b)(i) for stops, where we have plotted $\mu_{VBF,\gamma\gamma}$ versus $\mu_{ggF,\gamma\gamma}$ for different values of $\kappa_{b\bar{b}}$, for 120 GeV $< m_{\tilde{b}_1} <$ 300 GeV. In the case of sbottoms, as the arrows indicate, their main effect is to reduce κ_{gg}, reducing $\mu_{ggF,\gamma\gamma}$, with a much smaller effect on $\kappa_{\gamma\gamma}$, producing only a small increase in $\mu_{VBF,\gamma\gamma}$. The reduced Yukawa coupling to bottoms then reduces the total width, causing a universal increase in $\mu_{\gamma\gamma}$ irrespective of the production channel. Overall, we see that in this situation light sbottoms are able to produce fairly large non-universal alterations, which would give $\frac{\mu_{VBF,\gamma\gamma}}{\mu_{ggF,\gamma\gamma}>1}$, and that due to the lack of correlation between the Hbb coupling and the Higgs mass, their maximum possible effect is larger than that of similarly light stops. Figure 4.7(b)(ii) is similar to Figure 4.7(b)(i), but with the colours indicating the sbottom mass range in each case. We see that the largest effects are produced by the lightest sbottoms as expected, but that a significant effect giving $\frac{\mu_{VBF,\gamma\gamma}}{\mu_{ggF,\gamma\gamma}} \sim 1.2$ is still possible for sbottoms as heavy as 250 GeV $\leq m_{\tilde{b}_1} \leq$ 300 GeV.

4.3.4 Stau effects

In addition to light stops and sbottoms, the lightest stau may give important contributions that in particular could enhance $\kappa_{\gamma\gamma}$. For staus, $N_c Q^2 = 1$, a factor of 3 larger than sbottoms, and since the Higgs-stau coupling like the Higgs-sbottom coupling also does not depend on X_t and therefore isn't constrained by the Higgs mass, light stau effects on $\Gamma(h \to \gamma\gamma)$ could be more significant than sbottom effects. Obviously the $SU(3)_{\rm C}$ singlet stau does not affect κ_{gg}.

The Higgs coupling to the lightest stau, normalised by $v/\sqrt{2} = M_W/g$, with v the SM Higgs VEV, is given by

$$\hat{g}_{h\tilde{\tau}_1\tilde{\tau}_1} = \cos 2\beta \left(-\frac{1}{2}\cos^2\theta_{\tilde{\tau}} + \sin^2\theta_W \cos 2\theta_{\tilde{\tau}} \right) + \frac{m_\tau^2}{M_Z^2} + \frac{m_\tau X_\tau}{2M_Z^2} \sin 2\theta_{\tilde{\tau}}. \tag{4.48}$$

with $X_\tau = A_\tau - \mu \tan\beta$.

Similarly to sbottoms, for a large positive μ, with large $\tan\beta$, X_τ is large and negative, and we find that

$$\hat{g}_{h\tilde{\tau}_1\tilde{\tau}_1} \simeq \frac{m_\tau X_\tau}{2M_Z^2}, \tag{4.49}$$

which is large and negative. Thus the stau contribution may enhance $\Gamma(h \to \gamma\gamma)$ in a large

$\tan\beta$ scenario with large and positive μ. (As in the sbottom case, a large negative μ would also give rise to a large negative coupling, but we only consider positive μ, as required such that Y_b may be reduced). As intimated, since $N_c Q^2$ is 3 times larger for the stau than the sbottom, the minimum mass at which its contribution to $\kappa_{\gamma\gamma}$ can become large is approximately a factor of $\sqrt{3}$ times heavier than for the sbottom.

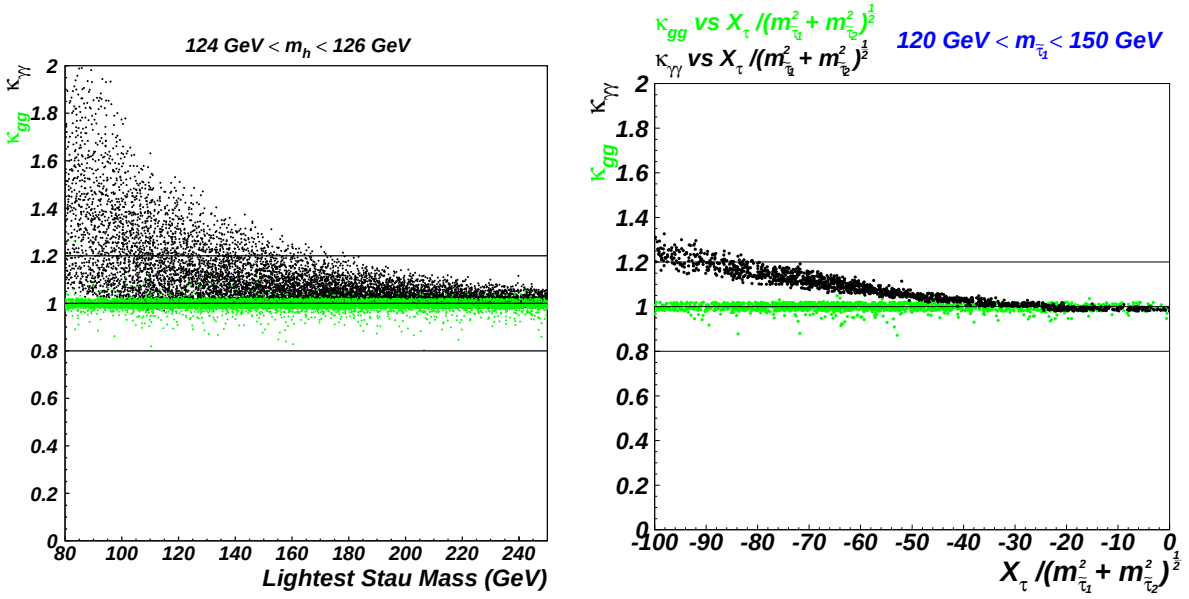

(a) (b)

Figure 4.8: *(a) $\kappa_{\gamma\gamma}$ (black) and κ_{gg} (green) as a function of lightest stau mass for 124 GeV $< m_h <$ 126 GeV. (b) $\kappa_{\gamma\gamma}$ (black) and κ_{gg} (green) as functions of $\frac{X_\tau}{(M^2_{\tilde{\tau}_1}+M^2_{\tilde{\tau}_2})}$ for 120 GeV $\leq m_{\tilde{t}_1} \leq$ 140 GeV. To isolate the influence of light staus, the following cuts are also applied: $m_{H^\pm}$, $m_{\chi^\pm_{1,2}}$, $m_{\tilde{t}_{1,2}}$, $m_{\tilde{b}_{1,2}}$, $m_{\tilde{\tau}_2} > 300$ GeV.*

This is demonstrated in Figure 4.8(a), where $\kappa_{\gamma\gamma}$ (black) is plotted against the stau mass, indeed showing that we can have $\kappa_{\gamma\gamma} > 1.2$ when $m_\tau \lesssim 180$ GeV. It also shows that light staus have no effect on κ_{gg} as expected. (The points with a slight reduction in κ_{gg} have sbottoms or stop masses ~ 300 GeV, just above the mass cut applied for these particles). In Figure 4.8(b), $\kappa_{\gamma\gamma}$ and κ_{gg} are plotted against $\frac{X_\tau}{\sqrt{(M^2_{\tilde{\tau}_1}+M^2_{\tilde{\tau}_2})}}$, showing that as for the sbottom, the coupling becomes largest for large and negative X_τ.

As staus are colourless and do not affect the gluon-gluon fusion production channel, $\mu_{ggF,\gamma\gamma}$ follows a very similar pattern to $\kappa_{\gamma\gamma}$. This is illustrated in Figure 4.9(a) where we see that for $m_{\tilde{\tau}_1} \lesssim 180$ GeV, the value of $\mu_{ggF,\gamma\gamma}$ can be > 1.2.

In Figure 4.9(b(i,ii)), we see that the effect of the light staus on the $(\mu_{VBF+VH}, \mu_{ggF+ttH})$ plane is as expected, causing a universal increase in decay to di-photons irrespective of production channel, magnifying also universal effects which may be caused by a reduction in $\Gamma_{hb\bar{b}}$.

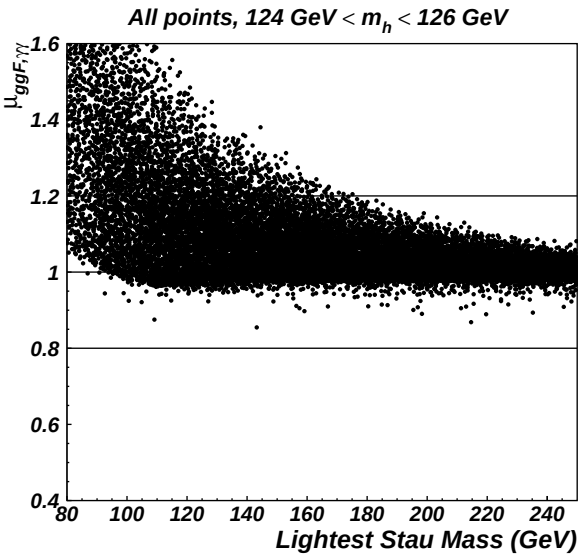

(a)

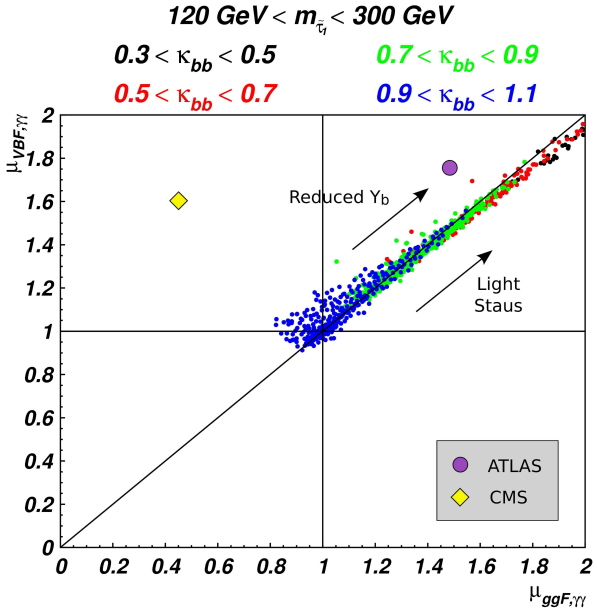

(b)(i)

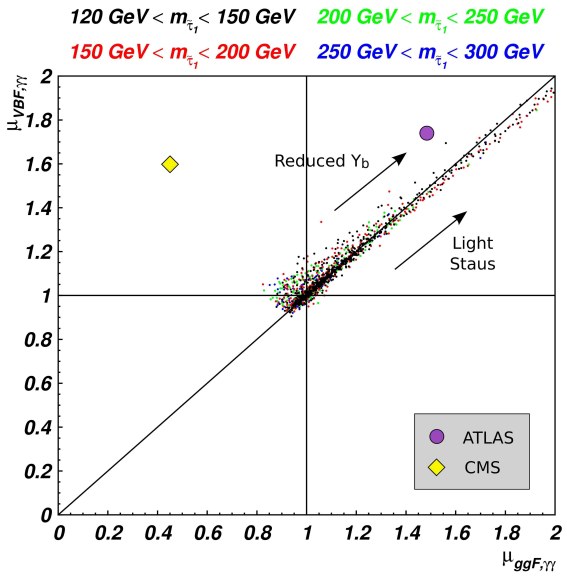

(b)(ii)

Figure 4.9: *(a) $\mu_{ggF,\gamma\gamma}$ vs lightest stau mass. We have cut for $0.98 \leq \kappa_{bb} \leq 1.02$ to remove the possible effect of a reduced $\Gamma_{h\bar{b}b}$. (b) Each point of the scan with $120\ GeV \leq m_{\tilde{\tau}_1} \leq 300\ GeV$ is plotted on the (μ_{VBF}, μ_{ggF}) plane, with colours to indicate (i) different values for κ_{bb}, (ii) different $m_{\tilde{\tau}_1}$ masses. The results from ATLAS (purple circle) and CMS (yellow diamond) are indicated for comparison. In all the plots, $124\ GeV \leq m_h \leq 126\ GeV$, and to isolate the influence of light staus the following cuts are also applied: $m_{H^\pm}$, $m_{\chi^\pm_{1,2}}$, $m_{\tilde{t}_{1,2}}$, $m_{\tilde{b}_{1,2}}$, $m_{\tilde{\tau}_2} > 300\ GeV$.*

4.3.5 Combined effect and fit of the LHC data

Thus far all of our plots have focused on $gg \to h$ and/or $h \to \gamma\gamma$. In Figure 4.10 we present results for μ_{VBF} versus μ_{ggF} for the $\gamma\gamma$, WW, ZZ, $\tau\tau$ and $b\bar{b}$ decay channels in the (μ_{VBF}, μ_{ggF}) plane,

where we have included all points from our scan for which any or all of the scenarios discussed in the previous subsections are realised.

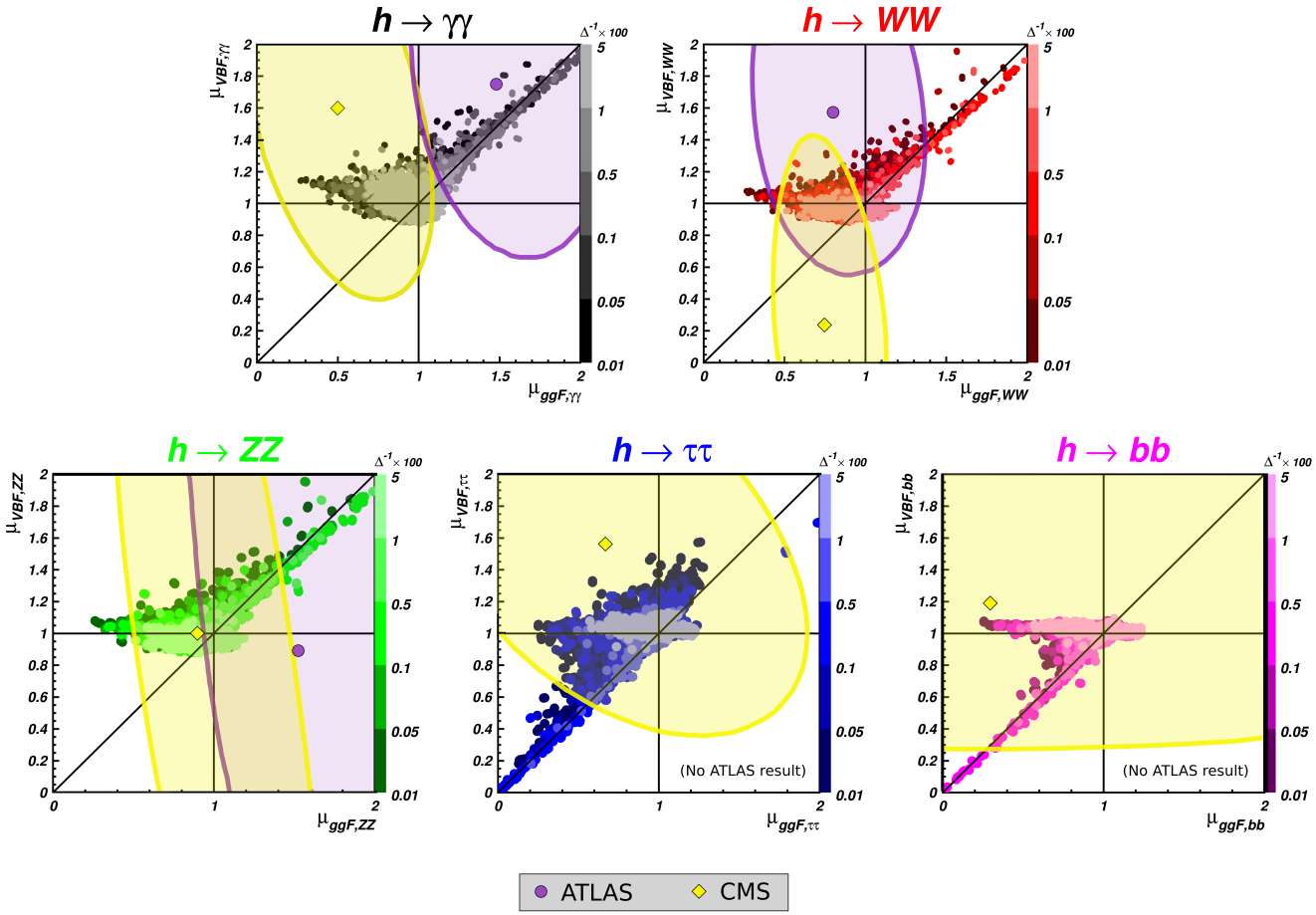

Figure 4.10: *μ_{VBF} vs μ_{ggF} for the di-photon, WW, ZZ, $\tau\tau$ and $b\bar{b}$ decay channels where the lightest stop and/or lightest stau and/or lightest sbottom has a mass between 120 GeV - 300 GeV. ATLAS (circle) and CMS (square) best fit results for each channel are also plotted. The 68% Confidence Level (CL) for the experimental results are included. ATLAS results were not available for the $b\bar{b}$ and $\tau\tau$ channels. Colour gradients denote different values of the fine-tuning parameter $\Delta^{-1} \times 100$ as described in subsection 4.3.2.*

We see that for each final state, the majority of parameter space has $\mu_{VBF} > \mu_{ggF}$, and comparing with experimental measurements, 6 out of 8 measurements have $\mu_{VBF} > \mu_{ggF}$ for their best fit values. Therefore we would expect that the MSSM will provide a better fit to the data, and that in general the light stop and sbottom scenarios will be able to explain a non-universal alteration of $\mu_{VBF} > \mu_{ggF}$ if this is confirmed at the upgraded LHC starting in 2015. In Figure 4.10 we have also stratified by shading according to the values of the fine-tuning parameter Δ, as described in section 4.3.2. We see that the points with a large universal

increase in μ_{ggF} and μ_{VBF} have a larger fine tuning in general (smaller Δ^{-1} in the plots). This is expected, as for these points μ, on which Δ depends, is required to be large to reduce Y_b as discussed in section 4.3.1.

It is interesting to note that in general it is not possible to satisfy both the ATLAS and CMS results simultaneously as there is a slight tension between them for each channel (although within large errors). As an example, for the di-photon decay channel, whilst both experiments prefer $\frac{\mu_{VBF,\gamma\gamma}}{\mu_{ggF,\gamma\gamma}} > 1$, CMS favours $\mu_{ggF,\gamma\gamma} < 1$ requiring only a light stop or sbottom, while ATLAS favours $\mu_{ggF,\gamma\gamma} > 1.5$ which would require both a light squark *and* a reduced Y_b or light stau.

To quantify how well the scenarios we have discussed fit current LHC data, we have calculated the χ^2 for each scenario having compared to the experimental best fit values for μ_{ggF} and μ_{VBF} for each decay channel show in Figure 4.1. For each collaboration (ATLAS, CMS) the systematic errors on the values of μ_{ggF} and μ_{VBF} for a single decay mode are correlated. To take this correlation into account, we actually calculate a "profiled log likelihood ratio" test statistic. However, under the assumption that the data is distributed as a multivariate Gaussian (valid to a good approximation), this reduces to a χ^2 statistics with a non-diagonal covariance matrix. This is discussed fully in [36]. There are 6 degrees of freedom from the ATLAS data and 10 from the CMS data, giving 16 degrees of freedom overall (3 channels for ATLAS ($\gamma\gamma$, WW and ZZ) and 5 from CMS ($\gamma\gamma$, WW, ZZ, $\tau\tau$, $b\bar{b}$), each with ggF and VBF channels). The regions of interest for which a χ^2 was calculated were defined as; 1) light stops only, 2) light sbottoms only, 3) light staus only, 4) lights stops and/or sbottoms and/or staus. In each case a "light" mass was defined as between 120 and 300 GeV.

For each scenario, we have calculated the χ^2 for every point from our parameter space scan that matched the relevant particle mass criteria. The results are presented in Figure 4.11 as the χ^2 per degree of freedom (χ^2/N_{DOF}), when compared to (a) just the ATLAS results, (b) just the CMS results, (c) both ATLAS and CMS results. The width of each block is proportional to the number of points in each region of parameter space with each particular value of χ^2, where each parameter space is defined as points satisfying 124 GeV $< m_h <$ 126 GeV, and other mass constraints as described in the caption to Figure 4.11.

First of all, we can see that the SM already fits the data well with a $\chi^2/N_{\text{DOF}} \sim 1$ when compared to ATLAS results only (Figure 4.11(a)), a $\chi^2/N_{\text{DOF}} \sim 0.6$ when compared to CMS results only (Figure 4.11(b)), and a $\chi^2/N_{\text{DOF}} \sim 0.75$ when compared to both the ATLAS and CMS combined results (Figure 4.11(c)). The χ^2/N_{DOF} for the SM is lower when calculated using CMS results rather than ATLAS results, which occurs mainly because the CMS signal strength best fit points for $h \to ZZ$ are very close to the SM values, and the best fit point for $\mu_{ggF,bb}$

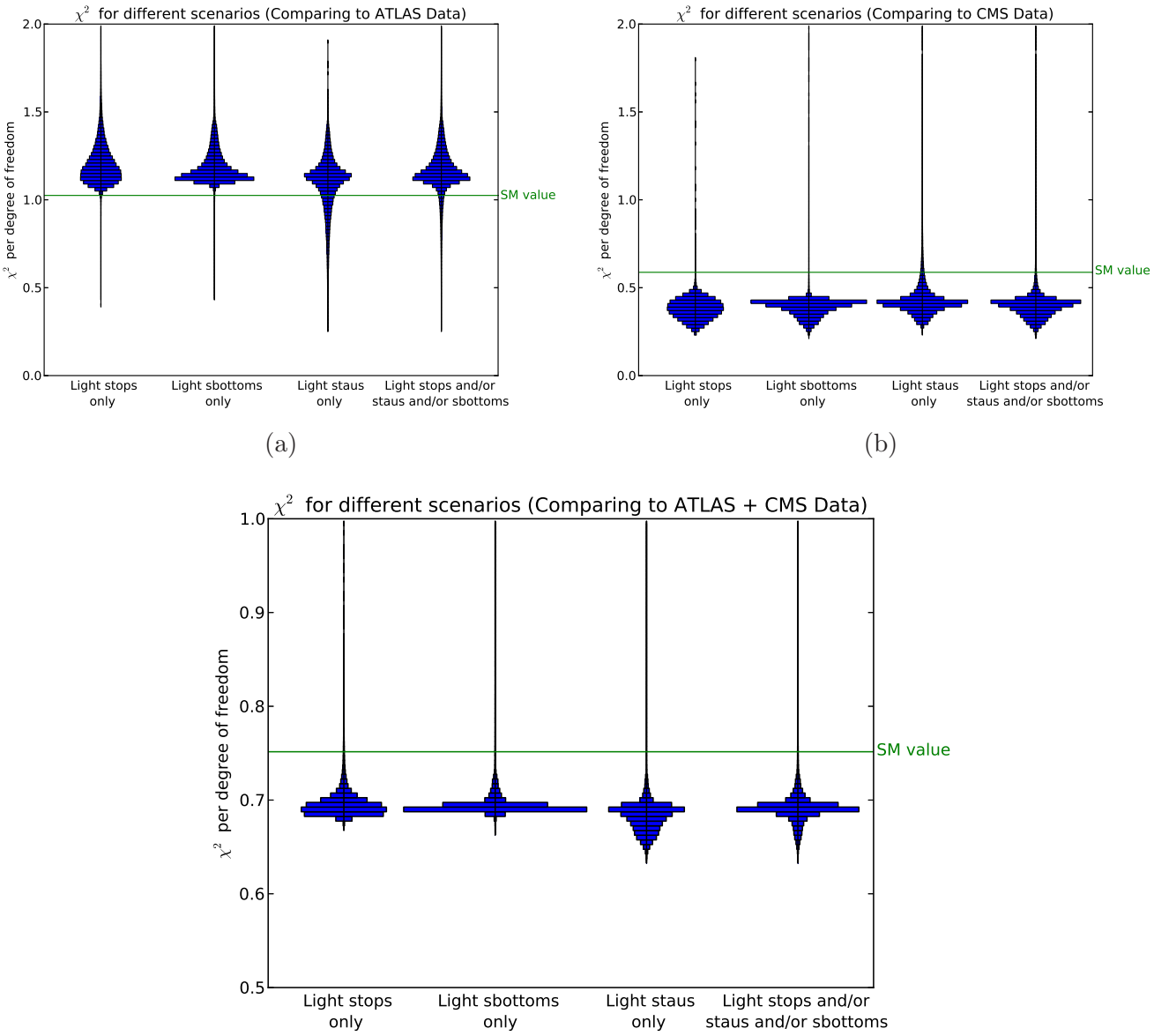

Figure 4.11: *χ^2 results per degree of freedom for different regions in parameter space compared to (a) ATLAS data, (b) CMS data, (c) combined ATLAS+CMS data. The width of each block is proportional to the number of points in each region of parameter space with each particular value of χ^2. The light stop, sbottom and stau regions are defined as 120 $GeV \leq m_i \leq 300$ GeV, where $m_i = m_{\tilde{t}_1}, m_{\tilde{b}_1}, m_{\tilde{\tau}_1}$ respectively. The SM fit to data is indicated by the green line for each plot.*

has very large error bars. For the MSSM, the majority of points in our parameter spaces fits the ATLAS results worse than the SM, but have a lower χ^2/N_{DOF} than the SM when compared to either the CMS results only, or to the combined ATLAS and CMS data. The scenarios with the lowest χ^2/N_{DOF} are the combined scenario allowing all masses to be light, and the scenario with light staus only.

4.4 Conclusions

In this chapter we have explored the effects of light sfermions on the production and decay of the lightest Higgs boson within the MSSM, culminating with a fit of the relevant parameter space to LHC data.

We have found that scenarios with light coloured sfermions, namely stops and sbottoms, have the potential to explain a non-universal alteration of the two most relevant Higgs production channels, *i.e.*, $\mu_{VBF} \neq \mu_{ggF}$, and predicts $\frac{\mu_{VBF}}{\mu_{ggF}} > 1$ in all Higgs boson decay channels for the majority of the parameter space. These light stop and light sbottom scenarios are realised in specific regions of the parameter space in terms of soft-breaking mass terms, namely where $M_{Q3} >> M_{U3}$ and $M_{Q3} >> M_{D3}$, respectively.

The specific feature of the scenario with a light stop is that $\hat{g}_{h\tilde{t}_1\tilde{t}_1}$ is negative (whenever one is near maximal stop mixing), which makes the overall stop loop contribution of the opposite sign as the top quark contribution and of same sign as the W loop. As a result, one obtains a decreased k_{gg} and an increased $k_{\gamma\gamma}$ couplings, with the relative decrease of k_{gg} being bigger than the relative increase of $k_{\gamma\gamma}$. Therefore, the overall effect of light stops alone would lead to a decrease of the Higgs production via gluon-gluon fusion decaying to di-photons ($\mu_{ggF,\gamma\gamma}$) as well as a reduction in μ_{ggF} compared to the SM for all decay channels. This scenario would be somewhat consistent with CMS data, where $\mu_{ggF} < 1$ for all decay channels.

However, this prediction is in tension with the ATLAS data, where $\mu_{ggF} \approx 1.5$ for both the $\gamma\gamma$ and ZZ decay channels. Therefore, we also consider the scenario where we have both light stops and a suppressed $hb\bar{b}$ coupling. In this case, the reduced $h \to b\bar{b}$ partial width (and related κ_{bb} parameter) causes an enhancement of the BRs and hence signal strengths of the other decay channels, which can compensate for the reduced production via ggF. Depending on the degree of suppression of the $hb\bar{b}$ coupling, the ggF signal strength in all channels can be increased, either to match the SM level, or greater, *e.g.*, to $\mu_{ggF} \approx 1.5$, in order to be more consistent with the ATLAS data. The exceptions being $\mu_{ggF,\gamma\gamma}$, which can be slightly enhanced compared to other channels, and $\mu_{ggF,bb}$, which would be reduced compared to the other channels. This reduction of the $hb\bar{b}$ coupling was achieved with a large μ (1–5 TeV), intermediate M_A (300–800 GeV) and intermediate-to-large $\tan\beta$ (20–50). In this light stop scenario, $\hat{g}_{h\tilde{t}_1\tilde{t}_1}$ is approximately fixed (in the maximal mixing scenario) to around $-\frac{1}{2}\frac{m_t^2}{M_Z^2}$, which limits the maximal contribution of the stop to Higgs production via ggF and decay via $h \to \gamma\gamma$.

We have also found that the effect from light sbottoms on the gluon fusion rate can potentially be larger than that of light stops, since the Higgs-sbottom-sbottom coupling is not correlated with the Higgs boson mass. Overall, we can see that in the light stop/sbottom scenarios, $\mu_{ggF,bb}$ and $\mu_{VBF,bb}$ are predicted to be at or below one, especially the $\mu_{ggF,bb}$ value,

which can be doubly suppressed both via ggF production (due to the negative interference from stop/sbottom loops) and from decay (due to κ_{bb} suppression). Therefore, in future LHC runs, the measurement of $\mu_{ggF,bb}$ and $\mu_{VBF,bb}$ would be particularly important to help rule out these scenarios.

In contrast, light staus were found to only be able to universally increase the signal strengths, irrespective of the production channel, generally complementing the effect of a reduced $hb\bar{b}$ coupling.

Furthermore, we showed that the non-universal solutions ($\mu_{ggF} \neq \mu_{VBF}$) had a fairly low minimum fine-tuning measure, as low as $\sim 5\%$, while in regions where a universal increase in signal strength ($\mu_{ggF} \sim \mu_{VBF} > 1$) is caused due to a suppressed Y_b, the fine-tuning was much larger due to the requirement of a large μ parameter.

Finally, we performed a χ^2 fit for these MSSM scenarios, which showed that for every one of the scenarios we considered, the majority of points in their parameter spaces fitted combined ATLAS and CMS data better than the SM.

To conclude, we have found that the MSSM with light stops or sbottoms has the potential to explain a non-universal alteration from SM values of the Higgs production rates in different channels, and that this can be complemented by a reduced Γ_h to increase the relevant signal strengths to be equal to or greater than the SM prediction.

Chapter 5

Ruling out Light Stops

5.1 Overview

As discussed in the thesis introduction, extending the spacetime symmetries to include supersymmetry has proven to be a popular BSM and is one of the main discovery goals at the LHC. Within its minimal extension, the MSSM, a common and important scenario is where the SUSY partner of the top quark, the stop is the lightest squark.

There are a number of reasons why the stop is commonly taken to be the lightest squark. Firstly, this arises naturally in SUSY models where universality of its masses at a high scale is assumed. In this case renormalisation group (RG) equations are used to then run these masses down from the Grand Unified Theory (GUT) scale to the electroweak scale (EW). In the MSSM, Yukawa couplings have the effect of reducing the masses at the EW scale, therefore the stop mass, which has the large top Yukawa in its RG equations, tends to be pushed to a lower value than the other squark masses. This assumption of universality is reasonably well motivated because SUSY allows unification of the gauge couplings at a high scale in GUT models such as $SU(5)$ and $SO(10)$. This provides the theory with a high scale where we can also envisage unification of some of the other Lagrangian parameters. This, combined with the observation that without universality the MSSM has around 120 additional free parameters compared to the SM, has traditionally made such constrained models popular. The large top Yukawa also leads to light stops for another reason. The mass mixing in the squark sector is proportional to the Yukawa coupling, thus the top Yukawa leads to a large mass splitting for the stops, with the consequence of one stop being light.

One of the main motivations for SUSY is that it solves the gauge hierarchy problem. When SUSY is softly broken, logarithmic terms related to the stop mass are re-introduced to the loop corrections to the Higgs mass squared parameter. If the stop masses become too large

then SUSY is no longer a satisfactory solution to the hierarchy problem, and thus arguments of naturalness prefer low stop masses with ideally $m_{\tilde{t}} \approx m_t$.

Light stops are also important from a cosmological point of view. They are able to lead to the correct relic density of dark matter through co-annihilation of the neutralino with the light stop[140–144], and they also enable electroweak baryogenesis (EWBG) sufficiently strong to explain the matter-antimatter asymmetry present in the universe today. Electroweak baryogenesis refers to any mechanism that produces an asymmetry in the density of baryons during the electroweak phase transition. For this to occur, the 3 Sakharov conditions must be satisfied[145]: (*i*) Departure from thermodynamic equilibrium, (*ii*) Violation of baryon number, (*iii*) C- and CP-violating scattering processes. In the MSSM, there is a small region of parameter space where the departure from thermodynamic equilibrium is sufficiently strongly first order to produce the observed matter asymmetry, and in this region the lightest stops mass has to be lighter than the top quark (i.e. $m_{\tilde{t}} \lesssim 174$ GeV)[146]. In relation to baryogenesis this is often called "*the light stop scenario*".

Finally, light stops are important due to their ability to enter loops, altering Higgs production and decay, as discussed in Chapter 4.

The purpose of work discussed in this chapter will be to extend current exclusion limits on the light stops, with the aim of increasing the minimum excluded mass, limiting its maximum possible effects on Higgs processes, and potentially ruling out the light stop scenario of baryogenesis.

5.2 Stop decay channels

With the assumption that the neutralino is stable and is the lightest supersymmetric particle, there are only two likely final states for stop decays for the vast majority of $m_{\tilde{t}}$ and $m_{\tilde{\chi}_1^0}$ values. The stop either decays to a 2-body state via $\tilde{t} \to \tilde{\chi}_1^0 c$, which is a flavour changing decay, or to a 4-body final state $\tilde{t} \to bff'\tilde{\chi}_1^0$, where f and f' are the decay products of a W-boson, with the W and b quark arising from a decaying top quark, which is therefore a flavor conserving decay. For this reason, the stop searches conducted by ATLAS and CMS only consider these two possibilities. However, in order to simplify their analysis, they go further assuming a 100% branching ratio (BR) to each of these in turn, a simplification which isn't valid for much of the parameter space. Here we discuss these two channels.

5.2.1 Two-Body Decay, $\tilde{t} \to \tilde{\chi}_1^0 c$

The stop is able to decay via a flavour changing neutral current (FCNC) to either a charm or an up quark, and the lightest neutralino. If the model doesn't have flavour violation (FV) at tree level, then this can occur at the loop level due to the CKM matrix.

In general in the MSSM, the quark and squark mass matrices are not simultaneously diagonalisable, which leads to flavour violation at tree level. However, stringent limits have been placed on flavour changing neutral currents from K, D and B meson studies setting tight limits on the possible contribution to FCNC from new physics[147–149]. In order to explain why flavour violation is so small in the MSSM, the Minimal Flavour Violation (MFV) framework[150–152] has been developed. It proposes that the quark and squark mass matrix are simultaneously diagnoalisable at a certain energy scale. However, flavour mixing is subsequently induced through renormalisation group equations (RGE) allowing tree level FCNC. As these depend on the CKM matrix elements, the decay width of a stop to a neutralino and an up quark is around $\mathcal{O}(10^{-2})$ that of a decay to a charm. Furthermore, the loop induced decays will also favour charm production over up quarks. Due to these considerations, only the $\tilde{t} \to \tilde{\chi}_1^0 c$ decay is considered by CMS and ATLAS.

An important question to consider, is which regions of the MSSM parameter space is this 2-body decay likely to have a large branching fraction. In particular, for what values of $m_{\tilde{t}}$ and $m_{\tilde{\chi}_1^0}$ is this decay allowed and/or likely? The most useful parameter in this respect is the mass gap between the stop and the neutralino, $\Delta m = m_{\tilde{t}} - m_{\tilde{\chi}_1^0}$. Recent work to study this question[153, 154] has showed that the answer is, as would be expected, heavily dependent on the pattern and degree of flavour violation. However in general, this 2-body decay becomes more likely as Δm gets smaller, and both flavour violating scenarios they considered had a near 100% BR to 4-body by $\Delta m \lesssim 20$ GeV. Once $\Delta m \lesssim 5$ GeV this will be the only remaining channel as the 4-body will be disallowed due to the mass of the bottom quark. Importantly, they also showed that this 2-body decay can have a sizeable BR ($> 10\%$) up to $\Delta m = 110$ GeV, even when the flavour changing was required to be within experimental bounds. A plot from their paper demonstrating this is reproduced in Figure 5.1, where $m_{\tilde{u}_1}$ is identified with the lightest stop. This result was assuming a specific pattern of flavour violation. In a more general case it seems likely that stop 2-body decays to charms can remain important for even higher mass gaps. i.e. $\Delta m > 110$.

In summary, this 2-body decay will tend to have a high BR when $\Delta m < 20$ GeV, but this branching fraction can still be sizeable up to mass gaps of at least $\Delta m = 110$ GeV.

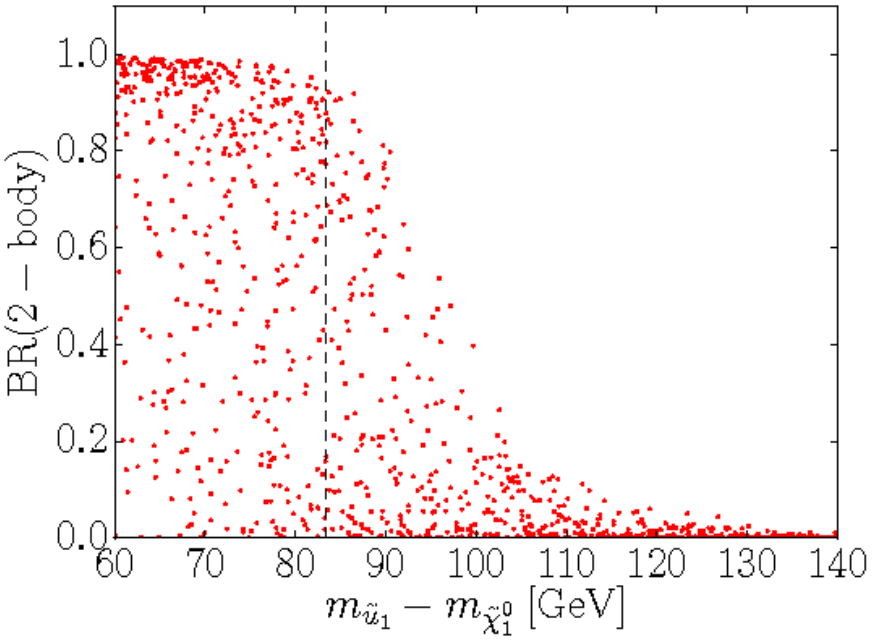

Figure 5.1: *Plot from the paper[154], showing the stop branching ratio to charm and neutralino (2-body) for different values of* $\Delta m = m_{\tilde{u}_1} - m_{\tilde{\chi}_1^0}$.

5.2.2 Four-Body Decay, $\tilde{t} \to bff'\tilde{\chi}_1^0$

In considering the four body decays of the stop, if we allow flavour changing vertices, as well charginos, charged Higgs or squarks in the decay chain, there are a large number of diagrams, and any of the other down-type quarks could replace the bottom in $\tilde{t} \to bff'\tilde{\chi}_1^0$. However, unlike in the 2-body case, this process can and is generally more likely to occur without flavour violation. Furthermore all of the other SUSY particles (sometimes with the exception of the chargino) are often taken to be too heavy to contribute significantly to the cross section. As a result, only one decay chain is usually considered, which doesn't have any flavour changing, and doesn't contain SUSY particles as intermediate particles, namely $\tilde{t} \to t\tilde{\chi}_1^0$, with $t \to bW$, and then $W \to ff'$, giving $\tilde{t} \to bff'\tilde{\chi}_1^0$. Whilst ultimately this is a single decay channel, its kinematics depend heavily on which particles in the chain are on- or off-shell. This plays an important role in the experimental searches, as the optimal cuts to increase the signal-to-background ratio will depend on the kinematics. ATLAS and CMS therefore usually describe this single chain differently depending on the value of Δm, referring to it as $\tilde{t} \to t\tilde{\chi}_1^0$ when there is sufficient phase space for the top quark to be on-shell, $\tilde{t} \to bW\tilde{\chi}_1^0$ when the top quarks is forced to be off-shell, but the W boson can be on shell, and $\tilde{t} \to bff'\tilde{\chi}_1^0$ when neither the W or the top is able to be on shell. In this chapter we will refer to all of these scenarios as 4-body, or $\tilde{t} \to bff'\tilde{\chi}_1^0$.

The question for which regions of parameter space is this likely to be the only decay channel, is answered by looking at the 2-body decay branching ratios as discussed above and in

[153, 154]. When $\Delta m \lesssim 5$ GeV this decay is not allowed, and for a Δm of at least 110 GeV it is likely to have a BR $\sim 100\%$. For intermediate values of Δm, any BR is possible, with lower branching fractions becoming likely for small mass gaps, especially for $\Delta m < 20$ GeV.

5.3 Experimental Searches: Current Status

One of the main search focuses of the 2 main detectors at the LHC, ATLAS and CMS, has been looking for new SUSY particles, usually with the assumption that it is the MSSM that is realised. In particular, there have been a number of searches dedicated to looking for stops, which have a reasonable chance of being the lightest charged SUSY particle, and hence the easiest SUSY particle to find.

A specific search assumes a 100% BR via a specific channel, and has cuts designed to increase the SUSY signal to SM background ratio in a specific region of SUSY parameter space. As a result, different searches tend to rule out different areas of SUSY parameter space, and these are usually presented in the stop mass ($m_{\tilde{t}}$) vs neutralino mass ($m_{\tilde{\chi}_1^0}$) plane. Both ATLAS and CMS have produced summary plots, where they combine all of their stop exclusion results on a single plot. Both plots are similar, however the ATLAS exclusion limits are more stringent in the low stop mass region of interest. Both are reproduced in Figure 5.2[155–163].

Some points to note about these results. Firstly, all of these exclusions assume a single decay channel, which should be remembered when interpreting whether a region is definitively ruled out or not. Secondly, we clearly see that there are areas of parameter space which still allow light stops. If the neutralino mass, $m_{\tilde{\chi}_1^0} \gtrsim 240$ GeV, then any stop mass down to around 280 GeV is allowed. If $m_{\tilde{\chi}_1^0} \lesssim 240$ then stops as light as 110 GeV may be allowed (for a very small area of parameter space) depending on the mass gap, Δm, between the stop and neutralino. The two main regions which are not excluded even for these very light stops are where $\Delta m = m_{\tilde{t}} - m_{\tilde{\chi}_1^0}$ is just larger than M_W, and where $\Delta m \approx m_t$. In both these regions, the stop decays to an on-shell W boson or top quark, with very little energy for the neutralino. Therefore there is very little Missing Transverse Energy (MET) from the undetected neutralino, the event is difficult to distinguish from the SM background, and isn't excluded.

We are now able to be more precise in defining the goal of this chapter. It is to extend the ATLAS analysis into the region with light stops where Δm is slightly larger than M_W, with the intention of ruling out some of the lowest mass regions which still remain. We specifically choose to extend the ATLAS bounds both because in this region they are more stringent than the corresponding CMS results, and also as it was apparent that this was possible, as will be discussed in section 5.3.2.

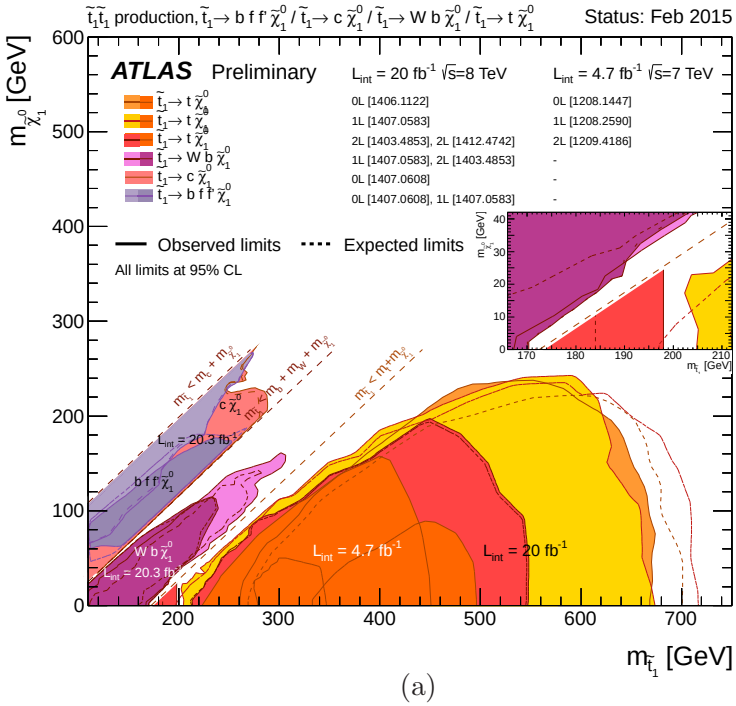

(a)

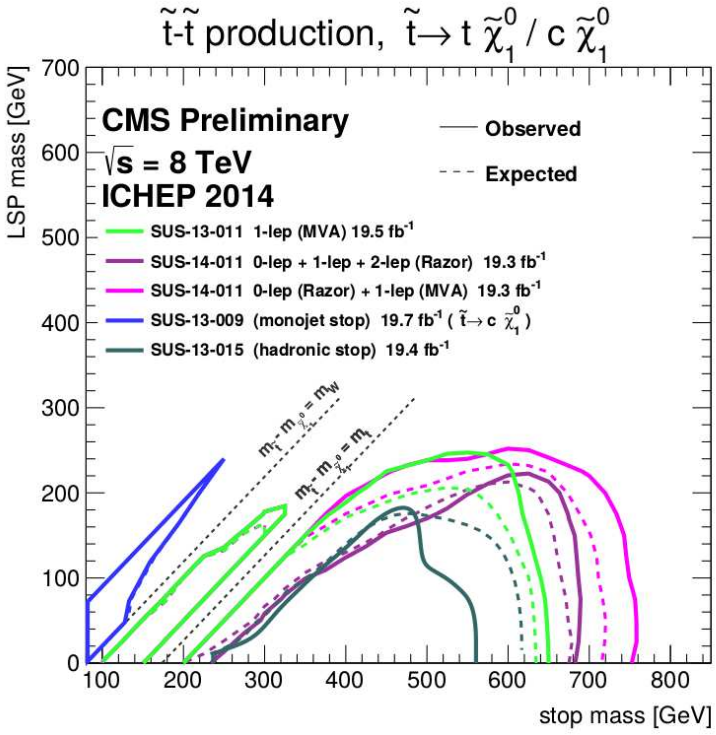

(b)

Figure 5.2: *(a) ATLAS summary plot, and (b) CMS summary plot for stop searches showing the 95% confidence limits (CL) exclusion region in the stop mass ($m_{\tilde{t}}$) vs neutralino mass ($m_{\tilde{\chi}_1^0}$) plane. Each search assumes a 100% branching ratio via certain channels as shown in the legend of the plot. [155–163].*

5.3.1 Monojet Searches

Traditionally, regions with small mass gaps between the stop and neutralino are difficult to rule out. The decay has very little phase space, and therefore all the decay products including the neutralino will have very little momentum. This is below the trigger threshold for the detectors and the event is not observed.

To counter this problem, it is possible to trigger on mono-objects, and in this particular case monojets. The idea is that in events with very hard initial state radiation, the stop recoils in the opposite direction. Upon decaying, the neutralino and other decay products are now in a boosted frame and the neutralino has a large momentum. As a result, the signature of such an event is one very high transverse momentum (p_T) jet and a high missing transverse energy (MET). These can be triggered on, and have a low SM background. All of the ATLAS searches in the $\Delta m < M_W$ region are monojet searches, with cuts for a high p_T jet and high MET.

5.3.2 Motivation for extending the ATLAS search

As stated previously, the intention is to extend the ATLAS exclusion into the $\Delta m > M_W$ region. In particular, the intention is to extend the regions in [163] and [159] (the salmon coloured and dark grey regions in Figure 5.2), which both rule out a large region where $\Delta m < M_W$, but are artificially cut off at around the $\Delta m = M_W$ line, where it looks likely they could have been extend further.

In [163] where a $\tilde{t} \to \tilde{\chi}_1^0 c$ decay is assumed, it is stated that the maximum Δm considered is 82 GeV. No further explanation is given, however its likely this is in part due to the fact that if we assume no tree level flavor violation, then the region of parameter space where the branching ratio to $\tilde{t} \to \tilde{\chi}_1^0 c$ is 100% becomes very small as Δm becomes much larger than this. However, as discussed in section 5.2.1, sizeable $\tilde{t} \to \tilde{\chi}_1^0 c$ BRs are still possible for mass gaps up to at least $\Delta m \approx 110$ GeV when flavour violation within experimental limits are allowed.

In [159] on the other hand, where a $\tilde{t} \to bff'\tilde{\chi}_1^0$ decay is assumed, they state that "*generating the full event with MadGraph would be computationally too expensive.*". As a result, their $\tilde{t}$ are decayed using Pythia, which produces isotropic decays. This will not be valid when the W bosons are on shell. This seems to be at least part of the reason the results have been restricted to $\Delta m < 80$ GeV (which isn't explicitly stated). As these omissions are both important and possible to rectify, these are the analyses we extend in this chapter.

5.4 Tools and Framework for Analysis

In order to extend these results, we reproduced the signal samples and analysis for three ATLAS analysis[159, 163] which we will call; (i) monojet analysis, (ii) monojet with c-tagging analysis, and (iii) monojet with 1 lepton analysis. They are discussed in the following subsections.

5.4.1 Analysis - Monojet, $\tilde{t} \to \tilde{\chi}_1^0 c$

This analysis is described in [163]. It assumes a 100% branching ratio to $\tilde{t} \to \tilde{\chi}_1^0 c$ and its main aim is to rule out the very small Δm region where the c-jets from the decay will usually be too soft to identify (roughly $\Delta m < 30$ GeV although ATLAS don't give a value). Therefore in monojet events the signature will be one high p_T jet and a large E_T^{miss}, with a small number of soft jets.

First, the events undergo a pre-selection, requiring an $E_T^{miss} > 150$ GeV, at least one jet with a $p_T > 150$ GeV and $|\eta| < 2.8$, and vetoing any event with a muon with $p_T > 10$ GeV or an electron with $p_T > 20$ GeV. Following this, as a result of the softness of the decay products, a maximum of three jets with $p_T > 30$ GeV and $|\eta| < 2.8$ are allowed. Additionally, the azimuthal separation between the missing transverse momentum direction and that of each jet has a minimum bound, $\Delta\phi(jet, p_T^{\text{miss}}) > 0.4$, which ATLAS used to reduce the multijet background where the large E_T^{miss} originates mainly from jet energy mismeasurement. In order to optimise the search reach, 3 separate signal regions were defined (denoted M1, M2, M3), with increasing minimum thresholds for p_T and E_T^{miss} to exclude increasing stop and neutralino masses. For the M1, M2 and M3 regions, the thresholds are respectively $p_T > 280$ GeV, $E_T^{\text{miss}} > 220$ GeV for M1, $p_T > 340$ GeV, $E_T^{\text{miss}} > 340$ GeV for M2, and $p_T > 450$ GeV, $E_T^{\text{miss}} > 450$ GeV for M3. These selection cuts are summarised in Table 5.1.

Monojet Search			
Applied to all 3 signal regions (M1, M2, M3) At most 3 jets with $p_T > 30$ GeV and $\|\eta\| < 2.8$ $\Delta\phi(jet, p_T^{\text{miss}}) > 0.4$			
Signal region	**M1**	**M2**	**M3**
Minimum leading jet p_T GeV	280	340	450
Minimum E_T^{miss} (GeV)	220	340	450

Table 5.1: *Analysis cuts for the pure monojet search in the $\tilde{t} \to \tilde{\chi}_1^0 c$ channel. There are 3 separate signal regions, M1, M2 and M3. The cuts applied to all 3 regions are in the top row, with the signal region dependent cuts in the lower row.*

The SUSY signal samples were produced at leading order using MadGraph5[50, 164, 165] with a CTEQ6L1 PDF, with the cross section rescaled using a K-factor calculated with next-to-

leading order (NLO) supersymmetric QCD corrections and the resummation of soft gluon emission at next-to-leading-logarithmic (NLL) accuracy using the NLL-fast computer program[166–168]. In view of the fact that for large Δm, the veto of any event with a fourth jet with $p_T > 30$ GeV can reduce the selection efficiency by around 50%, and that this can be from a second initial state radiation jet (with the 2$^{\text{nd}}$ and 3$^{\text{rd}}$ highest p_T jets from the c-quarks from stop decays), two-jet matching using the k_T-jet MLM scheme[169] was used to ensure accuracy of the p_T of subleading ISR jets. The showering is done using Pythia-6[170–172] and the detector simulation using Delphes-3[173–175]. The subsequent analysis and application of cuts was conducted using the ROOT Data Analysis Framework[71]. Each point in the $m_{\tilde{t}}$ vs $m_{\tilde{\chi}_1^0}$ plane was ruled out if for any of the signal regions (M1, M2, M3), the cross section of the signal sample and the efficiencies of the selection cuts predicted a larger number of signal events than the 95% confidence limits (CL) upper limit on BSM events which is provided by ATLAS in the paper.

5.4.2 Analysis - Monojet with c-tagging, $\tilde{t} \to \tilde{\chi}_1^0 c$

This analysis is also described in [163]. It again assumes a 100% branching ratio to $\tilde{t} \to \tilde{\chi}_1^0 c$, and its main purpose is to rule out the region with a larger but still relatively small Δm, (roughly 30 GeV $< \Delta m <$ 80 GeV although ATLAS don't give a value), where the c-jets from the decay will usually be hard enough to identify, but softer than the initial state radiation. Therefore the signature will be relatively large multiplicity jets with a charm jet as one of the subleading jets.

At ATLAS, the c-tagging is implemented via a dedicated algorithm using multivariate techniques which combine information from the impact parameters of displaced tracks and topological properties of secondary and tertiary decay vertices reconstructed within the jet. For this study, they used two operating points for the c-tagging called the *medium* and *loose* operating points. The *medium* operating point has a c-tagging efficiency of $\approx 20\%$, and a rejection factor of ≈ 8 for b-jets, ≈ 200 for light-flavour jets, and ≈ 10 for τ-jets, while the *loose* operating point has a c-tagging efficiency of $\approx 95\%$, with a rejection factor of ≈ 2.5 for b-jets, but no significant rejection of light-flavour or τ-jets. For our analysis, we used these quoted efficiencies and rejection factors, as well as representative data-to-simulation multiplicative scale factors given in the ATLAS paper[163] of 0.9 for simulated heavy-flavour tagging and 1.5 for mistagging of light-jets as charm jets.

Once more, the events undergo a pre-selection (slightly different to the monojet pre-selection), requiring an $E_T^{miss} > 150$ GeV, at least one jet with $p_T > 150$ GeV and $|\eta| < 2.5$, and vetoing any event with a muon or electron with $p_T > 10$.

Following this, due to the likelihood of multiple jets, a minimum of four jets with $p_T > 30$ GeV and $|\eta| < 2.5$ and $\Delta\phi(jet, p_T^{\text{miss}}) > 0.4$ are required. Additionally, there is a veto against

Monojet with c-tagging Search		
Applied to both signal regions (C1, C2)		
At least four jets with $p_T > 30$ GeV and $\|\eta\| < 2.5$		
$\Delta\phi(jet, p_T^{\text{miss}}) > 0.4$		
All four jets must pass loose tag requirements (b-jet vetoes)		
At least one medium charm tag in the three subleading jets		
Signal region	**C1**	**C2**
Minimum leading jet p_T GeV	290	290
Minimum E_T^{miss} (GeV)	250	350

Table 5.2: *Analysis cuts for the monojet with c-tagging search in the $\tilde{t} \to \tilde{\chi}_1^0 c$ channel. There are 2 separate signal regions, C1 and C2. The cuts applied to both regions are in the top row, with the signal region dependent cuts in the lower row.*

any event containing b-jets using a loose c-tag requirement, and a requirement that at least one of the three subleading jets passes a medium c-tag. Again in order to optimise the search reach, 2 separate signal regions were defined (denoted C1 and C2), both requiring their leading jet to have $p_T > 290$ GeV, but with C1 requiring $E_T^{\text{miss}} > 250$ GeV and C2 requiring $E_T^{\text{miss}} > 350$. These selection cuts are summarised in Table 5.2.

Once more, the SUSY signal samples were produced using MadGraph5 (with 2-jet matching and a CTEQ6L1 PDF), Pythia-6 and Delphes-3, with subsequent analysis conducted using ROOT. Each point in the $m_{\tilde{t}}$ vs $m_{\tilde{\chi}_1^0}$ plane was ruled out if for any of the signal regions (C1, C2) predicted a larger number of signal events than the 95% CL upper limit on BSM events provided by ATLAS.

5.4.3 Analysis - Monojet with 1 lepton, $\tilde{t} \to bff'\tilde{\chi}_1^0$

This analysis is described in [159]. It assumes a 100% branching ratio to $\tilde{t} \to bff'\tilde{\chi}_1^0$. Like the previous 2 analysis discussed above, it is separated into 2 signal regions, with the first, labelled bCa_low, aiming to probe mass scenarios where $\Delta m < 50$ GeV, and the second, bCa_med, intended to probe 50 GeV $< \Delta m <$ 80 GeV.

There are a number of differences between the event selection criteria for the 2 signal regions, all of which are presented in Table 5.3 for convenience. For bCa_med there is a requirement for ≥ 3 jets to suppress the SM W+jets background, wile for bCa_low this is lowered to ≥ 2 to avoid large acceptance losses. m_{eff} is defined by

$$m_{eff} = H_T + p_T^l + E_T^{\text{miss}} \tag{5.1}$$

where H_T is the scalar p_T sum of the four leading jets and p_T^l is the p_T of the single charged lepton in the event. Assuming the lepton mass is negligible, the transverse mass (m_T) is defined

	bCa_low	**bCa_med**
Lepton	7 GeV $p_T^{\text{electron}} < 25$ GeV 6 GeV $p_T^{\text{muon}} < 25$ GeV	
Jets	≥ 2 with $p_T > 180, 25$ GeV	≥ 3 with $p_T > 180, 25, 25$ GeV
b-tagging	≥ 1 sub-leading jet b-tagged (70% eff.)	
b-veto	1^{st} jet not b-tagged (70% eff.)	
$\mathbf{E_T^{miss}}$	> 370 GeV	> 300 GeV
$\mathbf{E_T^{miss}/m_{eff}}$	> 0.35	> 0.3
$\mathbf{m_T}$	> 90 GeV	> 100 GeV

Table 5.3: *Analysis cuts for the monojet with 1-lepton search in the $\tilde{t} \to bff'\tilde{\chi}_1^0$ channel. There are 2 separate signal regions, bCa_low and bCa_med.*

by,

$$m_T = \sqrt{2.p_T^l.E_T^{\text{miss}}\left(1 - \cos\Delta\phi(\vec{l}, \vec{p}_T^{\text{miss}})\right)}. \tag{5.2}$$

Here $\Delta\phi(\vec{l}, \vec{p}_T^{\text{miss}})$ is the azimuthal angle between the lepton momentum and the $\vec{p}_T^{\text{miss}}$ directions.

This is the analysis which ATLAS deemed computationally too expensive to produce the full matrix element for the SUSY signal sample, instead using Pythia which decays the $\tilde{t}_1$ isotropically. This limits the analysis to $\Delta m < 80$ GeV and fails to rule out the region we're interested in. Without flavour violation, the assumption of a 100% branching ratio to $\tilde{t} \to bff'\tilde{\chi}_1^0$ is correct for most of parameter space when $\Delta m > 80$, and it would be particularly useful to extend this analysis into this space.

We used MadGraph5 to produce the signal events. This was impossible to do accurately until November 2014, due to a bug in MadGraph which was fixed between Version-2.2.1 and Version-2.2.2. For small $\Delta m \lesssim 80$ GeV, the bug resulted in MadGraph incorrectly including many of the soft jets from stop decays in the matching scheme, with the result of a large proportion of the events being incorrectly vetoed, giving cross sections far smaller than their correct values. Once this bug was fixed, the generation of events was computationally intensive but achievable. Jet matching was required due to the added complication in this region that after selection cuts, the leading jet is sometimes from the decay products rather than being initial state radiation (ISR), which in the absence of matching leads to an infrared divergence of the ISR. Again the PDF used was CTEQ6L1 PDF, with Pythia-6, Delphes-3 and ROOT used for the rest of the signal generation and analysis. Each point in the $m_{\tilde{t}}$ vs $m_{\tilde{\chi}_1^0}$ plane was ruled out if for any of the signal regions (bCa_low, bCa_med) we predicted a larger number of signal events than the 95% CL upper limit on BSM events provided by ATLAS.

5.5 Results for Individual Channels

5.5.1 2-body, $\tilde{t} \to \tilde{\chi}_1^0 c$ Results

Monojet Analysis

Our result for the monojet analysis is presented in Figure 5.3, where the green region is the region we have ruled out at the 95% CL. ATLAS only presents their result after combining this exclusion region with that of the monojet with c-tagging search, with their combined exclusion being a salmon pink colour in Figure 5.2(a). This is done because this combination gives the entire region ruled out given the assumption that $\tilde{t} \to \tilde{\chi}_1^0 c$ is the only decay channel. It is this region's outline that is given by the red dashed line in Figure 5.3. Our monojet result reproduces the wedge shape seen in the ATLAS exclusion near $m_{\tilde{t}} = m_{\tilde{\chi}^0} \approx 270$ GeV. We also see that for $m_{\tilde{t}} \lesssim 170$ GeV, our exclusion extends outside the $\Delta m < 80$ GeV region, and therefore rules out a new region which is not covered by the ATLAS analyses. If we assume that the decay is entirely via $\tilde{t} \to \tilde{\chi}_1^0 c$, this monojet analysis alone rules out any stops with $m_t < 150$ GeV.

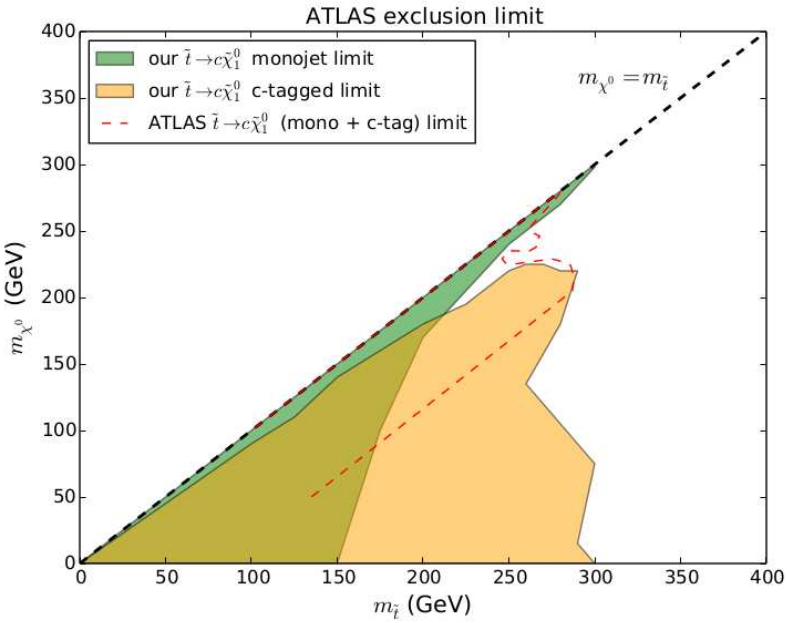

Figure 5.3: *The green region denotes the region excluded by the monojet analysis while the orange region is excluded by th monojet with c-tagging analysis. For both the exclusion is at a 95% CL assuming a 100% branching ratio to $\tilde{t} \to \tilde{\chi}_1^0 c$. The dashed red line is an outline of the region excluded by ATLAS after they conducted and combined the same two analyses.*

Monojet with c-tagging Analysis

Our result for the 95% exclusion region for the monojet with c-tagging analysis is denoted by the orange region in Figure 5.3.

Firstly, we see that we have successfully recreated the "bulge" in the ATLAS results, where 40 GeV $< \Delta m <$ 80 GeV and $m_{\tilde{t}} \approx 270$ GeV. When this is combined with the green monojet exclusion, we find that other than a small wedge when $m_{\tilde{t}} \approx 240$ GeV, $m_{\tilde{\chi}^0} \approx 210$ GeV, we agree well with ATLAS for the masses for which they have produced results, as we should expect. This agreement validates ours signal sample generation and analysis.

Secondly, our 95% CL extend well beyond the region excluded by ATLAS, all the way down to massless neutralinos. This means that if the assumption that $\tilde{t} \to \tilde{\chi}_1^0 c$ has a BR of 100% were true, light stops are ruled out for $m_{\tilde{t}} < 210$ GeV regardless of neutralino mass. However as discussed in section 5.2.1, this decay is only favoured when $\Delta m < 20$ GeV, and although it can occur at least up to $\Delta m \approx 110$ GeV, and assumption of a 100% BR over the entire region is very unlikely to be correct.

5.5.2 4-body, $\tilde{t} \to bff'\tilde{\chi}_1^0$ Results

Monojet with 1 lepton Analysis

The results of this analysis is presented separately to the monojet and monojet with charm tagging results as the assumed decay process is different. In Figure 5.4, we show our 95% CL excluded region, compared to the analogous ATLAS result outlined in dashed black. Also included on the plot is another ATLAS analysis which we have not reproduced, which is outlined in dashed blue. This is included to make it visually clear which region we particularly intended to rule out; the region *between* the two ATLAS exclusions.

Our exclusion region once more agrees reasonably well with ATLAS for $\Delta m < 80$ GeV, acting as a validation for our methods. However it also extends beyond this bound filling the previously unexcluded gap between the two ATLAS analyses, where Δm is slightly larger than M_W. Therefore, under the assumption that stops only have a 4-body decay, we have successfully ruled out a large part of the remaining phase space for light stops with masses of around 150 GeV $< m_{\tilde{t}} <$ 200 GeV. As discussed in 5.2.2, if we disallow flavour violation in the MSSM, then stops exclusively decaying to 4-body is a reasonable assumption. More generally however 2-body decays can also occur in this mass range.

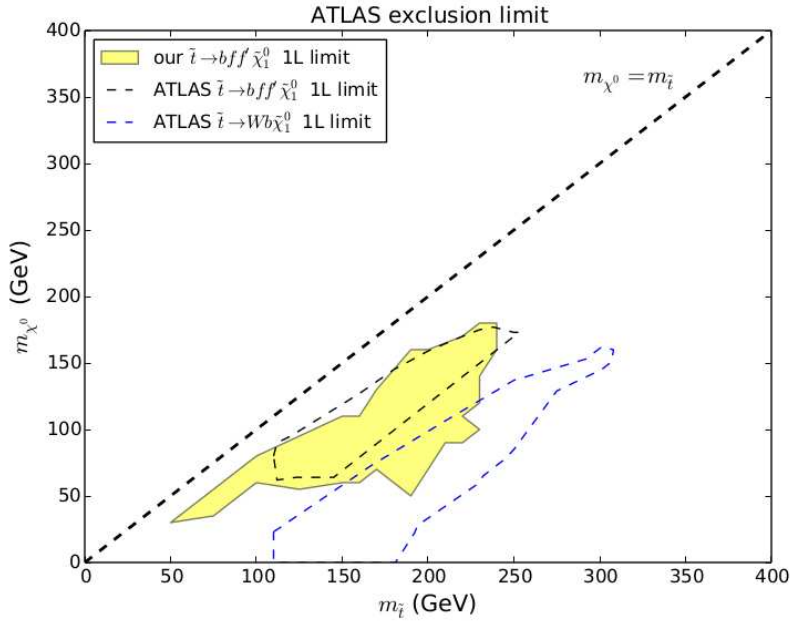

Figure 5.4: *The yellow area is excluded at a 95% CL by the monojet with 1-lepton analysis, assuming a 100% branching ratio to $\tilde{t} \to bff'\tilde{\chi}_1^0$. The dashed black line is an outline of the region excluded by ATLAS for the same analysis. The region inside the dashed blue line is excluded by a different ATLAS analysis which also assumes a $\tilde{t} \to bff'\tilde{\chi}_1^0$ decay.*

5.6 Results for Combined Analysis

In this section, we combine our results with those of ATLAS, including ATLAS analyses which we did not reproduce, to see the full region in the $m_{\tilde{t}}$ vs $m_{\tilde{\chi}_1^0}$ plane which is now excluded. As previously, it is sensible to consider the two decay channels separately which we do below.

5.6.1 2-body, $\tilde{t} \to \tilde{\chi}_1^0 c$ Combined Results

As we reproduced all of the ATLAS analyses which assume a $\tilde{t} \to \tilde{\chi}_1^0 c$ decay, combining our results with that of ATLAS only excludes an additional small wedge shaped region around $m_{\tilde{t}} \approx 240$, $m_{\tilde{\chi}^0} \approx 210$. These combined results are shown in Figure 5.5.

Our conclusion here is very similar to that prior to combining our results with ATLAS, but with the lower bound on the stop mass increased to around 240 GeV. If true, as having $m_{\tilde{t}} < m_t$ is a necessary condition for the light stop scenario of EW baryogenesis, this scenario would have been ruled out, but as this decay is disfavoured for moderate and large values of Δm this conclusion is invalid more generally.

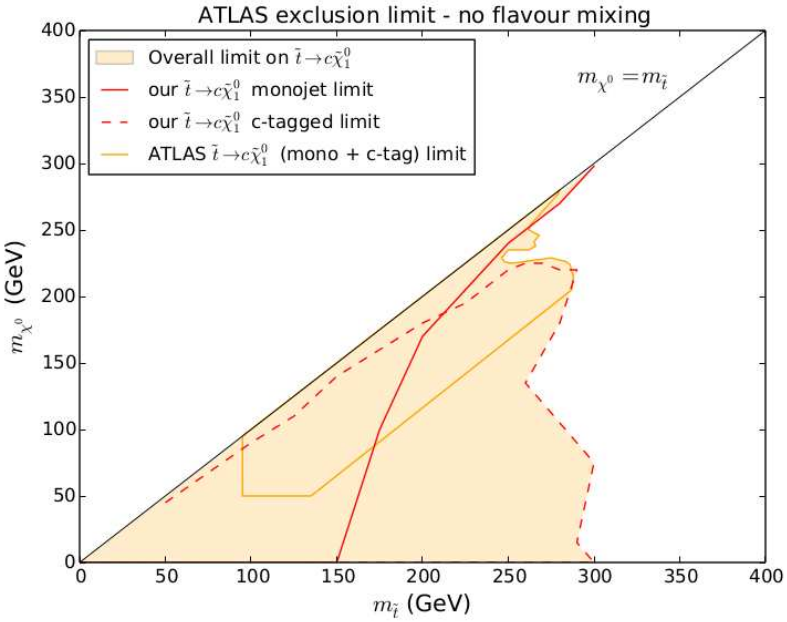

Figure 5.5: *The area shaded yellow in the $m_{\tilde{t}}$ vs $m_{\tilde{\chi}^0}$ plane has been excluded at the 95% CL after both our results and ATLAS results are included. The red outlines show regions excluded by our analysis (solid: monojet analysis, dashed: monojet with c-tagging analysis). The solid orange line outlines the region excluded by ATLAS.*

5.6.2 Four Body, $\tilde{t} \to bff'\tilde{\chi}_1^0$ Combined Results

In Figure 5.6 we combine our results for the monojet with one lepton analysis with all of the ATLAS analyses which assume the same $bff'\tilde{\chi}_1^0$ final state. The total area excluded at the 95% CL is shaded in blue. The outline of our contribution to the total exclusion area has a solid blue line, while all of the ATLAS exclusion results are outlined in purple. The only exception is another ATLAS study which is based on top-antitop spin correlations, whose outline is green.

The goal of the study was to rule out as much of the region with light stops as possible, in particular where Δm is slightly larger than M_W as this is where extending the ATLAS 95% CL was most likely to be successful. Inspection of Figure 5.6 shows that the addition of our analysis to ATLAS's results has achieved this, closing much of this remaining region and bridging the gap between ATLAS's $\tilde{t} \to bff'\tilde{\chi}_1^0$ analyses (where $\Delta m < 80$ GeV) and $\tilde{t} \to bW\tilde{\chi}_1^0$ analyses (where $\Delta m > 80$ GeV).

However, there still remains a small area where 110 GeV $\lesssim m_{\tilde{t}} \lesssim$ 140 GeV and 25 GeV $\lesssim m_{\tilde{\chi}^0} \lesssim$ 50 GeV where light stops are still allowed, as well as a narrow band along the $\Delta m \approx m_t$ line, and a small region where 191 GeV $< m_{\tilde{t}} \lesssim 205$ GeV near where the neutralino is massless. Therefore even with the assumption of a 4-body decay BR of 100% there remains a small region where light stop EWBG is still viable. Furthermore as discussed previously, this

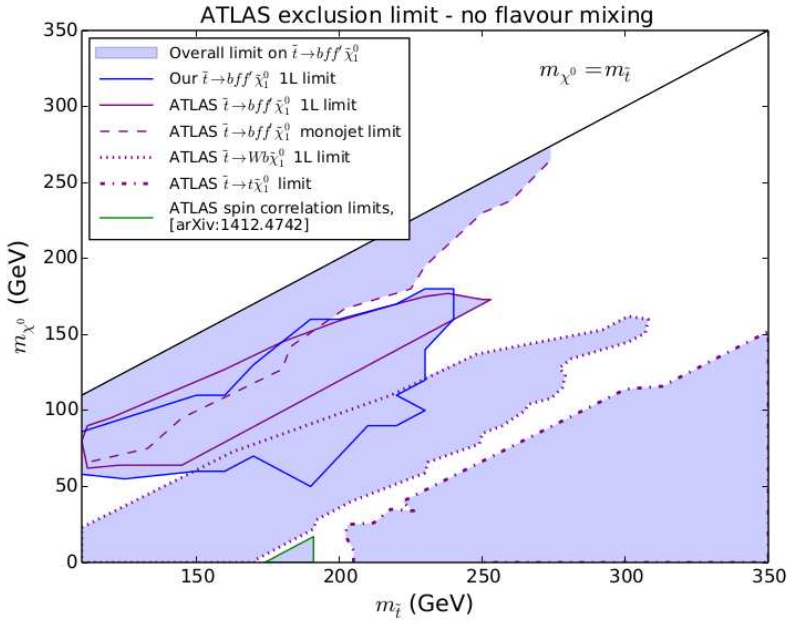

Figure 5.6: *Area in the $m_{\tilde{t}}$ vs $m_{\tilde{\chi}^0}$ plane which has been excluded at the 95% CL after combining our results with ATLAS. Blue outline - excluded by our monojet with lepton search. Purple outlines - regions excluded by ATLAS searches. Green outline - Excluded by ATLAS search via top-antitop spin correlations.*

assumption of exclusively 4-body decays is not valid as 2-body decays are able to occur for Δm at least up to 110 GeV when FV is allowed.

There are ongoing efforts to reduce the region where $\Delta m \approx m_t$ further. These include spin correlation approaches[176], and methods where the stop manifests as a disagreement between the theoretical and experimental values of the top cross section[177].

5.7 Intermediate values for the branching ratios

Thus far all the results presented assume a 100% branching fraction, either decaying via $\tilde{t} \to \tilde{\chi}_1^0 c$ or $\tilde{t} \to bff'\tilde{\chi}_1^0$. In this section we allow intermediate values of these results, assuming that these are the only two decay channels such that their branching ratios add to 100%.

The procedure followed was a simple procedure of adjusting the cross section and therefore the number of predicted signal events, according to the branching ratios. A point in the mass plane is excluded if the number of signal events in either channel was predicted to be larger than the 95% confidence limits (CL) upper limit on BSM events provided by ATLAS. This naive method is likely to be more pessimistic than a more sophisticated likelihood contour method. Furthermore, to produce these results, we have also assumed that any event with a mixed decay, i.e. where the two stops which are pair-produced decay to one of each of the two different

final states, will not pass the selection cuts. This assumption is also unlikely to be true for every mixed event, and therefore the exclusion regions presented here should be considered a *minimum* exclusion region.

These results are shown in the plots in Figure 5.7 where the branching ratio (BR) of the 2-body decay $\tilde{t} \to \tilde{\chi}_1^0 c$ is given above each plot, with the remaining BR being due to $\tilde{t} \to bff'\tilde{\chi}_1^0$. Starting from the top left and working right and down, the BRs to $\tilde{t} \to \tilde{\chi}_1^0 c$ considered are 100%, 80%, 50%, 30%, 20%, 10%, 5% and 0%. We can see that when the 2-body branching fraction is between about 10%–50%, neither decay is able to exclude our main region of interest where $\Delta m \approx M_W$ between the two ATLAS results. This occurs mainly because the $\tilde{t} \to bff'\tilde{\chi}_1^0$ exclusion region shrinks rapidly as the cross section of this decay channel drops, requiring a BR $> 90\%$ before its 95% CL extends beyond the $\Delta m = 80$ GeV line. As any combination of branching ratios is possible when $\Delta m \approx M_W$, these plots confirm that we cannot fully exclude these stop masses for every realisation of the MSSM.

5.8 Conclusion and Outlook

The goal of this study was to reproduce and extend the ATLAS light stop searches, having noticed that some of their studies had limitations in SUSY signal sample production and analysis, rather than direct limitations from the LHC experiment. In particular, we wanted to rule out as much of the parameter space which allows light stops as possible, with our main focus on the region where $\Delta m \approx M_W$. This is relevant to Higgs signal strength ratios discussed in Chapter 4, reducing the maximum possible contribution of light stops to $\frac{\mu_{VBF}}{\mu_{ggF}} > 1$, and could rule out the light stop scenario for baryogenesis.

Assuming a 100% branching fraction of $\tilde{t} \to \tilde{\chi}_1^0 c$, we agreed well with ATLAS in the region where they had produced results, validating our signal sample production and analysis code. However we also extended the exclusion well beyond the Δm region, successfully ruling out any $m_{\tilde{t}} < 240$ GeV when our results are included alongside that of ATLAS. These would be quite impressive results, although we also discussed that it is not valid to assume a 100% BR of $\tilde{t} \to \tilde{\chi}_1^0 c$ over most of the $m_{\tilde{t}}$ vs $m_{\tilde{\chi}^0}$ plane.

When instead we assume that the stop only decays via $\tilde{t} \to bff'\tilde{\chi}_1^0$, our results again agree well with the ATLAS exclusion limits where they have produced results. We also extend these results, bridging an important gap between two ATLAS analyses where $\Delta m \approx M_W$, although a small region where $m_{\tilde{t}} \approx 120$ GeV with $m_{\tilde{\chi}^0} \approx 40$ GeV remains unexcluded. Therefore we have limited the values of $m_{\tilde{t}}$ and reduced the amount of parameter space remaining where light stop electroweak baryogenesis is still viable, but it is not ruled out entirely.

In addition, we also considered intermediate values for the branching ratios, and found

that if the branching fraction to charm and neutralino is between 10%–50%, then our new exclusion limits are much reduced and do not extend beyond $\Delta m > 80$ GeV. In this region, the decay is most likely to be $\tilde{t} \to bff'\tilde{\chi}_1^0$ in a model with no flavour violation, but more generally any value of BR is possible, and so the most general exclusions limits are much weaker.

To understand the limits on stop masses in the most general scenario, a full simulation allowing for any intermediate branching ratios of the 2-body and 4-body decays is required, which would go beyond the naive calculations used for the intermediate branching ratio results presented in this chapter. A further complication which we have ignored, but needs to be considered for full generality is allowing for light charginos entering the decay chains. In this study we have made the assumption that this chargino is too heavy to be important. However when the LSP neutralino is Higgsino like, the chargino mass is almost degenerate with it, and to be as general as possible we should allow for the role this chargino may play in the decay process. We are currently working on extending this study taking both of these into account.

In summary we have successfully extended the ATLAS stop exclusion bounds, which reduces the parameter space where light stop EWBG can take place, and further limits the effect of light stops on Higgs physics. However, light stops are still not entirely ruled out, and there remains a small region of parameter space where light stop baryogenesis is still viable.

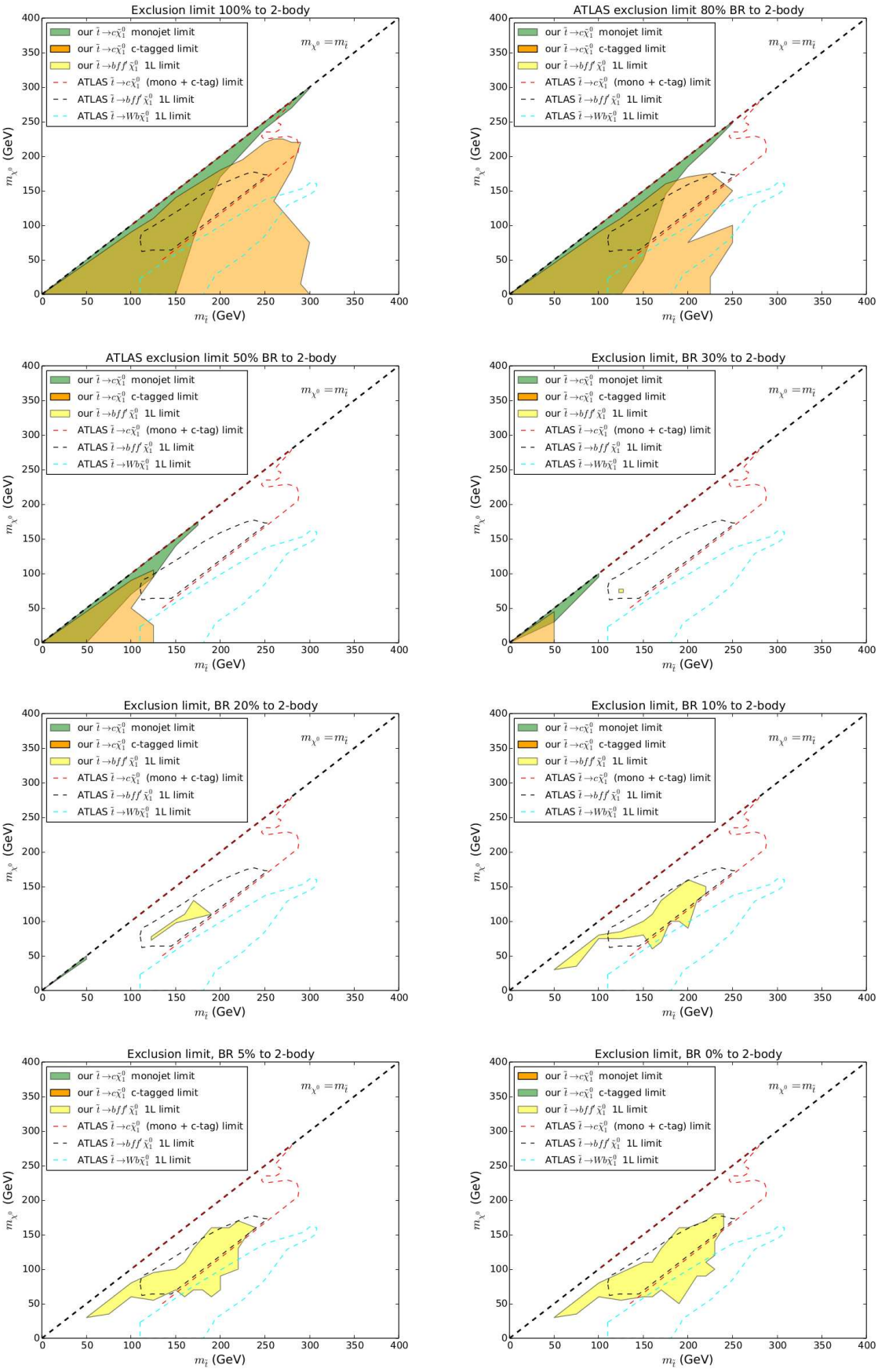

Figure 5.7: *Excluded region assuming a certain branching ratio to the 2-body decay $\tilde{t} \to \tilde{\chi}_1^0 c$. The rest of the branching ratio is to $\tilde{t} \to bff'\tilde{\chi}_1^0$. Starting from the top left and working right and down, the BRs to $\tilde{t} \to \tilde{\chi}_1^0 c$ are 100%, 80%, 50%, 30%, 20%, 10%, 5% and 0%. ATLAS exclusion regions are shown by dotted lines.*

Chapter 6

Conclusion

As discussed in the introduction, despite the standard model's success, there are many experimental observations and theoretical considerations which require BSM physics. With the Higgs discovery in 2012 and the LHC restarting at a higher energy of 13 TeV in spring 2015, there is a real possibility of finding signs of BSM physics at the LHC in the near future. The main purpose of my phenomenological research has been to study the effects of BSM physics on phenomena which are or may be observable at the LHC, so that results can be interpreted in terms of these BSM settings. The number of BSM theories is vast, and so in this thesis I have concentrated on theories which are likely to be observable at LHC energies if they are realised in nature.

Of the SM particles, a candidate for the most likely to show observable signs of BSM physics is the Higgs boson. Not only does it currently have large errors on the measurements of its couplings, but also these measurement will be greatly improved in the next 2-3 years, meaning that moderate deviations from SM predictions would be likely to be discovered soon. It can also be considered a more "special" particle than many of the others, being the only scalar in the standard model, the source of the hierarchy problem, and coupling to any BSM particles which gain their mass via the Higgs mechanism. It is also intimately linked to electroweak symmetry breaking (EWSB), and unitarises the scattering of longitudinally polarised vector bosons, who get their masses from the Goldstone bosons which arise during EWSB.

For these reasons, in Chapter 2, we used an effective field theory which is valid for many composite Higgs models to study the effect of non-SM couplings between the Higgs and vector bosons on scattering cross sections for processes involving the Higgs and longitudinally polarised weak bosons. We concentrated on high multiplicity processes (3 or 4 particles in the final state) as we'd noted that without the cancellations required to restore unitarity, the larger phase space in these processes causes a much more rapid scaling of cross section with collision energy. We found that these large increases in cross section do occur as expected, even for small ($\sim 10\%$)

deviations, with 3 particles in the final state generally being optimal at LHC energies because larger multiplicities had total cross sections that were too small despite the large increases. To see if this could be observed at the LHC, we studied the effects on total unpolarised cross sections and found that despite up to $\mathcal{O}(10^4$–$10^5)$ increases in cross section, the effects are masked by a combination of very low cross sections for the longitudinally polarised scattering and the large transverse component (*transverse pollution*).

Chapter 3 naturally followed on from this. Here we concentrated on the simplest relevant scattering, $V_LV_L \to V_LV_L$, (V_L's, $V = W^{\pm}, Z$), and devise a series of cuts on observables which reduce this *transverse pollution* to enable a more accurate analysis of longitudinal scattering. We also found that by fitting the distribution of θ^*, an angle between the momentum of a fermion which is a decay product of the vector boson, and the direction of boost to the boson's rest frame, we were able to directly measure the fraction which were longitudinally or transversely polarised. As well as enabling us to measure the effect of other cuts on polarisation, this would enable us to directly measure the hVV coupling as it is correlated with the longitudinal fraction. A preliminary analysis showed that this would allow us to measure the coupling to around 10% accuracy with 100 fb^{-1} of data at 13 TeV at the LHC, improving to 2.5% with 1.5 ab^{-1}.

In Chapter 4 we considered how the Higgs couplings would be affected by another BSM model, namely supersymmetry. There are a number of reasons to expect that SUSY is a symmetry of nature, and the gauge hierarchy problem leads us to expect that it would be realised at around the TeV scale (or less). Also, the main Higgs production via gluon fusion, and one of its easiest decays to observe, to di-photon, are via loops, which MSSM particles can enter and alter. Furthermore, due to their larger Yukawa couplings we would expect the 3$^{\text{rd}}$ generation quarks and lepton to be lighter than the 1$^{\text{st}}$ and 2$^{\text{nd}}$ and hence we studied the effects of light stops, sbottoms and staus, as well as SUSY corrections to the main Higgs decay, $h \to b\bar{b}$, via the Y_b coupling. Our results showed that for most of the parameter space, light stops or sbottoms produce a non-universal alteration of the signal strength with regards to production, with in general the signal strength via VBF production, μ_{VBF}, being larger than for gluon fusion production, μ_{ggF}, (i.e. $\frac{\mu_{VBF}}{\mu_{ggF}} > 1$). A chi-squared test showed that all 3 of these scenarios fitted data better than the SM.

Finally in Chapter 5 we looked at excluding light stops. Having noticed that some of the ATLAS exclusions in the region of light stops was limited by difficulties in generating SUSY signal samples and in analysis, we aimed to overcome these difficulties to extend these excluded regions. In particular we wanted to increase the minimum allowed mass of the stop to see if we could reduce the maximum possible effects of light stops on $\frac{\mu_{VBF}}{\mu_{ggF}}$ as discussed in Chapter 4, and limit the available parameter space for the light stop scenario of electroweak baryogenesis

(EWBG). We found that if we assume a 100% branching ratio of $\tilde{t} \to \tilde{\chi}_1^0 c$ then we drastically extend the original ATLAS exclusion, ruling out $m_{\tilde{t}} < 240$ GeV regardless of $m_{\tilde{\chi}^0}$. In this case EWBG would be ruled out. If on the other hand we assume the more realistic scenario that the decay is only via $\tilde{t} \to bff'\tilde{\chi}_1^0$, we successfully extend the analysis, ruling out much of the remaining low stop mass region, in particular near the $\Delta m = m_{\tilde{t}} - m_{\tilde{\chi}^0} \approx m_W$ line. Furthermore we show that intermediate branching ratios, with a branching fraction to charm and neutralino between 10%–50% would remove these new exclusions.

Producing the work presented in this thesis has opened up many interesting new avenues of study, and much of my current and future research follows on directly from the work which has been discussed. The loss of unitarity discussed in Chapter 2 becomes more acute as the collision energy increases, and so with the recently discussed possibility of building a 100 TeV collider, we are currently extending this study up to this energy regime[55]. In addition, the exciting prospect of using vector boson scattering to measure the Higgs coupling to weak bosons discussed in Chapter 3 is also worthy of further study, and we have ongoing work to combine all the relevant scattering channels and optimise cuts to improve the projected accuracy further. Finally, we are extending the work in Chapter 5, both by allowing for light charginos in the decay chain, and by producing a more realistic simulation of events with intermediate branching ratios, as this will allow the stop exclusion limits for any combination of branching fractions to be calculated more accurately.

Overall, in this thesis I have considered the phenomenology of BSM physics at the LHC, assessing the effect of a composite Higgs scenario or supersymmetry on the Higgs boson, as well as extending the exclusion limits on light stops. I have found that these models predict effects which could be visible at the LHC or other future colliders. The standard model has been the standard paradigm for particle physics since the 1970s. With the LHC increasing its energy and run 2 starting this spring, the next few years will be an exciting time for the collider community. Hopefully beyond standard model physics will be found, ushering in a new era for particle physics.

Appendices

Appendix A

Proof of Unitarity Bound

In this appendix, we derive the upper bound on the inelastic $2 \to n$ scattering cross section given in Equation 2.1, largely reproducing the derivation in [41]. From the unitarity of the S matrix, $S^\dagger S = 1$, writing $S = 1 + iT$ we obtain

$$T^\dagger T = 2\Im(T). \tag{A.1}$$

Take the matrix element of this equation between identical initial and final two-body states. Insert a complete set of intermediate states into the left-hand side of this equation, separating out explicitly the intermediate state which is identical to the initial and final states, to get

$$\int dPS_2 |T_{el}(2 \to 2)|^2 + \sum_n \int dPS_n |T_{inel}(2 \to n)|^2 = 2\Im\left(T_{el}(2 \to 2)\right), \tag{A.2}$$

where dPS_n indicates n-body phase space and the sum is over all inelastic intermediate states. Define the J^{th} partial-wave $2 \to 2$ elastic amplitude

$$a_J = \frac{1}{32\pi} \int_{-1}^{1} dz P_J(z) T_{el}(2 \to 2), \tag{A.3}$$

where z is the cosine of the scattering angle, to get

$$\sum_J |a_J|^2 + \frac{1}{32\pi} \sum_n \int dPS_n |T_{inel}(2 \to n)|^2 = \sum_J \Im(a_J). \tag{A.4}$$

Using $|a_J|^2 = \Re(a_J)^2 + \Im(a_J)^2$ yields

$$\sum_J \Re(a_J)^2 + \frac{1}{32\pi} \sum_n \int dPS_n |T_{inel}(2 \to n)|^2 = \sum_J \Im\left(a_J(1 - \Im(a_J))\right). \tag{A.5}$$

If the elastic amplitude is dominated by a single partial wave, one may remove the summation. The right-hand side is then bounded above by $\frac{1}{4}$, giving

$$\int dPS_n |T_{inel}(2 \to n)|^2 \leq 8\pi, \tag{A.6}$$

for all n. This implies the desired upper bound,

$$\sigma_{inel}(2 \to n) \leq \frac{4\pi}{s}. \tag{A.7}$$

If there is more than one n-body intermediate state, then the bound applies to the sum of the cross section for each intermediate state.

Appendix B

Loop functions

The loop functions used in this thesis are;

$$F_1(x) = -x^2\left[\frac{2}{x^2}+\frac{3}{x}+3\left(\frac{2}{x}-1\right)\arcsin^2\sqrt{\frac{1}{x}}\right] \tag{B.1}$$

$$F_{1/2}(x) = 2x^2\left[\frac{1}{x}+\left(\frac{1}{x}-1\right)\arcsin^2\sqrt{\frac{1}{x}}\right] \tag{B.2}$$

$$F_0(x) = -x^2\left[\frac{1}{x}-\arcsin^2\sqrt{\frac{1}{x}}\right]. \tag{B.3}$$

Bibliography

[1]M. L. Perl, G. Abrams, A. Boyarski, M. Breidenbach, D. Briggs, et al., "Evidence for Anomalous Lepton Production in e+ - e- Annihilation", Phys.Rev.Lett. **35**, 1489–1492 (1975).

[2]J. Aubert et al., "Experimental Observation of a Heavy Particle J", Phys.Rev.Lett. **33**, 1404–1406 (1974).

[3]J. Augustin et al., "Discovery of a Narrow Resonance in e+ e- Annihilation", Phys.Rev.Lett. **33**, 1406–1408 (1974).

[4]S. Herb, D. Hom, L. Lederman, J. Sens, H. Snyder, et al., "Observation of a Dimuon Resonance at 9.5-GeV in 400-GeV Proton-Nucleus Collisions", Phys.Rev.Lett. **39**, 252–255 (1977).

[5]M. Banner et al., "Observation of Single Isolated Electrons of High Transverse Momentum in Events with Missing Transverse Energy at the CERN anti-p p Collider", Phys.Lett. **B122**, 476–485 (1983).

[6]G. Arnison et al., "Experimental Observation of Isolated Large Transverse Energy Electrons with Associated Missing Energy at s**(1/2) = 540-GeV", Phys.Lett. **B122**, 103–116 (1983).

[7]G. Arnison et al., "Experimental Observation of Lepton Pairs of Invariant Mass Around 95-GeV/c**2 at the CERN SPS Collider", Phys.Lett. **B126**, 398–410 (1983).

[8]V. Abazov et al., "Observation of Single Top Quark Production", Phys.Rev.Lett. **103**, 092001 (2009).

[9]K. Kodama et al., "Observation of tau neutrino interactions", Phys.Lett. **B504**, 218–224 (2001).

[10]G. Aad et al., "Observation of a new particle in the search for the Standard Model Higgs boson with the ATLAS detector at the LHC", Phys.Lett. **B716**, 1–29 (2012).

[11]S. Chatrchyan et al., "Observation of a new boson at a mass of 125 GeV with the CMS experiment at the LHC", Phys.Lett. **B716**, 30–61 (2012).

[12]G. Gabrielse, D. Hanneke, T. Kinoshita, M. Nio, and B. C. Odom, "New Determination of the Fine Structure Constant from the Electron g Value and QED", Phys.Rev.Lett. **97**, Erratum-ibid. 99 (2007) 039902, 030802 (2006).

[13]P. Clade, E. de Mirandes, M. Cadoret, S. Guellati-Khelifa, C. Schwob, et al., "Determination of the Fine Structure Constant Based on Bloch Oscillations of Ultracold Atoms in a Vertical Optical Lattice", Phys.Rev.Lett. **96**, 033001 (2006).

[14]L. Canetti, M. Drewes, and M. Shaposhnikov, "Matter and Antimatter in the Universe", New J.Phys. **14**, 095012 (2012).

[15]M. R. Lovell, V. Eke, C. S. Frenk, L. Gao, A. Jenkins, et al., "The Haloes of Bright Satellite Galaxies in a Warm Dark Matter Universe", Mon.Not.Roy.Astron.Soc. **420**, 2318–2324 (2012).

[16]C. Baker, D. Doyle, P. Geltenbort, K. Green, M. van der Grinten, et al., "An Improved experimental limit on the electric dipole moment of the neutron", Phys.Rev.Lett. **97**, 131801 (2006).

[17]S. R. Coleman and J. Mandula, "All Possible Symmetries of the S Matrix", Phys.Rev. **159**, 1251–1256 (1967).

[18]R. Haag, J. T. Lopuszanski, and M. Sohnius, "All Possible Generators of Supersymmetries of the s Matrix", Nucl.Phys. **B88**, 257 (1975).

[19]J. B. *et al.*, "Particle data group", Phys. Rev. **D86**, 010001 (2012).

[20]G. Bennett et al., "Measurement of the positive muon anomalous magnetic moment to 0.7 ppm", Phys.Rev.Lett. **89**, 101804 (2002).

[21]G. Bennett et al., "Measurement of the negative muon anomalous magnetic moment to 0.7 ppm", Phys.Rev.Lett. **92**, 161802 (2004).

[22]G. Bennett et al., "Final Report of the Muon E821 Anomalous Magnetic Moment Measurement at BNL", Phys.Rev. **D73**, 072003 (2006).

[23]P. J. Mohr, B. N. Taylor, and D. B. Newell, "CODATA Recommended Values of the Fundamental Physical Constants: 2010", Rev.Mod.Phys. **84**, 1527–1605 (2012).

[24]A. Czarnecki and W. J. Marciano, "The Muon anomalous magnetic moment: A Harbinger for 'new physics'", Phys.Rev. **D64**, 013014 (2001).

[25]A. Djouadi, "The Anatomy of electro-weak symmetry breaking. II. The Higgs bosons in the minimal supersymmetric model", Phys.Rept. **459**, 1–241 (2008).

[26]S. P. Martin, "A supersymmetry primer", hep-ph/9709356, 1997.

[27]"Updated coupling measurements of the Higgs boson with the ATLAS detector using up to 25 fb^{-1} of proton-proton collision data", ATLAS-CONF-2014-009, ATLAS-COM-CONF-2014-013 (2014).

[28]V. Khachatryan et al., "Precise determination of the mass of the Higgs boson and tests of compatibility of its couplings with the standard model predictions using proton collisions at 7 and 8 TeV", arXiv:1412.8662 (2014).

[29]G. Aad et al., "Search for $H \to \gamma\gamma$ produced in association with top quarks and constraints on the Yukawa coupling between the top quark and the Higgs boson using data taken at 7 TeV and 8 TeV with the ATLAS detector", Phys.Lett. **B740**, 222–242 (2015).

[30]A. Belyaev, A. Oliveira, R. Rosenfeld, and M. C. Thomas, "Multi Higgs and Vector boson production beyond the Standard Model", JHEP **1305**, 005 (2013).

[31]A. Belyaev, S. Khalil, S. Moretti, and M. C. Thomas, "Light sfermion interplay in the 125 GeV MSSM Higgs production and decay at the LHC", JHEP **1405**, 076 (2014).

[32]G. Brooijmans, R. Contino, B. Fuks, F. Moortgat, P. Richardson, et al., "Les Houches 2013: Physics at TeV Colliders: New Physics Working Group Report", (2014).

[33]S. Chatrchyan et al., "Study of the Mass and Spin-Parity of the Higgs Boson Candidate Via Its Decays to Z Boson Pairs", Phys.Rev.Lett. **110**, 081803 (2013).

[34]V. Khachatryan et al., "Constraints on the spin-parity and anomalous HVV couplings of the Higgs boson in proton collisions at 7 and 8 TeV", arXiv:1411.3441 (2014).

[35]G. Aad et al., "Evidence for the spin-0 nature of the Higgs boson using ATLAS data", Phys.Lett. **B726**, 120–144 (2013).

[36]A. Belyaev, M. S. Brown, R. Foadi, and M. T. Frandsen, "The Technicolor Higgs in the Light of LHC Data", Phys.Rev. **D90**, 035012 (2014).

[37]M. S. Chanowitz and M. K. Gaillard, "Multiple Production of W and Z as a Signal of New Strong Interactions", Phys.Lett. **B142**, 85 (1984).

[38]D. Morris, R. Peccei, and R. Rosenfeld, "Multiple W(L) production from inelastic W(L) W(L) scattering at s**(1/2) $\gg$ M(H)", Phys.Rev. **D47**, 3839–3848 (1993).

[39]U. Aydemir, M. M. Anber, and J. F. Donoghue, "Self-healing of unitarity in effective field theories and the onset of new physics", Phys.Rev. **D86**, 014025 (2012).

[40]D. A. Dicus and H.-J. He, "Scales of fermion mass generation and electroweak symmetry breaking", Phys.Rev. **D71**, 093009 (2005).

[41]F. Maltoni, J. Niczyporuk, and S. Willenbrock, "The Scale of fermion mass generation", Phys.Rev. **D65**, 033004 (2002).

[42]E. Byckling and K. Kajantie, *Particle kinematics* (John Wiley & Sons Ltd, 1973).

[43]G. Giudice, C. Grojean, A. Pomarol, and R. Rattazzi, "The Strongly-Interacting Light Higgs", JHEP **0706**, 045 (2007).

[44]R. Contino, C. Grojean, M. Moretti, F. Piccinini, and R. Rattazzi, "Strong Double Higgs Production at the LHC", JHEP **1005**, 089 (2010).

[45]R. Grober and M. Muhlleitner, "Composite Higgs Boson Pair Production at the LHC", JHEP **1106**, 020 (2011).

[46]K. Agashe, R. Contino, and A. Pomarol, "The Minimal composite Higgs model", Nucl.Phys. **B719**, 165–187 (2005).

[47]R. Contino, L. Da Rold, and A. Pomarol, "Light custodians in natural composite Higgs models", Phys.Rev. **D75**, 055014 (2007).

[48]R. Contino, D. Marzocca, D. Pappadopulo, and R. Rattazzi, "On the effect of resonances in composite Higgs phenomenology", JHEP **1110**, 081 (2011).

[49]T. Hahn and M. Perez-Victoria, "Automatized one loop calculations in four-dimensions and D-dimensions", Comput.Phys.Commun. **118**, 153–165 (1999).

[50]J. Alwall, M. Herquet, F. Maltoni, O. Mattelaer, and T. Stelzer, "MadGraph 5 : Going Beyond", JHEP **06**, 128 (2011).

[51]N. D. Christensen and C. Duhr, "FeynRules - Feynman rules made easy", Comput. Phys. Commun. **180**, 1614–1641 (2009).

[52]C. Degrande, C. Duhr, B. Fuks, D. Grellscheid, O. Mattelaer, et al., "UFO - The Universal FeynRules Output", Comput.Phys.Commun. **183**, 1201–1214 (2012).

[53]A. Belyaev, N. D. Christensen, and A. Pukhov, "CalcHEP 3.4 for collider physics within and beyond the Standard Model", Comput.Phys.Commun. **184**, 1729–1769 (2013).

[54]A. Semenov, "LanHEP - a package for the automatic generation of Feynman rules in field theory. Version 3.0", Comput. Phys. Commun. **180**, 431–454 (2009).

[55]A. Belyaev, P. Hamers, and M. Thomas, *Triple Higgs Production at a 100 TeV collider as a measurement of anomolous Higgs couplings t weak bosons*, **Upcoming**.

[56]H.-J. He et al., "LHC Signatures of New Gauge Bosons in Minimal Higgsless Model", Phys. Rev. **D78**, 031701 (2008).

[57]S. Dawson, "The Effective W Approximation", Nucl.Phys. **B249**, 42–60 (1985).

[58]M. S. Chanowitz and M. K. Gaillard, "The TeV Physics of Strongly Interacting W's and Z's", Nucl.Phys. **B261**, 379 (1985).

[59]P. Borel, R. Franceschini, R. Rattazzi, and A. Wulzer, "Probing the Scattering of Equivalent Electroweak Bosons", JHEP **1206**, 122 (2012).

[60]J. M. Cornwall, D. N. Levin, and G. Tiktopoulos, "Derivation of Gauge Invariance from High-Energy Unitarity Bounds on the s Matrix", Phys.Rev. **D10**, 1145 (1974).

[61]J. Bagger, V. D. Barger, K.-m. Cheung, J. F. Gunion, T. Han, et al., "The Strongly interacting W W system: Gold plated modes", Phys.Rev. **D49**, 1246–1264 (1994).

[62]J. Bagger, V. D. Barger, K.-m. Cheung, J. F. Gunion, T. Han, et al., "CERN LHC analysis of the strongly interacting W W system: Gold plated modes", Phys.Rev. **D52**, 3878–3889 (1995).

[63]J. Butterworth, B. Cox, and J. R. Forshaw, "WW scattering at the CERN LHC", Phys.Rev. **D65**, 096014 (2002).

[64] A. Belyaev, O. J. Eboli, M. Gonzalez-Garcia, J. Mizukoshi, S. Novaes, et al., "Strongly interacting vector bosons at the CERN LHC: Quartic anomalous couplings", Phys.Rev. **D59**, 015022 (1999).

[65] A. Ballestrero, G. Bevilacqua, and E. Maina, "A Complete parton level analysis of boson-boson scattering and ElectroWeak Symmetry Breaking in lv + four jets production at the LHC", JHEP **0905**, 015 (2009).

[66] T. Han, D. Krohn, L.-T. Wang, and W. Zhu, "New Physics Signals in Longitudinal Gauge Boson Scattering at the LHC", JHEP **1003**, 082 (2010).

[67] K. Doroba, J. Kalinowski, J. Kuczmarski, S. Pokorski, J. Rosiek, et al., "The $W_L W_L$ Scattering at the LHC: Improving the Selection Criteria", Phys.Rev. **D86**, 036011 (2012).

[68] Y. Cui and Z. Han, "New light on WW scattering at the LHC with W jet tagging", (2013).

[69] A. Freitas and J. Gainer, "High Energy WW Scattering at the LHC with the Matrix Element Method", Phys.Rev. **D88**, 017302 (2013).

[70] J. Chang, K. Cheung, C.-T. Lu, and T.-C. Yuan, "WW Scattering in the Era of Post Higgs Discovery", Phys.Rev. **D87**, 093005 (2013).

[71] R. Brun and F. Rademakers, "ROOT: An object oriented data analysis framework", Nucl.Instrum.Meth. **A389**, 81–86 (1997).

[72] "Combined coupling measurements of the Higgs-like boson with the ATLAS detector using up to 25 fb^{-1} of proton-proton collision data", ATLAS-CONF-2013-034, ATLAS-COM-CONF-2013-035 (2013).

[73] *Updated coupling measurements of the Higgs boson with the ATLAS detector using up to 25 fb^{-1} of proton-proton collision data*, tech. rep. ATLAS-CONF-2014-009 (CERN, Geneva, 2014).

[74] "Combination of standard model Higgs boson searches and measurements of the properties of the new boson with a mass near 125 GeV", CMS-PAS-HIG-13-005 (2013).

[75] *Precise determination of the mass of the Higgs boson and studies of the compatibility of its couplings with the standard model*, tech. rep. CMS-PAS-HIG-14-009 (CERN, Geneva, 2014).

[76] M. E. Chasco, "Search for invisible Higgs boson production with the CMS detector at the LHC", arXiv:1310.1002 (2013).

[77] J. Lee, A. Pilaftsis, M. S. Carena, S. Choi, M. Drees, et al., "CPsuperH: A Computational tool for Higgs phenomenology in the minimal supersymmetric standard model with explicit CP violation", Comput.Phys.Commun. **156**, 283–317 (2004).

[78] J. Lee, M. Carena, J. Ellis, A. Pilaftsis, and C. Wagner, "CPsuperH2.0: an Improved Computational Tool for Higgs Phenomenology in the MSSM with Explicit CP Violation", Comput.Phys.Commun. **180**, 312–331 (2009).

[79] M. Carena et al., "Report of the tevatron higgs working group", hep-ph/0010338 (2000).

[80] A. Arbey, M. Battaglia, A. Djouadi, and F. Mahmoudi, "An update of the constraints on the phenomenological MSSM from the new LHC Higgs results", Phys. Lett. **B720**, 153–160 (2013).

[81] P. Bechtle, S. Heinemeyer, O. Stå l, T. Stefaniak, G. Weiglein, and L. Zeune, "MSSM interpretations of the LHC discovery: light or heavy Higgs?", Eur. Phys. J. **C73**, 2354 (2013).

[82] K. Schmidt-Hoberg, F. Staub, and M. W. Winkler, "Enhanced diphoton rates at Fermi and the LHC", JHEP **2013**, 124 (2013).

[83] Z. Heng, "A 125 GeV Higgs and its di-photon signal in different SUSY models: a mini review", Adv. High Energy Phys. **2012**, 312719 (2012).

[84] M. Drees, "Supersymmetric explanation of the excess of Higgs-like events at the LHC and at LEP", Phys. Rev. **D86**, 115018 (2012).

[85] A. Arbey, M. Battaglia, A. Djouadi, and F. Mahmoudi, "The Higgs sector of the phenomenological MSSM in the light of the Higgs boson discovery", JHEP **2012**, 107 (2012).

[86]K. Schmidt-Hoberg and F. Staub, "Enhanced h $\gamma\gamma$ rate in MSSM singlet extensions", JHEP **2012**, 195 (2012).

[87]M. Carena, I. Low, and C. E. Wagner, "Implications of a Modified Higgs to Diphoton Decay Width", JHEP **1208**, 060 (2012).

[88]M. Carena, S. Gori, N. R. Shah, and C. E. M. Wagner, "A 125 GeV SM-like Higgs in the MSSM and the $\gamma\gamma$ rate", JHEP **2012**, 14 (2012).

[89]L. J. Hall, D. Pinner, and J. T. Ruderman, "A natural SUSY Higgs near 125 GeV", JHEP **2012**, 131 (2012).

[90]S. Heinemeyer, O. Stå l, and G. Weiglein, "Interpreting the LHC Higgs search results in the MSSM", Phys. Lett. **B710**, 201–206 (2012).

[91]A. Arbey, M. Battaglia, A. Djouadi, F. Mahmoudi, and J. Quevillon, "Implications of a 125 GeV Higgs for supersymmetric models", Phys. Lett. **B708**, 162–169 (2012).

[92]P. Draper, P. Meade, M. Reece, and D. Shih, "Implications of a 125 GeV Higgs boson for the MSSM and low-scale supersymmetry breaking", Phys. Rev. **D85**, 095007 (2012).

[93]N. Chen and H.-J. He, "LHC signatures of two-Higgs-doublets with fourth family", JHEP **2012**, 62 (2012).

[94]G. Guo, B. Ren, and X.-G. He, "LHC Evidence Of A 126 GeV Higgs Boson From $H \to \gamma\gamma$ With Three And Four Generations", arXiv:1112.3188 (2011).

[95]X.-G. He, B. Ren, and J. Tandean, "Hints of Standard Model Higgs Boson at the LHC and Light Dark Matter Searches", Phys.Rev. **D85**, 093019 (2012).

[96]A. Djouadi, O. Lebedev, Y. Mambrini, and J. Quevillon, "Implications of LHC searches for Higgs-portal dark matter", Phys. Lett. **B709**, 65–69 (2012).

[97]K. Cheung and T.-C. Yuan, "Could the Excess Seen at 124126 GeV Be due to the Randall-Sundrum Radion?", Phys. Rev. Lett. **108**, 141602 (2012).

[98]B. Batell, S. Gori, and L.-T. Wang, "Exploring the Higgs portal with 10 fb1 at the LHC", JHEP **2012**, 172 (2012).

[99]N. D. Christensen, T. Han, and S. Su, "MSSM Higgs Bosons at The LHC", Phys.Rev. **D85**, 115018 (2012).

[100]M. Kadastik, K. Kannike, A. Racioppi, and M. Raidal, "Implications of the 125 GeV Higgs boson for scalar dark matter and for the CMSSM phenomenology", JHEP **2012**, 61 (2012).

[101]H. Baer, V. Barger, and A. Mustafayev, "Implications of a 125 GeV Higgs scalar for the LHC supersymmetry and neutralino dark matter searches", Phys. Rev. **D85**, 075010 (2012).

[102]L. Aparicio, D. G. Cerdeño, and L. E. Ibáñez, "A 119-125 GeV Higgs from a string derived slice of the CMSSM", JHEP **2012**, 126 (2012).

[103]J. Ellis and K. A. Olive, "Revisiting the Higgs mass and dark matter in the CMSSM", Eur. Phys. J. **C72**, 2005 (2012).

[104]H. Baer, V. Barger, and A. Mustafayev, "Neutralino dark matter in mSUGRA/CMSSM with a 125 GeV light Higgs scalar", JHEP **2012**, 91 (2012).

[105]N. Desai, B. Mukhopadhyaya, and S. Niyogi, "Constraints on Invisible Higgs Decay in MSSM in the Light of Diphoton Rates from the LHC", arXiv:1202.5190 (2012).

[106]J. Cao, Z. Heng, D. Li, and J. M. Yang, "Current experimental constraints on the lightest Higgs boson mass in the constrained MSSM", Phys. Lett. **B710**, 665–670 (2012).

[107]S. King, M. Mühlleitner, R. Nevzorov, and K. Walz, "Natural NMSSM Higgs bosons", Nucl. Phys. **B870**, 323–352 (2013).

[108]J. F. Gunion, Y. Jiang, and S. Kraml, "Could two NMSSM Higgs bosons be present near 125 GeV?", Phys. Rev. **D86**, 071702 (2012).

[109]G. Bélanger, U. Ellwanger, J. F. Gunion, Y. Jiang, S. Kraml, and J. H. Schwarz, "Higgs bosons at 98 and 125 GeV at LEP and the LHC", JHEP **2013**, 69 (2013).

[110]J. F. Gunion, Y. Jiang, and S. Kraml, "The constrained NMSSM and Higgs near 125 GeV", Phys. Lett. **B710**, 454–459 (2012).

[111]U. Ellwanger and C. Hugonie, "Higgs Bosons Near 125 GeV in the NMSSM with Constraints at the GUT Scale", Adv.High Energy Phys. **2012**, 1–18 (2012).

[112]U. Ellwanger, "A Higgs boson near 125 GeV with enhanced di-photon signal in the NMSSM", JHEP **2012**, 44 (2012).

[113]J.-J. Cao, Z.-X. Heng, J. M. Yang, Y.-M. Zhang, and J.-Y. Zhu, "A SM-like Higgs near 125 GeV in low energy SUSY: a comparative study for MSSM and NMSSM", JHEP **1203**, 086 (2012).

[114]Z. Kang, J. Li, and T. Li, "On naturalness of the MSSM and NMSSM", JHEP **2012**, 24 (2012).

[115]A. Elsayed, S. Khalil, and S. Moretti, "Higgs mass corrections in the SUSY model with inverse seesaw", Phys. Lett. **B715**, 208–213 (2012).

[116]L. Basso and F. Staub, "Enhancing h$\gamma\gamma$ with staus in supersymmetric models with an extended gauge sector", Phys. Rev. **D87**, 015011 (2013).

[117]S. Khalil and S. Moretti, "Heavy neutrinos, Z' and Higgs bosons at the LHC: new particles from an old symmetry", J.Mod.Phys. **4**, 7–10 (2013).

[118]S. Khalil and S. Moretti, "A simple symmetry as a guide toward new physics beyond the Standard Model", Front. Physics **1**, 10 (2013).

[119]B. Batell, S. Jung, and C. E. M. Wagner, "Very Light Charginos and Higgs Decays", arXiv:1309.2297 (2013).

[120]M. Carena, S. Gori, N. R. Shah, C. E. Wagner, and L.-T. Wang, "Light Stau Phenomenology and the Higgs $\gamma\gamma$ Rate", JHEP **1207**, 175 (2012).

[121]T. Han, Z. Liu, and A. Natarajan, "Dark matter and Higgs bosons in the MSSM", JHEP **1311**, 008 (2013).

[122]J. R. Ellis, G Ridolfi, and F. Zwirner, "Radiative corrections to the masses of supersymmetric Higgs bosons", Phys. Lett. **B257**, 83–91 (1990).

[123]H. Haber and R. Hempfling, "Can the mass of the lightest Higgs boson of the minimal supersymmetric model be larger than m_{Z}?", Phys. Rev. Lett. **66**, 1815–1818 (1991).

[124]H. E. Haber, R. Hempfling, and A. H. Hoang, "Approximating the radiatively corrected Higgs mass in the minimal supersymmetric model", Z.Phys. **C75**, 539–554 (1997).

[125]Joint LEP2 Supersymmetry Working Group, *Combined LEP Selectron/Smuon/Stau Results, 183-208 GeV, http://lepsusy.web.cern.ch/lepsusy*, 2004.

[126]M. Drees, "A Supersymmetric explanation of the excess of Higgs-like events at LEP", Phys.Rev. **D71**, 115006 (2005).

[127]J. Frere, D. Jones, and S. Raby, "Fermion Masses and Induction of the Weak Scale by Supergravity", Nucl.Phys. **B222**, 11 (1983).

[128]M. Claudson, L. J. Hall, and I. Hinchliffe, "Low-Energy Supergravity: False Vacua and Vacuous Predictions", Nucl.Phys. **B228**, 501 (1983).

[129]J. Camargo-Molina, B. O'Leary, W. Porod, and F. Staub, "**Vevacious**: A Tool For Finding The Global Minima Of One-Loop Effective Potentials With Many Scalars", Eur.Phys.J. **C73**, 2588 (2013).

[130]M. A. Shifman, A. Vainshtein, M. Voloshin, and V. I. Zakharov, "Low-Energy Theorems for Higgs Boson Couplings to Photons", Sov.J.Nucl.Phys. **30**, 711–716 (1979).

[131]J. Ellis, M. K. Gaillard, and D. Nanopoulos, "A phenomenological profile of the Higgs boson", Nucl. Phys. **B106**, 292–340 (1976).

[132]A. Chakraborty, B. Das, J. L. Diaz-Cruz, D. K. Ghosh, S. Moretti, et al., "The 125 GeV Higgs signal at the LHC in the CP Violating MSSM", arXiv:1301.2745 (2013).

[133]G. Abbiendi et al., "Search for chargino and neutralino production at s**(1/2) = 192-GeV to 209 GeV at LEP", Eur.Phys.J. **C35**, 1–20 (2004).

[134]M. Carena, D. Garcia, U. Nierste, and C. E. Wagner, "Effective Lagrangian for the interaction in the MSSM and charged Higgs phenomenology", Nucl. Phys. **B577**, 88–120 (2000).

[135]R. Barbieri and G. Giudice, "Upper Bounds on Supersymmetric Particle Masses", Nucl.Phys. **B306**, 63 (1988).

[136]J. R. Ellis, K. Enqvist, D. V. Nanopoulos, and F. Zwirner, "Observables in Low-Energy Superstring Models", Mod.Phys.Lett. **A1**, 57 (1986).

[137]H. Baer, V. Barger, P. Huang, D. Mickelson, A. Mustafayev, et al., "Radiative natural supersymmetry: Reconciling electroweak fine-tuning and the Higgs boson mass", Phys.Rev. **D87**, 115028 (2013).

[138]D. Curtin, P. Jaiswal, and P. Meade, "Excluding Electroweak Baryogenesis in the MSSM", JHEP **1208**, 005 (2012).

[139]M. Carena, G. Nardini, M. Quiros, and C. E. Wagner, "MSSM Electroweak Baryogenesis and LHC Data", JHEP **1302**, 001 (2013).

[140]C. Boehm, A. Djouadi, and M. Drees, "Light scalar top quarks and supersymmetric dark matter", Phys.Rev. **D62**, 035012 (2000).

[141]J. R. Ellis, K. A. Olive, and Y. Santoso, "Calculations of neutralino stop coannihilation in the CMSSM", Astropart.Phys. **18**, 395–432 (2003).

[142]C. Balazs, M. S. Carena, A. Menon, D. Morrissey, and C. Wagner, "The Supersymmetric origin of matter", Phys.Rev. **D71**, 075002 (2005).

[143]J. Ellis, K. A. Olive, and J. Zheng, "The Extent of the Stop Coannihilation Strip", Eur.Phys.J. **C74**, 2947 (2014).

[144]A. De Simone, G. F. Giudice, and A. Strumia, "Benchmarks for Dark Matter Searches at the LHC", JHEP **1406**, 081 (2014).

[145]A. Sakharov, "Violation of CP Invariance, c Asymmetry, and Baryon Asymmetry of the Universe", Pisma Zh.Eksp.Teor.Fiz. **5**, 32–35 (1967).

[146]M. Carena, M. Quiros, A. Riotto, I. Vilja, and C. E. M. Wagner, "Electroweak baryogenesis and low energy supersymmetry", Nucl. Phys. **B503**, 387–404 (1997).

[147]A. Masiero and O. Vives, "New physics in CP violation experiments", Ann. Rev. Nucl. Part. Sci. **51**, 161–187 (2001).

[148]Y. Grossman, Z. Ligeti, and Y. Nir, "Future prospects of B physics", Prog.Theor.Phys. **122**, 125–143 (2009).

[149]G. Isidori, Y. Nir, and G. Perez, "Flavor Physics Constraints for Physics Beyond the Standard Model", Ann.Rev.Nucl.Part.Sci. **60**, 355 (2010).

[150]C. Bobeth, M. Bona, A. J. Buras, T. Ewerth, M. Pierini, et al., "Upper bounds on rare K and B decays from minimal flavor violation", Nucl.Phys. **B726**, 252–274 (2005).

[151]G. D'Ambrosio, G. Giudice, G. Isidori, and A. Strumia, "Minimal flavor violation: An Effective field theory approach", Nucl.Phys. **B645**, 155–187 (2002).

[152]A. Buras, P. Gambino, M. Gorbahn, S. Jager, and L. Silvestrini, "Universal unitarity triangle and physics beyond the standard model", Phys.Lett. **B500**, 161–167 (2001).

[153]R. Grober, M. Muhlleitner, E. Popenda, and A. Wlotzka, "Light Stop Decays: Implications for LHC Searches", arXiv:1408.4662 (2014).

[154]R. Grober, M. Muhlleitner, E. Popenda, and A. Wlotzka, "Light stop decays into $Wb\tilde{\chi}_1^0$ near the kinematic threshold", arXiv:1502.05935 (2015).

[155]*Atlas experiment - susy summary plots, https://twiki.cern.ch/twiki/bin/view/atlaspublic/supersymmetrypublicresults.*

[156]G. Aad et al., "Search for a supersymmetric partner to the top quark in final states with jets and missing transverse momentum at $\sqrt{s} = 7$ TeV with the ATLAS detector", Phys.Rev.Lett. **109**, 211802 (2012).

[157]G. Aad et al., "Search for direct top squark pair production in final states with one isolated lepton, jets, and missing transverse momentum in $\sqrt{s} = 7$ TeV pp collisions using 4.7 fb^{-1} of ATLAS data", Phys.Rev.Lett. **109**, 211803 (2012).

[158]G. Aad et al., "Search for a heavy top-quark partner in final states with two leptons with the ATLAS detector at the LHC", JHEP **1211**, 094 (2012).

[159]G. Aad et al., "Search for top squark pair production in final states with one isolated lepton, jets, and missing transverse momentum in $\sqrt{s}$ =8 TeV pp collisions with the ATLAS detector", JHEP **1411**, 118 (2014).

[160]G. Aad et al., "Search for direct pair production of the top squark in all-hadronic final states in proton-proton collisions at $\sqrt{s} = 8$ TeV with the ATLAS detector", JHEP **1409**, 015 (2014).

[161]G. Aad et al., "Search for direct top-squark pair production in final states with two leptons in pp collisions at $\sqrt{s} = 8$TeV with the ATLAS detector", JHEP **1406**, 124 (2014).

[162]G. Aad et al., "Measurement of Spin Correlation in Top-Antitop Quark Events and Search for Top Squark Pair Production in pp Collisions at $\sqrt{s} = 8$ TeV Using the ATLAS Detector", arXiv:1412.4742 (2014).

[163]G. Aad et al., "Search for pair-produced third-generation squarks decaying via charm quarks or in compressed supersymmetric scenarios in pp collisions at $\sqrt{s} = 8$ TeV with the ATLAS detector", Phys.Rev. **D90**, 052008 (2014).

[164]F. Maltoni and T. Stelzer, "MadEvent: Automatic event generation with MadGraph", JHEP **02**, 027 (2003).

[165]T. Stelzer and W. Long, "Automatic generation of tree level helicity amplitudes", Phys. Commun. **81**, 357–371 (2004).

[166]W. Beenakker, S. Brensing, M. Kramer, A. Kulesza, E. Laenen, et al., "Squark and Gluino Hadroproduction", Int.J.Mod.Phys. **A26**, 2637–2664 (2011).

[167]W. Beenakker, S. Brensing, M. Kramer, A. Kulesza, E. Laenen, et al., "Supersymmetric top and bottom squark production at hadron colliders", JHEP **1008**, 098 (2010).

[168]W. Beenakker, M. Kramer, T. Plehn, M. Spira, and P. Zerwas, "Stop production at hadron colliders", Nucl.Phys. **B515**, 3–14 (1998).

[169]J. Alwall, S. Hoche, F. Krauss, N. Lavesson, L. Lonnblad, et al., "Comparative study of various algorithms for the merging of parton showers and matrix elements in hadronic collisions", Eur.Phys.J. **C53**, 473–500 (2008).

[170]T. Sjostrand, "High-energy physics event generation with PYTHIA 5.7 and JETSET 7.4", Comput. Phys. Commun. **82**, 74–90 (1994).

[171]A. S. Belyaev et al., "CompHEP-PYTHIA interface: Integrated package for the collision events generation based on exact matrix elements", hep-ph/0101232 (2000).

[172]T. Sjostrand, S. Mrenna, and P. Z. Skands, "PYTHIA 6.4 Physics and Manual", JHEP **0605**, 026 (2006).

[173]M. Cacciari and G. P. Salam, "Dispelling the N^3 myth for the k_t jet-finder", Phys.Lett. **B641**, 57–61 (2006).

[174]M. Cacciari, G. P. Salam, and G. Soyez, "FastJet User Manual", Eur.Phys.J. **C72**, 1896 (2012).

[175]J. de Favereau et al., "DELPHES 3, A modular framework for fast simulation of a generic collider experiment", JHEP **1402**, 057 (2014).

[176]Z. Han and A. Katz, "Stealth Stops and Spin Correlation: A Snowmass White Paper", arXiv:1310.0356 (2013).

[177]M. Czakon, A. Mitov, M. Papucci, J. T. Ruderman, and A. Weiler, "Closing the stop gap", Phys.Rev.Lett. **113**, 201803 (2014).